Melting in Superheated Silicon Films Under Pulsed-Laser Irradiation

Jin Jimmy Wang

Submitted in partial fulfillment of the

requirements for the degree

of Doctor of Philosophy

in the Graduate School of Arts and Sciences

COLUMBIA UNIVERSITY

2016

ABSTRACT

Melting in Superheated Silicon Films Under Pulsed-Laser Irradiation

Jin Jimmy Wang

This thesis examines melting in superheated silicon films in contact with SiO_2 under pulsed-laser irradiation. An excimer-laser pulse was employed to induce heating of the film by irradiating the film through the transparent fused-quartz substrate such that most of the beam energy was deposited near the bottom Si-SiO_2 interface. Melting dynamics were probed via *in situ* transient reflectance measurements. The temperature profile was estimated computationally by incorporating temperature- and phase-dependent physical parameters and the time-dependent intensity profile of the incident excimer-laser beam obtained from the experiments.

The results indicate that a significant degree of superheating occurred in the subsurface region of the film. Surface-initiated melting was observed in spite of the internal heating scheme, which resulted in the film being substantially hotter at and near the bottom Si-SiO_2 interface. By considering that the surface melts at the equilibrium melting point, the solid-phase-only heat-flow analysis estimates that the bottom Si-SiO_2 interface can be superheated by at least $220\,K$ during excimer-laser irradiation.

It was found that at higher laser fluences (i.e., at higher temperatures), melting can be triggered internally. At heating rates of $10^{10}\,K/s$, melting was observed to initiate at or near the (100)-oriented Si-SiO_2 interface at temperatures estimated to be over $300\,K$ above the equilibrium melting point. Based on theoretical considerations, it was deduced that melting in the superheated solid initiated via a nucleation and growth process. Nucleation rates were estimated from the experimental data using Johnson-Mehl-Avrami-Kolmogorov (JMAK) analysis. Interpretation of the results using classical nucleation theory suggests that nucleation of the liquid phase occurred via the heterogeneous mechanism along the Si-SiO_2 interface.

Table of Contents

List of Figures

List of Tables

Acknowledgments

I am deeply grateful to all those who have assisted and contributed to this work. Among them are: Professor James Im for his guidance and mentorship; Professor Michael Thompson for technical discussions and the single-crystal silicon samples that inspired this work; Adrian Chitu for his invaluable help and advice on the experimental part of the work; Dr. Alexander Limanov for helping me get started in the lab and for his expertise and advice; Dr. Ying Wang for numerous technical discussions and providing me with MPS samples that enabled me to do experiments that, despite not being in this dissertation, were critical in developing the ideas and conclusions in this work; Vernon Wong for many helpful technical discussions and providing helpful feedback on this dissertation; Wenkai Pan for his invaluable assistance related to all things computational; Miao Yu for technical discussions and his especially insightful questions during group meetings. Additionally, I would like to thank Miao Yu and Wenkai Pan for allowing me to stay in their guest room for the months when finances were challenging.

This thesis is dedicated to all my Teachers, not only those from school, but to all those who have taught me something important in my life.

Chapter 1

Introduction

The melting of solids is a major topic of interest in materials science and condensed-matter physics. In addition to its fundamental importance, it is also a critical part of many materials processes. Materials processes that involve melting are used in various areas such as metallurgy, polymer science, food science, semiconductors, and many more. Due to its interdisciplinary nature, improved understanding of the melting of solids may lead to profound implications across various disciplines. This thesis examines melting during an important technological process – excimer-laser-induced melting of silicon films – in order to reveal fundamental mechanisms of melting that are significant both scientifically and technologically.

1.1 Excimer Laser Crystallization

Excimer laser crystallization techniques [4, 5] are capable of producing high-quality polycrystalline silicon (often referred to as "polysilicon" or p-Si) for the fabrication of electronic devices on low-thermal-budget substrates, such as inexpensive transparent substrates for display applications. Such processes typically involve starting with a precursor amorphous silicon (a-Si) material deposited on glass substrates at relatively low, substrate-compatible temperatures (approximately $300°C$) using plasma-enhanced chemical vapor deposition (PECVD). Next, the a-Si-on-glass is irradiated under an excimer-laser beam (at an ultraviolet wavelength) in order to crystallize it into p-Si. Most of the incident beam energy is deposited in the first ten nanometers of the film due to the high absorption coefficient of silicon in the UV region and the short pulse duration of the

incident beam, allowing most of the substrate to remain near room temperature. The resulting melting then leads to crystallization and/or grain enlargement during solidification. This crystallization process is quite intricate and the resulting microstructure depends intimately on a variety of processing conditions. Research in this field has resulted in various laser-crystallization techniques yielding a variety of possible microstructures that are unique to such techniques. That fact that laser crystallization is capable of producing well-controlled microstructures on low-thermal-budget substrates has led to its extensive application in electronic display manufacturing.

Microstructure engineering, particularly, control of the location and amount of grain boundaries in silicon films, is critical in producing high-quality silicon for electronic display applications. Since grain boundaries in the material drastically reduce transistor performance [6, 7] and are therefore unwelcomed, in order to reduce grain boundaries in the film, a simple solution would be to merely increase the average grain size. However, a new problem is introduced as grain size approaches the area of the active channel in the thin-film-transistor (TFT): The variation in the length of randomly located grain boundaries contained within the TFT becomes exceedingly large which leads to unacceptably large device-to-device fluctuations in device characteristics. Uniformity in the electrical characteristics of the material is critical as these p-Si-based TFTs are typically used as pixel-controlling elements in high-performance electronic displays.

Thus an excimer laser crystallization technique called excimer laser annealing (ELA) was developed in order to address the above issues. Excimer laser annealing is a multiple-pulse-per-area laser crystallization process. The first pulse involves crystallization of the initially amorphous silicon. The successive pulses lead to partial melting and subsequent resolidification of the film, leading to grain-size enlargement. Due to its ability to produce p-Si with sufficiently uniform and moderately sized grains, it has gained extensive adoption in the manufacturing of electronic displays.

Despite the fact that ELA is a critical process in the manufacturing of high-performance electronic displays, researchers have proposed wildly diverging and incompatible models of the ELA process [8–10]. The fundamental difference in these drastically different models lie in their disagreement regarding the spatiotemporal extent of melting of the polycrystalline films during the

excimer-laser-induced grain-enlargement process. While it is known that melting is favored to initiate at more defective, high-excess-free-energy sites, details regarding how melting initiates and transpires, particularly within these microstructurally complex p-Si films that contain a variety of buried interfaces such as grain boundaries and Si-SiO_2 interfaces, remain to be examined in detail.

1.2 Fundamental Investigations of Melting

Although much theoretical work has been performed regarding the nature of internal melting and melting at buried interfaces [11], experimental work in the area has been insufficient. It is well known that, under typical conditions, while melting readily initiates at surfaces and other material defects, an ideal perfect crystal (without surfaces or interfaces) may be heated well above its equilibrium melting point while remaining solid in a phenomenon called "superheating." Moreover, it has been observed that, under certain conditions, buried interfaces such as low-excess-free-energy heterophase interfaces and coherent grain boundaries can be significantly superheated above the equilibrium melting point [12]. Due to the many heteogeneities in solid materials, melting, and particularly internal melting, in solids is inherently complex. While there are theoretical predictions for the limits of superheating before the onset of melting at various sites in a solid (e.g., superheated grain boundaries, internal nucleation of liquid, etc.), many of these theoretical predictions remain experimentally untested due to difficulties in probing melting at buried interfaces.

1.3 An Unusual Opportunity to Experimentally Investigate Internal Melting

Systematic examination of melting at buried interfaces is experimentally challenging but is necessary in order to understand melting in the microstructurally complex p-Si in ELA and to better our fundamental understanding of the melting process. In order to develop a clear understanding of how melting initiates and transpires at these buried interfaces, it is fruitful to examine

each interface separately in simple systems. This dissertation is focused primarily on melting of single-crystal silicon at and near the Si-SiO_2 interface. By utilizing single-crystal silicon films on transparent fused quartz substrates in the present experiments, we were afforded the unusual opportunity to induce internal heating (and superheating) of the silicon near the bottom Si-SiO_2 interface via substrate-side excimer-laser laser irradiation, leading to a significant thermal gradient in the film where the near-substrate region is hottest. The near-absence of defects (the dislocation density was estimated to be approximately 10^{-2} cm^2) in the single-crystal material enabled us to focus on examining melting at the surface, the bottom Si-SiO_2 interface, and homogeneously in the film. The transparent substrate enabled *in situ* optical reflectance measurements [13] from both the surface side and the substrate side, providing detailed quantitative information pertaining to the temperature- and phase-transition-evolution of the films. Additionally, the atomically flat nature of the Si-SiO_2 interface avoids the problem of interface roughness, which can affect the melting process. The experiments here thus present a remarkable opportunity to examine melting of a superheated solid at and near a buried interface in a practically ideal material system, which, traditionally, is an extremely challenging experimental endeavor.

Using this unique and experimentally-enabling material, the strategy of the present investigation is to first examine (via internal heating and optical reflectance probes) melting of single-crystal silicon at and near the Si-SiO_2 interface. Once we have established sufficient understanding of melting at and near the Si-SiO_2 interface, we examine the effects of how the introduction of grain boundaries into the same material (via complete-melting-crystallization of the initially single-crystal material) affects melting. In order to extract quantitative information from the experiments, we perform a series of thermal analysis on the experiments. Due to the nonlinear, time- and temperature-dependence of many of the parameters, in order to provide accurate estimates of the thermal evolution in the films during laser irradiation, our thermal analysis utilizes the `3DNS` laser-irradiation-simulation software previously developed in our research group [14]. Using quantitative information extracted from the experimental data, we discuss our results in light of the proposed theoretical models of melting in superheated solids. In essence, the main contributions of this

dissertation are: (1) quantitative and systematic experiments in order to understand fundamental melting mechanisms in superheated solids, and (2) experimental investigations of melting at buried interfaces in a technologically important material – silicon films – which may enable better predictive models and process control of present and future laser crystallization processes.

1.4 Dissertation Outline

This thesis is organized into the following chapters:

Chapter 2 provides the relevant background information on the science of superheating and melting in solids. In the latter part of this chapter, we discuss how fundamental understanding of melting is relevant for understanding and improving important laser crystallization processes. Chapter 3 discusses in detail the experimental approach of this work, including the materials, experimental setup, and thermal analysis. Chapter 4 presents experimental results on internal heating and melting of single-crystal silicon-on-quartz. We present experimental data showing that surface-initiated melting was observed under substrate-side irradiation, in which the subsurface region of the film (while still solid) is much hotter than the top surface, suggesting that the subsurface region of the film must have undergone a significant degree of superheating. Chapter 5 presents quantitative thermal analysis of the experimental results presented in the previous chapter. We describe the thermal analysis procedures in detail and provide quantitative estimates of the degree of superheating. Chapter 6 examines theoretical predictions on the mechanisms of melting and argues that liquid nucleation is the predicted mechanism of melting in this work. Nucleation rates were estimated from the experimental data. Chapter 7 fits the experimental data using classical nucleation theory in order to examine whether one should expect homogeneous or heterogeneous nucleation. Chapter 8 concludes the dissertation and points to future research directions.

Chapter 2

Background and Motivation

The study of melting in solids is of great scientific and technological interest due to its ubiquity in nature and its diverse applications in materials processing. The nature of melting in a solid depends sensitively not only on its thermodynamic conditions, but also on defects in the solid. As such, various experimental, theoretical, and computational investigations have been performed in order to study melting at various material interfaces, including surfaces, grain boundaries, and more. It has been predicted and observed that under certain conditions, solids can be superheated above their respective equilibrium melting points. The complexity of melting in solids has led to many unresolved scientific questions that may lead to fundamental and technological developments in materials science and engineering. In this chapter, a basic overview of various melting mechanisms is presented, with a focus on melting in crystalline solids. As well, some background information on the current understanding of several technologically important pulsed-laser melting processes and their unresolved questions are presented.

2.1 Classical Thermodynamics Description of Melting

It is well-established that, for a given pressure, the solid and liquid phases of a material can co-exist at a temperature known as the melting point. Solidification is thermodynamically favored to occur if

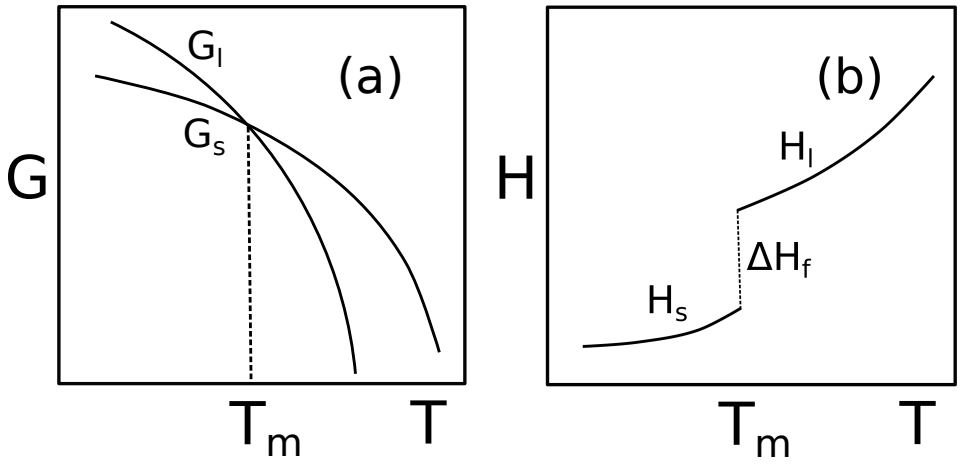

Figure 2.1: (a) Schematic plot of the Gibbs free energy of the solid phase, ΔG_s, and the Gibbs free energy of the liquid phase, ΔG_l, as a function of temperature. T_m is the equilibrium melting point. (b) Schematic plot of the enthalpy of the solid phase (ΔH_s) and the enthalpy of the liquid phase (ΔH_l) as a function of temperature.

the temperature of a solid drops below its melting point; and melting is thermodynamically favored to occur if the temperature of a solid increases above its melting point [15]. Thermodynamically, the melting point is defined as the temperature at which the Gibbs free energy of the solid phase is equal to that of the liquid phase, as shown in Figure 2.1.

Since melting is a transition involving a discrete change in enthalpy (see Figure 2.1), it is considered a first-order or discontinuous phase transition [16]. In addition to its consumption of enthalpy (thereby rendering it an endothermic process), melting also leads to a discontinuity in heat capacity, density, and other physical parameters. In particular, for silicon, melting leads to a drastic increase in thermal conductivity, optical reflectance, and density due to the fact that liquid silicon is essentially metallic [13].

2.1.1 The Interface Response Function

Once a solid-liquid interface forms, its motion depends exponentially on the interface temperature. The velocity of the solidifying or melting interface is given by the interface response function [17]:

$$v\left(T\right) = v_0 \exp\left(-\frac{Q}{kT}\right)\left[1 - \exp\left(-\frac{\Delta G_{ls}\left(T\right)}{kT}\right)\right], \tag{2.1}$$

where T is the temperature at the interface, v_0 is a kinetic prefactor, Q is the activation energy, k is the Boltzmann constant, and ΔG_{ls} is the difference in Gibbs free energy per atom between the liquid and solid. At high temperatures, where $c_{p,l} \approx c_{p,s}$, $\Delta G_{ls} = \frac{\Delta H_f \Delta T}{T_m}$, where $\Delta T = T_m - T$. If ΔG_v is sufficiently small, the exponential term may be rewritten in terms of its Taylor series expansion. Under this approximation, v is linearly dependent on ΔT,

$$v = c\Delta T, \tag{2.2}$$

where c is a constant that can be extracted from experimental data. Using the convention here, $v > 0$ for solidification and $v < 0$ for melting.

2.1.2 The Gibbs-Thomson Effect

Although a solid typically starts to melt at its equilibrium melting point, various factors such as kinetic factors and crystal defects (or lack thereof) may significantly affect the actual temperature at the onset of melting. One such factor is the local curvature in a solid. This is called the Gibbs-Thomson effect and is described by the following equation [18, 19]:

$$T_m = T_{mp}\left(1 - \frac{2\sigma_{sl}}{\Delta H_f}\kappa_{local}\right), \tag{2.3}$$

where T_m is the local equilibrium melting temperature, T_{mp} is the bulk equilibrium melting point, σ_{sl} is the solid-liquid interface free energy, ΔH_f is the enthalpy of fusion, and κ_{local} is the local curvature of the solid phase. Depending on the sign of the local curvature, the local equilibrium melting temperature may be either elevated or depressed.

2.2 Initiation of the Melting Transition at Material Interfaces

Under most circumstances, including in silicon laser crystallization processes, melting initiates at material defects such as surfaces, grain boundaries, and heterophase interfaces. Thus in order to understand how melting transpires in a solid during melt-mediated materials processing, it is necessary to have some fundamental understanding of how melting initiates at various common material interfaces. In this section, we provide an overview of melting at the interfaces relevant to the experiments performed as part of this work.

2.2.1 Surface Melting

Due to the presence of surfaces, it is often incredibly challenging to experimentally heat a solid substantially above its melting point. This due to the fact that surface pre-melting (and subsequent discontinuous melting), may occur as the temperature of a solid is heated to its melting point [20]. Thermodynamically, surface pre-melting can be viewed as the wetting of the solid surface by its liquid as the solid is heated to its melting point. This wetting condition is given by [21]:

$$\sigma_{sv} > \sigma_{lv} + \sigma_{sl}, \tag{2.4}$$

where σ_{sv} is the interface energy of the solid-vapor interface, σ_{lv} is the interface energy of the liquid-vapor interface, and σ_{sl} is the interface energy of the solid-liquid interface. If this wetting condition is satisfied, the surface becomes disordered. As the temperature increases, this "quasi-liquid" layer, having properties that are intermediate between those of the solid and the liquid, grows in thickness. As the temperature of the solid increases to its melting point, the disordered layer behaves like a bulk liquid and discontinuous melting of the surface ensues.

For a crystalline material, the propensity for surface pre-melting is dependent on the surface orientation, as shown in Equation 2.4. In fact, there are surfaces that do not exhibit pre-melting below the melting point. Various surfaces have even been observed to undergo superheating under extreme heating rates [22]. However, these extreme heating rates are above and beyond those observed in the experiments presented in this dissertation. Thus, in the present work, since bulk

melting of the surface occurs at or very near the melting point, in most cases, it can be assumed that discontinuous surface melting initiates at the melting point of silicon. It should also be noted that pre-melting cannot be detected with our experimental setup.

2.2.2 Grain Boundary Melting

Grain boundaries are a type of crystal defect that can trigger melting. Experimentally, it has been observed that melting can be triggered at grain boundaries at or very near the melting point [23]. Molecular dynamics simulations have also demonstrated that high-angle grain boundaries in silicon and other elemental solids melt at or very near the equilibrium melting point [24–26] although whether pre-melting occurs along grain boundaries in bulk elemental solids is still unclear due to the lack of experimental evidence and differing theoretical and computational models [26, 27]. Theoretical results have suggested that certain low-excess-free-energy grain boundaries, such as highly symmetric tilt boundaries, can be superheated substantially above the melting point due to a nucleation barrier to liquid formation [28, 29]. However, experimental results on pre-melting, melting and superheating at grain boundaries continue to be lacking due to the difficulties in investigating melting at such buried interfaces.

2.2.3 Melting at Solid-Solid Interfaces

Another material interface that must be considered in the present investigation is solid-solid interfaces. Whether the heterophase interface is stable against melting is highly dependent upon the structure of the interface. For example, at a low-excess-free-energy interface, such as in coherent or semi-coherent interfaces, substantial superheating of the solid may be possible [30]. Even in amorphous-crystal interfaces, substantial superheating can be observed along low-excess-free-energy interfaces, such as SiO_2-Ge interfaces [31]. Thus it is expected that the low-excess-free-energy interfaces, such as the Si-SiO_2 interface in the present work, can undergo substantial superheating. On the other hand, under typical experimental conditions, high-excess-free-energy interfaces cannot undergo a significant degree of superheating [11].

2.3 Melting in Superheated Solids

In order to fundamentally understand the melting transition, simple experiments on simple materials can reveal much about the nature of melting. Just as homogeneous nucleation of solid in a substantially undercooled liquid corresponds to one of the simplest cases of solidification, the formation of liquid from within the bulk of a crystal (which requires substantial superheating) corresponds to one of the simplest cases of melting. Since, as discussed in the previous sections of this chapter, solids are often very heterogeneous materials, containing a variety of defects which can affect the melting process. Thus, it is of scientific interest to investigate superheating and internal melting of homogeneous crystals.

A long-standing question in materials science and condensed-matter physics is: What is the superheating limit of a solid? In order to address the question of the upper superheating limit of a solid, various theoretical models have been proposed. Drawing on Kauzmann's idea on the glass transition [32], Fecht and Johnson proposed a thermodynamic upper superheating limit of a solid at the isentropic point – the temperature at which the entropy of its liquid phase is equal to that of its solid phase [33]. Later on, Tallon argued that the isentropic point proposed by Fecht and Johnson is actually an outer bound limit since the rigidity limit, the temperature at which the shear modulus of the solid falls to zero, falls below the isentropic point [34]. However, these predicted upper limits of superheating were never observed experimentally [2]. Moreover, it has been shown that nucleation models, such as classical nucleation theory [2, 30, 35], have given upper bound superheating limits lower than all of the other models mentioned above for heating rates normally observed in experiments ($< 10^{13}\ K/s$). And in a theoretical investigation by Mei et al., classical nucleation theory, when applied to the heterogeneous at semicoherent interfaces, accurately predicted the corresponding experimentally observed superheated melting temperatures [30].

2.3.1 Nucleation of Liquid in Superheated Solids

It is relevant at this point to provide a brief introduction to liquid nucleation in a superheated elemental solid. More detailed expositions of nucleation, including the analytic expressions of classical nucleation theory is presented in Chapter 7 and Appendix A.

Nucleation is a stochastic process that involves the random fluctuations in the local ordering of atoms. As a solid is heated, clusters of disordered atoms spontaneously appear. Being a stochastic process, the size of any single cluster may randomly grow and shrink. Thus the cluster size is best described by its size distribution, which from statistical mechanical considerations follows a Boltzmann distribution:

$$N\left(n,T\right) \propto \exp\left(-\frac{\Delta G\left(n,T\right)}{kT}\right), \tag{2.5}$$

where $N(n)$ is the number of clusters containing n atoms, $\Delta G\left(n\right)$ is an activation energy to form a cluster of n atoms, k is the Boltzmann constant, and T is the local temperature. The size distribution of these clusters increases as the temperature of the solid is increased. According to classical nucleation theory, once the size of a cluster exceeds the "critical cluster size", n^*, it is statistically favored to grow. The rate of generation of these supercritical clusters is defined as the nucleation rate. Hence, the nucleation rate can be approximated as the critical cluster population multiplied by a pre-exponential term:

$$I\left(T\right) = I_0\left(T\right)\exp\left(-\frac{\Delta G\left(n^*,T\right)}{kT}\right). \tag{2.6}$$

For the homogeneous nucleation of liquid, the temperature at which n^* (and, consequently, the nucleation rate) becomes significant is expected to be substantially higher than the equilibrium melting point.

Nucleation can occur homogeneously or heterogeneously. In homogeneous nucleation, schematically shown in Figure 2.2 the stochastic formation of a new phase occurs in defect-free and homogeneous regions of the metastable parent phase. In contrast, in heterogeneous nucleation, schematically shown in Figure 2.3, the stochastic formation of a new phase occurs at catalyzing interfaces, such as grain boundaries, heterophase interfaces, and other heterogeneities in the metastable parent

phase. The new phase forms a contact angle with the catalyzing interface, thereby decreasing the critical cluster size for formation, which reduces $\Delta G(n^*)$. Since the nucleation rate (Equation 2.6) is exponentially dependent on T and $\Delta G(n^*)$, in most cases, heterogeneous nucleation of liquid and subsequent growth of the liquid phase is expected to completely transform the solid before the onset of homogeneous nucleation.

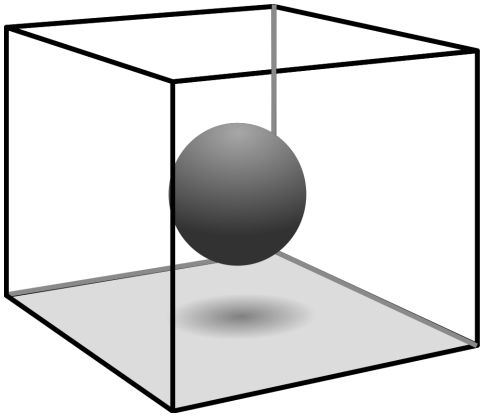

Figure 2.2: Schematic diagram of a homogeneously nucleated sphere in its parent material.

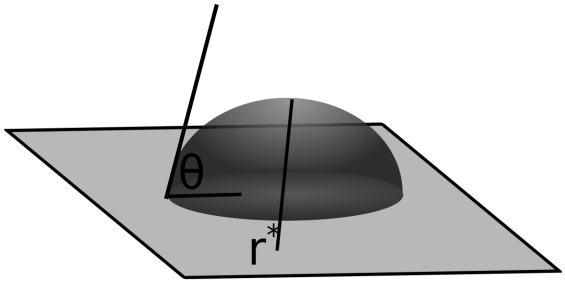

Figure 2.3: Schematic diagram of a heterogeneously nucleated spherical cap forming a contact angle of θ along the catalyzing interface in its parent material.

2.3.2 Implementations of Superheating Experiments

In practice, under typical conditions, melting readily initiates at free surfaces and random high-angle grain boundaries at or near the equilibrium melting point, rendering superheating experiments very challenging. Experimental investigations of superheating have been performed using various techniques such as internal heating [36], heating an encapsulated solid [31,37–41], shock-wave loading [42,43], and intense pulsed-laser irradiation [22,43–45]. The strategy of these experiments is to suppress melting at defects by manipulating the material, to induce internal heating of the material, or to kinetically suppress the onset of melting by using high heating rates. However, there have been no results reported on the internal melting of a substantially superheated elemental, defect-free, single-crystal solid film on an atomically flat substrate – the ideal material for such experiments, as extrinsic complicating factors such as uncontrolled crystal defects, nanoscale effects, and interface roughness are essentially removed from the experiment. Our experiments – which utilizes single-crystal, semiconductor-grade undoped silicon on fused quartz substrates – thus presents an unusual opportunity to experimentally examine melting and superheating in a simple material system.

2.4 Melt-Mediated Processing of Silicon Films

In melt-mediated silicon-laser-crystallization processes, such as ELA, the resulting microstructure after laser processing is extremely sensitive to the extent in which melting proceeds in the film [46]. Microstructure is important as it can significantly affect the electrical characteristics of the silicon film, which, in turn, affect the performance of transistors fabricated on the film. Clearly, silicon films not only serve as the ideal material for such melting and superheating studies (due to established capabilities and techniques in precisely controlling their microstructure) but understanding the melting behavior of silicon films may lead to profound technological implications. In this section, we review the science and technology of various laser crystallization techniques and examine some of the unanswered questions in the study of pulsed-laser melting of silicon.

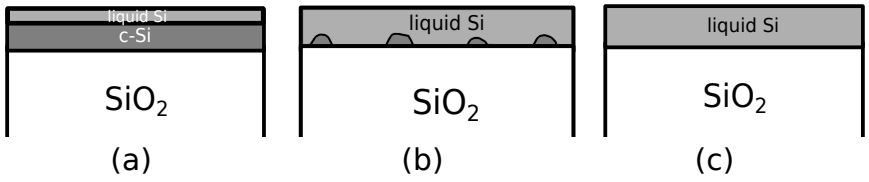

Figure 2.4: (a) Partial melting regime (b) Super-lateral growth (SLG) regime (c) Complete melting regime. Crystalline silicon is abbreviated as "c-Si".

2.4.1 Melting Regimes in Excimer Laser Processing of Silicon Films

In excimer-laser-beam-induced melting of silicon films, Im et al. have established that there are three different melting regimes, depending on the maximum melt depth (which, in turn, is dependent on the energy density of the incident beam) during the melting process [46]. Schematics of these melting regimes showing the maximum melt depths are shown in Figure 2.4. In the partial melting regime and in the super-lateral growth (SLG) regime, since there remains unmelted residual solid in the film in contact with the liquid silicon, prompt regrowth of solid occurs. In the complete melting regime, since the entire depth of the film eventually transforms into liquid (effectively erasing the "microstructure history" of the film) solidification is triggered via a nucleation and growth process. Thus, it can be inferred that for partial-melting-based processes such as excimer laser annealing (ELA) (described below in Section 2.4.2), the extent of melting in the film (which is dependent on the incident-beam-energy-density and existing material defects in the film, among other things) essentially dictates the final microstructure of the silicon film.

2.4.2 Excimer Laser Annealing (ELA)

Excimer laser annealing (ELA) is a critical step in the manufacturing of low-temperature polycrystalline silicon (LTPS) backplanes for high-performance flat-panel displays. It is a multiple pulse-per-area process, where each point on the silicon films is irradiated up to twenty times, starting from initially amorphous silicon films on glass substrates. After the first pulse, the amorphous silicon crystallizes into polycrystalline silicon. With each subsequent laser pulse, partial-melting

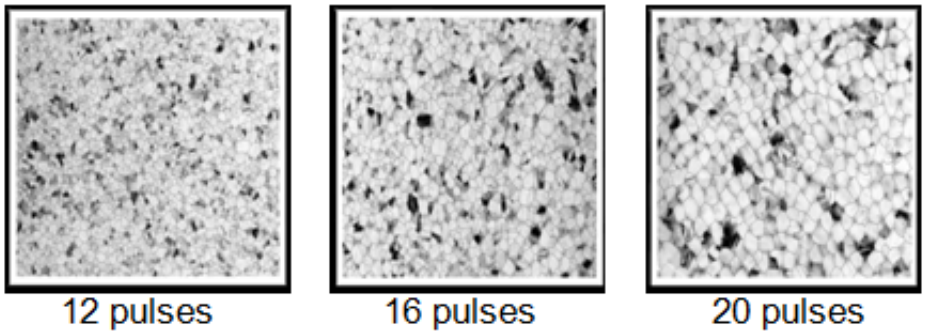

Figure 2.5: Plan-view TEM images showing defect-etched, 50-nm polycrystalline silicon irradiated under typical ELA processing conditions after 12, 16, and 20 pulses (from left to right).

and subsequent resolidification transpires in the film leading to grain-size enlargement of the now polycrystalline material. Eventually, the average grain size of film saturates at approximately the wavelength of the incident laser beam. Representative plan-view TEM images of the grain-enlargement process as observed in a typical 20-shot ELA process are shown in Figure 2.5.

ELA is extensively used to produce LTPS in the display industry with various implementations. A typical ELA process involves a homogenized excimer-laser beam shaped into a high-aspect ratio rectangle and scanned across the sample at high rates of at least 1 cm/s in order to optimize the output. High pulse-repetition frequencies are matched to the beam translation velocity to produce overlapping irradiated regions such that each area is irradiated multiple times. Such implementations can yield high output processes that enable the production of LTPS on inexpensive transparent substrates such as glass or plastic for electronic displays and other large-area electronics applications.

The microstructure of the resulting material is extremely sensitive to fluctuations in the energy density of the incident beam, which, in manufacturing, translates to a very small process window. To improve manufacturing yield and efficiency, it is desirable that the number of exposures be decreased and the process window increased. Additionally, as the demand for ever-higher performing displays increases, higher quality silicon films with greater material uniformity will be required. Since ELA is a partial-melting process which relies on melting to eliminate certain grains, resulting

in the increase of the average grain size, melting is essentially the microstructure-determining step of the laser annealing process. To these ends, it is fruitful to understand various mechanisms of melting that transpire during pulsed-laser processing in ELA.

2.4.2.1 Unsolved Problems in ELA Melting Models

Unfortunately, the current state of understanding of melting mechanisms in ELA leave much to be desired. Although it is known that ELA is a partial-melting-based process, the details of melting are not well-understood, and there exists contradictory explanations on how the details of melting in the ELA process lead to the resulting ELA microstructure [8–10]. And, despite the fact that surface conditions (such as whether the surface is oxidized) clearly affect the melting process and the resulting surface roughness [47], not much is known about initiating melting at the Si-SiO_2 interface. Systematic studies of melting mechanisms pertaining to ELA are very much needed in order to address these unanswered questions.

2.4.3 Mixed-Phase Solidification

Another crystallization process that can produce silicon films with a very unique and useful microstructure is mixed-phase solidification (MPS). MPS is a multiple exposure process in which silicon films are exposed to a radiative beam (such as light from a continuous wave (CW) laser) multiple times until both average the grain size and the fraction of (100)-surface-texturing soft-saturates [1,48]. The process can produce micron-sized grains that are highly (100)-surface-textured (i.e., >99% of the grains were within 15° of (100)). The unique microstructure of MPS-processed silicon films is explained by considering the interplay between the following characteristics and phenomena: (1) the reflectivity difference between solid and liquid silicon and (2) the dynamically balanced yet continuously changing surroundings of stable coexisting superheated solid and supercooled liquid regions. It has been observed that, in the MPS process, melting initiates primarily at the grain boundaries and proceeds laterally in the film at rates depending on the local thermal and thermodynamic conditions. A schematic diagram illustrating the solid-liquid coexistence along

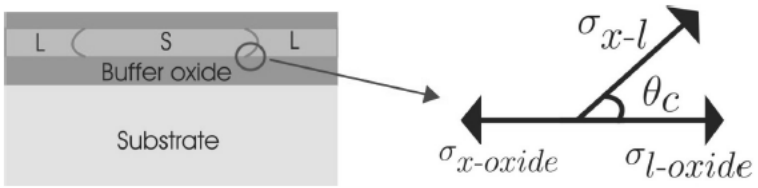

Figure 2.6: A schematic diagram illustrating the solid-liquid coexistence in the silicon film. A relationship between interface energies and the contact angle is shown. Figure adapted from [1].

with the local interface energies is shown in Figure 2.6.

2.4.3.1 Unresolved Problems in the MPS Model

The fact that melting initiates at the grain boundaries and transpires laterally in the film may indicate that grain boundaries are more susceptible to melting than the Si-SiO_2 interface. Although the MPS thermodynamic model proposed by Chahal [1, 48] gives a consistent picture of melting in MPS processing, details regarding the propensity to melting for various interfaces (in this case, grain boundaries and Si-SiO_2 interfaces) remain to be examined in detail.

2.5 Motivation and Research Strategy

Experimental investigations on the melting of solids, particularly for internal melting at buried interfaces and in substantially superheated solids, are very much desired [11, 43]. Technologically, melting in silicon films occurs in economically important manufacturing processes such as ELA, which is currently being used to create LTPS backplanes for high-performance displays. Although there are numerous published studies on melting of silicon films, various descriptions of melting and solidification in silicon films are inconsistent and incompatible [8–10]. Moreover, fundamental investigations of melting at and near the technologically important Si-SiO_2 interface have been insufficient. The present work aims to contribute both scientifically and technologically by performing systematic experiments of fundamental importance on the technologically important silicon thin

films.

The motivation of this work is twofold: (1) to contribute technologically by examining melting in the technologically relevant silicon film as it undergoes the excimer-laser irradiation process; and (2) to experimentally address fundamental questions and examine theoretical models in the melting of superheated solids.

We argue that in order to understand melting in the ELA process, one must systematically examine how melting initiates and transpires at surfaces and at buried interfaces such as grain boundaries and Si-SiO_2 interfaces. Furthermore, in order to conduct simple and clean experiments, our strategy is to examine melting at each of these defects separately in simple systems. The strategy of the present investigation is to first examine melting of single-crystal silicon at and near the Si-SiO_2 interface. More complicated material defects (i.e., grain boundaries, etc.) are introduced into the experiments after sufficient understanding of melting in single-crystal silicon is established.

In addition to contributing technologically, we aim to design and implement experiments that can provide clean results that simultaneously address fundamental questions regarding melting in superheated solids. The fundamental goals of this work are (1) to quantitatively estimate the degree of superheating at and near the Si-SiO_2 interface during pulsed-laser heating and (2) to compare our experimental results to the corresponding theoretical models of melting in order to examine their applicability and predictions. In order to accurately estimate the degree of superheating in this highly nonlinear and transient system, our strategy is to perform systematic computational thermal analysis of the laser irradiation experiments. The quantitative superheating estimates then enable critical examination of the proposed theoretical models.

2.6 Summary

In summary, pulsed-laser-induced-melting experiments on silicon afford the unusual opportunity to investigate fundamental mechanisms of melting relevant to technologically relevant materials

processes. By choosing single-crystal silicon-on-quartz as our material of investigation, simple melting experiments may be performed without the complications of grain boundaries. This enables us to focus on investigating melting at the technologically relevant Si-SiO_2 interface, which is important in industrial laser crystallization processes. Due to the low excess-free-energy of the Si-SiO_2 interface, and especially the (100)-oriented Si-SiO_2 interface examined in the present investigation, it is expected that, at the high heating rates induced by the excimer-laser beam, a substantial degree of superheating may be observed. Quantitative analysis of the observed heating enables critical examination of various proposed theoretical models of melting in substantially superheated solids, which may lead to new fundamental developments on the science of melting. Once we have acquired sufficient understanding of melting at and near the Si-SiO_2 interface, we proceed to perform experiments on polycrystalline silicon films in order to further our understanding of melting in the technologically important silicon films.

Chapter 3

Research Approach

Experimentally observing melting at buried interfaces is not an easy task and requires judicious experimental design and implementation. In order to examine superheating and melting at and near the Si-SiO_2 interface, our strategy is perform simple internal laser-induced heating experiments on single-crystal silicon-on-quartz. Our approach is as follows:

Excimer-Laser Irradiation: Internal heating was induced in silicon films via substrate-side excimer-laser irradiation of the silicon-on-quartz samples through the transparent fused-quartz substrate, depositing most of the incident beam energy at and near the bottom Si-SiO_2 interface.

***In situ* Transient Reflectance:** *In situ* transient reflectance measurements from both the surface side and surface side were obtained via continuous-wave laser probes.

Thermal Analysis: Thermal analysis was performed by simulating the conditions observed in the experiments and analyzing the computations along with the *in situ* transient reflectance signals.

3.1 Sample Configurations

The material used in the present investigation is (100)-surface-oriented, undoped, single-crystal, 200-nm silicon films, on thermally grown SiO_2 on 0.7-mm fused-quartz substrates fabricated using

a wafer-bonding-based [49] silicon-on-insulator technique. The single-crystal material with (100) surface orientation was chosen for investigation as the material is, first and foremost, free of grain boundaries (thereby enabling us to focus on simpler and uniform excess free energy sites of the top surface and the bottom Si-SiO_2 interface); and, additionally, the (100)-oriented Si-SiO_2 interface corresponds presumably to the most energetically stable configuration [48,50] (thereby making this interface commensurately more melt-resistant than those of other orientations). The dislocation density in the silicon films was estimated to be on the order of $10^2\,cm^{-2}$. The transparent nature of the fused-quartz substrate is a particularly and doubly enabling element in the present experiments as it permitted us to (1) substrate-side irradiate the sample and induce internal heating of the film via subsurface energy deposition of the incident beam mostly near the bottom interface, and (2) obtain more spatially comprehensive *in situ* information about how melting proceeds in the film by examining the substrate-side TR signals (in addition to the usual surface-side TR signals).

Initially, the samples were coated with a 50-nm SiO_2 capping layer deposited using low-pressure chemical vapor deposition (LPCVD). To evaluate the effects of the Si-SiO_2 interface on melting, we performed experiments under two types of surface conditions: oxide-free (via BHF-etchant) and oxide-capped (as-processed, with the 50-nm LPCVD-deposited oxide). In order to compare the effects of surface heating versus internal heating, the samples were irradiated under two different geometries (see Figure 3.1): (1) surface-side irradiation and (2) substrate-side irradiation. Case (1) corresponds to the standard excimer-laser-irradiation geometry in which the top surface of the film absorbs most of the beam energy such that it is much hotter at the top surface than at the bottom interface. Case (2) corresponds to the geometry in which the *bottom* Si-SiO_2 *interface* is much hotter than the top surface, i.e., resulting in internal heating of the film where most of the beam energy is deposited near the bottom Si-SiO_2 interface due to the extremely high absorption coefficient of silicon for the incident UV light.

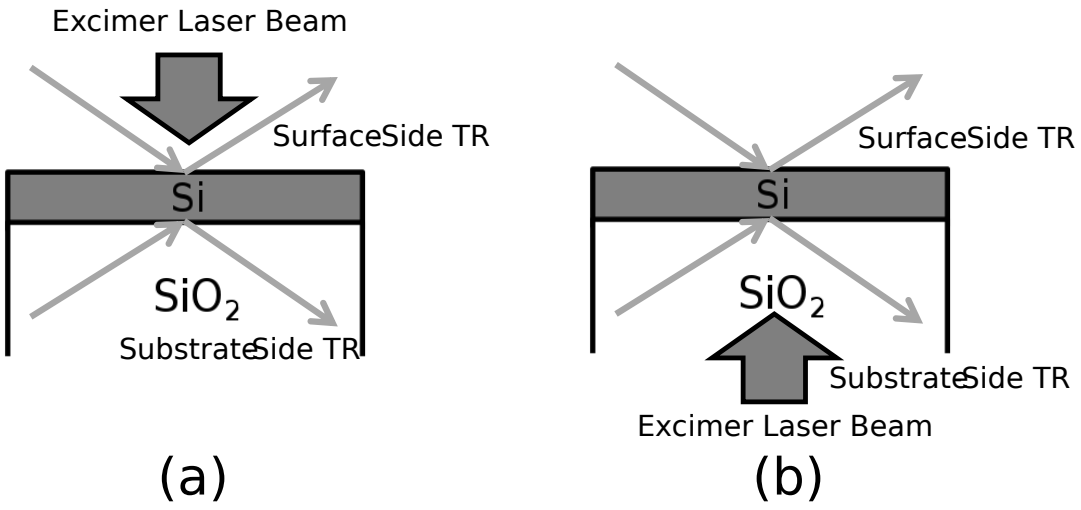

Figure 3.1: (a) Surface-side irradiation, where the excimer laser beam is directly incident on the top surface of the film. This is the typical irradiation geometry in excimer-laser processing. (b) Substrate-side irradiation, where the excimer-laser beam transmits through the transparent fused-quartz substrate and deposits most of its energy at and near the the bottom Si-SiO_2 interface. This atypical irradiation geometry enables internal heating of the film near the bottom Si-SiO_2 interface.

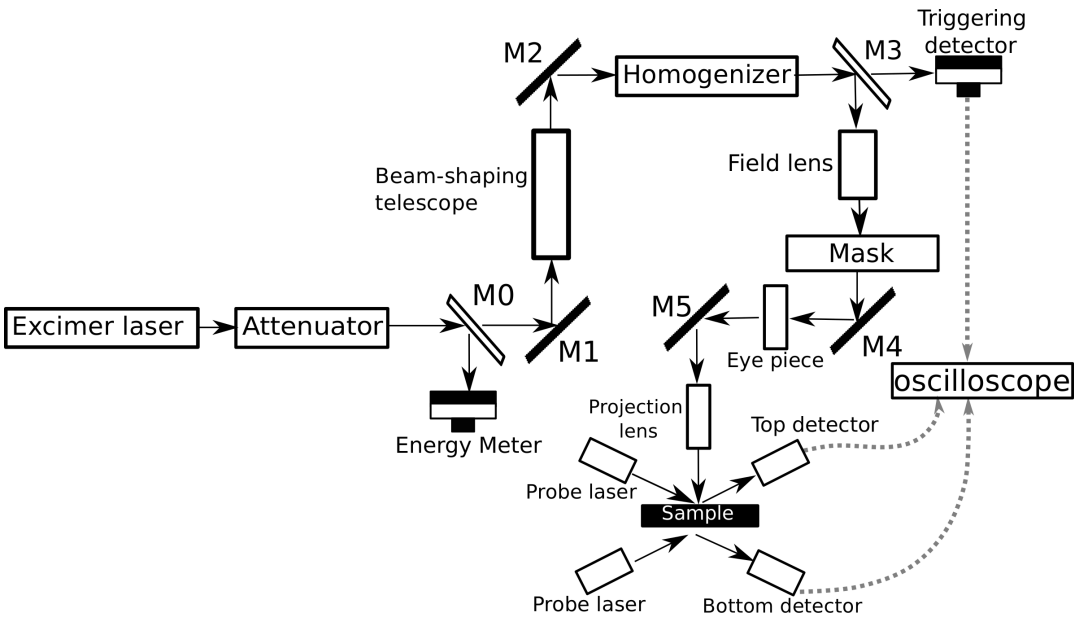

Figure 3.2: Schematic of the excimer-laser system used in the experiments.

3.2 Experimental Setup

3.2.1 Laser Irradiation System

Figure 3.2 shows the schematic diagram of the laser irradiation system. For this investigation, we used a XeCl excimer laser, operating at a wavelength of 308 nm, which is typical for industrial laser crystallization processes such as ELA. The full-width-at-half-maximum (FWHM) of a single pulse is 30 ns. The laser pulse energy was monitored using a calibrated pyroelectric energy meter, which received a fraction of the laser light from a beam splitter.

In order to obtain clean TR signals, it is necessary that the incident excimer-laser beam is spatially homogeneous. The beam was shaped by a telescope lens and then spatially homogenized through homogenizing optics to produce a spatially homogeneous beam. The beam was then further shaped by a patterned chrome mask and projected onto to the sample through a 5× demagnification projection lens with a numerical aperture of 0.13. The irradiated area on the samples was 1×1 mm^2.

3.2.2 *In Situ* Transient Reflectance

Our transient reflectance setup enables *in situ* probing of the spatiotemporal details of the melting transition with sub-nanosecond resolution. Optical transient reflectance measurements take advantage of the fact that optical parameters are temperature- and phase-dependent. Specifically, liquid silicon is much more reflective than solid silicon, owing to its metallic nature. As discussed in more detail in Section 3.4.1, the reflectance of an assembly of thin films (in this case, solid silicon and liquid silicon) depends on the thickness and the temperature-dependent optical properties of each layer. Thus as the silicon film undergoes melting, changes in reflectance can be observed.

The transient reflectance setup is as pictured in the schematics Figure 3.1. The setup consisted of two diode lasers operating at 670 nm and two fast, silicon-based photodiode detectors with rise times of less than 1 ns. The incident angles of the probe lasers were both at approximately 50° from the surface normal. In order to reduce stray ultraviolet light from the excimer laser and to obtain clear signals, the reflected beams passed through focusing lenses and UV filters before reaching their respective photodetectors. The TR signals were then recorded by a digital oscilloscope (Tektronix 3054C) with a maximum sampling rate of 5 Gs/s. To minimize delays between the signals, identical cables that were impedance-matched to the oscilloscope were used for collecting the surface-side TR, substrate-side TR, and incident beam intensity signals in all experiments. Signal smoothing was performed using a Savitzky-Golay filter [51] that optimized the signal-to-noise ratio while still retaining distinctive features in the signals.

It can be assumed that the collected TR signals probed an area where energy deposition was uniform due to the fact that the probed region was much smaller than the area on the sample that was irradiated using a homogenized beam. The visible spot diameter of the probe laser beam on the sample was around 0.2 mm, whereas the irradiated region was $1 \times 1\ mm^2$. Moreover, the homogenizing optics of the excimer-laser system resulted in spatially homogenized energy deposition of the incident beam.

3.3 Parametric Variation

In order to thoroughly examine the effects of the (100)-oriented Si-SiO_2 interface on melting, we varied the following parameters in this investigation:

1. **Surface treatment:** 50-nm LPCVD oxide or free surface (BHF-treated surface)
2. **Irradiation geometry:** Surface-side irradiation or substrate-side irradiation
3. **Energy density:** 150 mJ/cm^2 to 1900 mJ/cm^2

Our experimental design includes of all permutations of the above experimental configurations for a total of four different experimental configurations. For each experimental configuration, the energy density was varied from the minimum energy density for melting (as detected by TR) up to the maximum output energy density of our excimer laser.

3.4 Data Analysis

3.4.1 Thin-Film Reflectance Model

In situ transient reflectance data was analyzed using a thin-film interference approach. The reflectance of an assembly of thin films depends sensitively on the thickness and optical properties of each layer. Using the transfer matrix approached described in [52], we calculated the expected reflectance signals as a function of melt depth. Experimental temperature-dependent complex refractive indices for solid silicon [53], liquid silicon [54], and SiO_2 [55] were used in the calculations. For simplicity, we computed the surface-side and substrate-side reflectances as a function of the thickness of the liquid silicon layer near the thermodynamic melting point, assuming isothermal conditions. For higher temperatures, the values were extrapolated using linear regression.

The calculated reflectance signals qualitatively agree with what is expected and observed in experiments. The results are presented in Figure 3.3, which shows that if melting initiates at the

surface and propagates toward the substrate (such as in typical surface-side irradiation experiments), the surface-side reflectance saturates once the thickness of the liquid layer grows beyond a characteristic thickness whereas the substrate-side reflectance oscillates. If melting initiates at bottom interface (such as in certain substrate-side irradiation experiments), the reverse is true.

3.4.2 Heat Flow Analysis

Numerical simulations were performed using a software package called `3DNS` [14]. `3DNS` is capable of simulating nanosecond-timescale heat flow and first-order phase transitions (melting and solidification) in thin films undergoing pulsed-laser irradiation conditions. It can simulate the pulsed-laser irradiation process in one, two, or three spatial dimensions. Phase transitions at each interface (or homogeneously in the bulk) can be switched on or off. It utilizes a finite-difference scheme to calculate the heat flow and thermal evolution. The simulation mesh consists of orthorhombic nodes, each with its unique temperature-, phase-, and material-dependent thermal, thermodynamic, and optical parameters. In order to track solid-liquid interfaces in the film, it utilizes a non-equilibrium interface tracking algorithm and the interface response function.

The heat flow estimation is a critical part of `3DNS` that we utilize in this work. In the one-dimensional scenario, the time-dependent heat transport equation may be expressed as

$$c_p \frac{\partial T}{\partial t}(\phi, T) = \frac{\partial}{\partial z}\left(\kappa_T(\phi, T)\frac{\partial T}{\partial z}\right) + \dot{q}_L + \dot{q}_E, \tag{3.1}$$

where z is the position into the film (with the top surface defined at $z = 0$ and the Si-SiO_2 interface defined at $z = d_{film}$ where d_{film} is the film thickness), ϕ is the phase (solid or liquid) of the material, T is temperature, t is time, c_p is the heat capacity, κ_T is the thermal conductivity, $\dot{q}_L$ corresponds to the latent heat release at the solid-liquid interface, and $\dot{q}_E$ corresponds to the energy absorption of the incident beam and is described as [14]

$$\dot{q}_E(z,t) = I_0(t)\left|\tau(T)\right|^2\left[1-\exp\left(-\alpha(T)\right)\,dz\right]\left(\exp-\int_{d_{film}}^{0}\alpha(T)\,dx\right), \tag{3.2}$$

where I_0 is the beam intensity, $|\tau|^2$ is the absorption factor, and α is the absorption coefficient. For simulations that incorporate melting, the linearized form of the interface response function [56]

(Equation 2.1) was used. Due to the short timescale of the process, radiative and convective heat loss to the environment was ignored. Additionally, the possibly non-negligible (but very small, especially at high temperatures [57]) interface thermal resistance [58] between silicon and SiO_2 at the Si-SiO_2 interface [59] was neglected due to a lack of data at high temperatures. In order to accurately capture the non-isothermal and transient nature of the laser irradiation process, experimental values for heat capacity [14,60,61], thermal conductivity [14,62,63], normal-incidence reflectance [53], and normal-incidence absorption coefficients [53] of silicon and SiO_2 were used. Additionally, the experimentally obtained time-dependent intensity profile of the incident excimer laser beam was used. Further details describing the thermal analysis procedure can be found in Chapter 5.

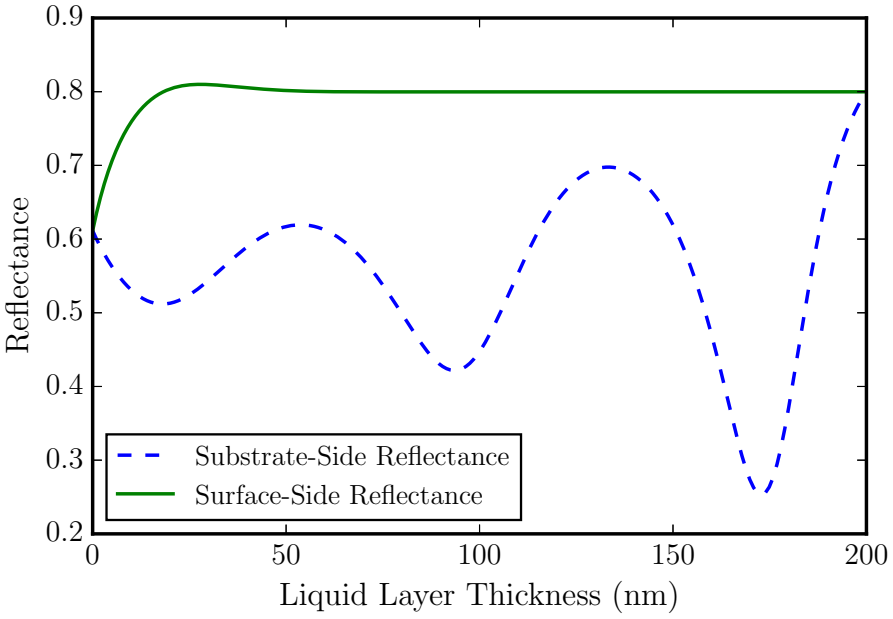

(a) Liquid layer initiating at and propagating from the surface side

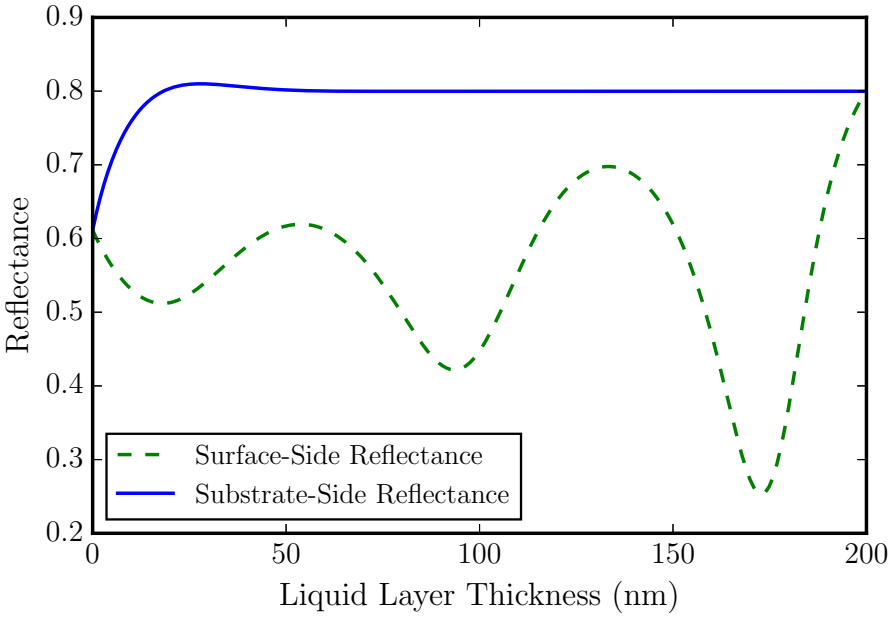

(b) Liquid layer initiating at and propagating from the substrate side

Figure 3.3: Computed reflectance for an incident angle of 50° and a wavelength of 675 nm assuming isothermal conditions at the equilibrium melting temperature of 1687 K.

Chapter 4

Experimental Observations of Superheating in Melting of Single-Crystal Silicon

In this chapter we present our experimental results that reveal significant superheating of solid silicon at and near the Si-SiO_2 interface during internal laser heating. This was accomplished via substrate-side laser irradiation of (100)-surface-oriented single-crystal silicon on a transparent fused-quartz substrate via an excimer-laser pulse. The spatiotemporal details of the melting transition was tracked *in situ* using surface-side and substrate-side transient reflectance (TR) measurements. From the TR signals, we observed melting at or near the buried Si-SiO_2 interface only under significantly higher laser fluences than what was required for melting at the oxide-free surface. This result can only be explained by the fact that, at least under the high heating rates induced via excimer-laser irradiation, a substantial degree of superheating is required to initiate melting at the (100)-oriented Si-SiO_2 interface.

4.1 Experimental Implementation

The excimer-laser system employed in the present experiments is described in Section 3.2.1. The full-width-at-half-maximum of the first peak of the excimer-laser pulse was approximately 30 ns. Due to the fact that time-dependent beam intensity profile varied slightly for each set of experiments, the time-dependent beam-intensity profile for each set of experiments is presented along with the *in situ* TR data. *In situ* surface-side and substrate-side TR was implemented using two diode lasers at 675 nm at 50° from normal incidence and two corresponding photodetectors. Details of the *in situ* TR implementation is described in Section 3.2.2. Since the energy density required to create an equivalent extent of melting in the same sample is highly sensitive to the time-dependent beam-intensity profile (which varied for each set of experiments), the energy density is normalized with respect to the complete-melting threshold (E_{CMT}), the minimum energy density required to induce complete melting of the film. The complete-melting threshold for each set of experiments was determined by irradiating the samples at various incident energy densities and analyzing the corresponding TR signals and optical micrographs.

In order to thoroughly examine melting at the (100)-oriented Si-SiO_2 interface, we examined substrate-side laser irradiation of the film as a function of the incident-beam-energy density in the following sets of experiments:

1. Substrate-side irradiation of 200-nm (100)-surface-oriented single-crystal silicon-on-quartz **after BHF surface treatment** (oxide-free surface)

2. Substrate-side irradiation of 200-nm (100)-surface-oriented single-crystal silicon-on-quartz **with a 50-nm surface oxide cap** (oxide-capped surface)

In order to examine for possible unexpected variables, we take advantage of the established understanding of the well-investigated case of pulsed-laser-induced melting resulting from surface-side irradiation [46] and performed additional sets of experiments using the same samples under the surface-side irradiation configuration as our experimental control:

1. Surface-side irradiation of 200-nm (100)-surface-oriented single-crystal silicon-on-quartz **after BHF surface treatment** (oxide-free surface)

2. Surface-side irradiation of 200-nm (100)-surface-oriented single-crystal silicon-on-quartz **with a 50-nm surface oxide cap** (oxide-capped surface)

In all experiments that require BHF surface treatment to remove the surface oxide, BHF-etching was performed immediately prior to excimer-laser irradiation. No more than 15 minutes elapsed from oxide removal to laser irradiation. A summary of the various experimental and sample configurations is shown in Table 4.1.

Irradiation Configuration	Surface Treatment
Surface-Side	Oxide-Capped
Surface-Side	BHF
Substrate-Side	Oxide-capped
Substrate-Side	BHF

Table 4.1: Table of the four experimental configurations in this chapter. Additionally, energy density was varied throughout the entire range for all four experimental and sample configurations.

4.2 Experimental Results

In situ TR signals obtained during laser irradiation are presented in this section. We first present the results of the most significant experiment of this work – substrate-side irradiation (i.e., internal heating) experiments performed at various incident energy densities. Since energy density is an important variable in these experiments, we organize the experimental results by their corresponding energy-density-dependent melting regimes, discussed in Section 2.4.1. We compare experiments on

BHF-treated samples with those on surface-oxide-capped samples for each melting regime at similar normalized incident energy densities (normalized with respect to E_{CMT}). Due to the fact that the time-dependent intensity profile of the incident excimer-laser beam fluctuated with each set of experiments, the corresponding temporal intensity profile of the excimer-laser pulse is presented with each set of experiments. The results of the surface-side irradiation experiments are presented in the latter part of this section for comparison.

4.2.1 Substrate-Side Irradiation

The substrate-side irradiation experiments, particularly the experiments performed on BHF-treated silicon, form the main result of this dissertation. For each melting regime (partial melting, complete melting, etc.), experiments performed on BHF-treated silicon are compared with those performed on surface-oxide-capped silicon in order to examine the effects of the Si-SiO_2 interface on melting.

In the substrate-side irradiation experiments, the TR signals show striking contrasts in the melting behavior of the BHF-treated sample compared to that of the surface-oxide-capped sample. Figure 4.1 presents TR signals obtained during substrate-side irradiation of (a) the BHF-treated sample and (b) the oxide-capped sample in the partial-melting regime. In the experiments performed on BHF-treated sample, the surface-side TR signals saturated whereas the substrate-side TR signal exhibited oscillatory behavior. In the experiments performed on the oxide-capped sample, the substrate-side TR signals saturated whereas the surface-side TR signals exhibited oscillatory behavior. As can be seen from the computed reflectance results in Section 3.4.1, the TR signals obtained during substrate-side irradiation of the BHF-treated sample show clear signatures of surface-side-initiated melting; whereas those of the oxide-capped sample show clear signatures of substrate-side-initiated melting.

At incident energy densities above the complete-melting regime, both the surface-side TR and substrate-side TR signals saturated as the film transformed completely into highly reflective liquid silicon. From Figure 4.2, it can be seen that in the experiments performed on the BHF-treated sample, the surface-side TR saturated before the substrate-side TR; in other words, melting initiated

Surface Treatment	Side Where Melting Initiates	Incident Energy Density
Oxide-Capped	Substrate	ALL
BHF	Surface	Up to 1.5 E_{CMT}
BHF	Surfacec AND Substrate	Above 1.5 E_{CMT}

Table 4.2: Summary of data from the substrate-side-irradiation experiments.

at or near the surface first. Whereas in the experiments performed on the oxide-capped sample, the substrate-side TR saturated before the surface-side TR; in other words, melting initiated at or near the bottom interface first. Interestingly, during substrate-side irradiation of the BHF-treated sample at sufficiently high energy densities, the oscillations in the substrate-side TR vanished as energy density increased (Figure 4.3). What is even more notable is that at extremely high laser fluences, the substrate-side TR of the BHF-treated sample finally rose before the surface-side TR, indicating that, at the very least, substrate-side-initiated melting occurred first only when irradiated at very high laser fluences. The implications of these results are discussed in Section 4.3. Table 4.2 summarizes the data shown in the *in situ* TR signals.

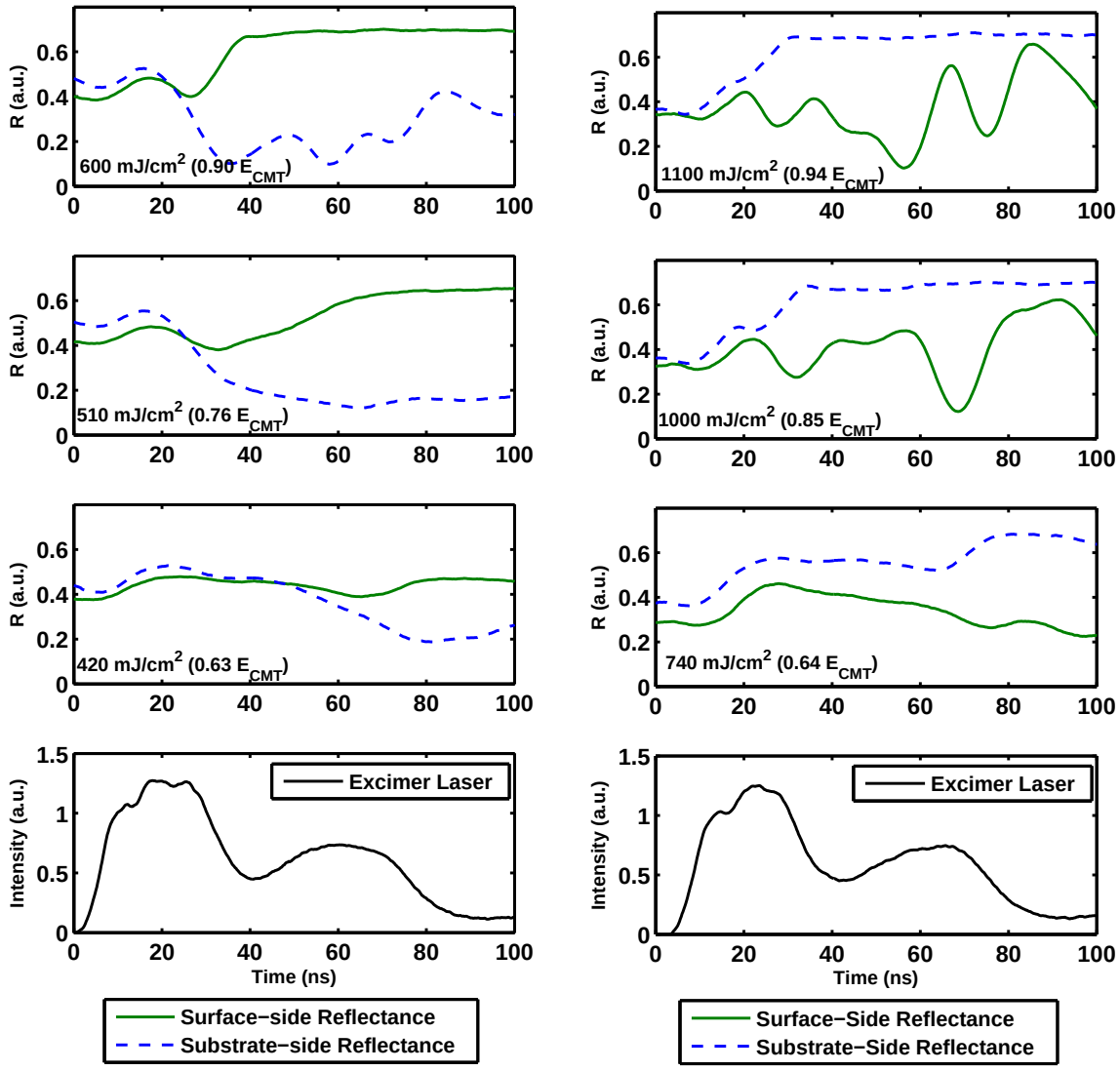

(a) BHF-treated surface

(b) Oxide-capped surface

Figure 4.1: *In situ* surface-side and substrate-side TR signals measured during substrate-side excimer-laser irradiation of (a) the BHF-treated sample and (b) the oxide-capped sample in the partial-melting regime. The time-dependent intensity profile of the incident excimer-laser pulse is presented in the bottommost subplots.

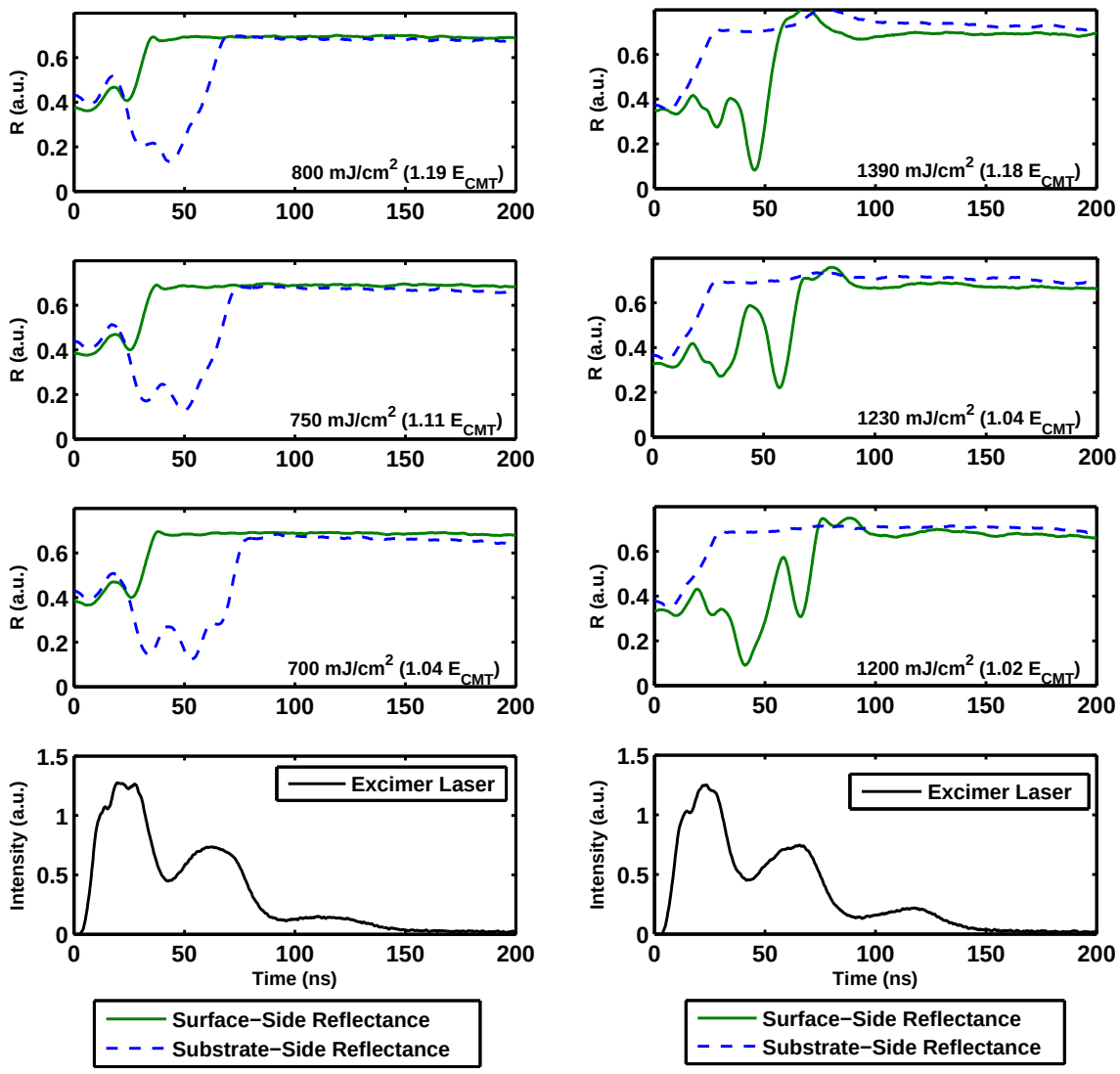

(a) BHF-treated surface

(b) Oxide-capped surface

Figure 4.2: *In situ* surface-side and substrate-side TR signals measured during substrate-side excimer-laser irradiation of (a) the BHF-treated sample and (b) the oxide-capped sample in the complete-melting regime. The time-dependent intensity profile of the incident excimer-laser pulse is presented in the bottommost subplots.

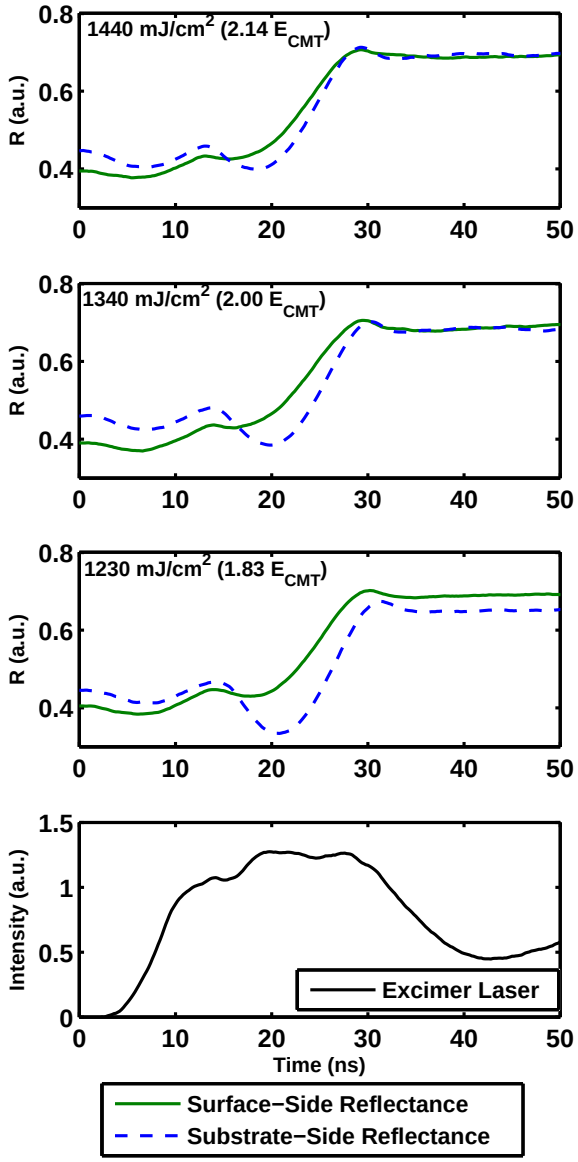

Figure 4.3: *In situ* surface-side and substrate-side TR signals measured during substrate-side excimer-laser irradiation of the BHF-treated sample well above the complete-melting regime. The time-dependent intensity profile of the incident excimer-laser pulse is presented in the bottommost subplot.

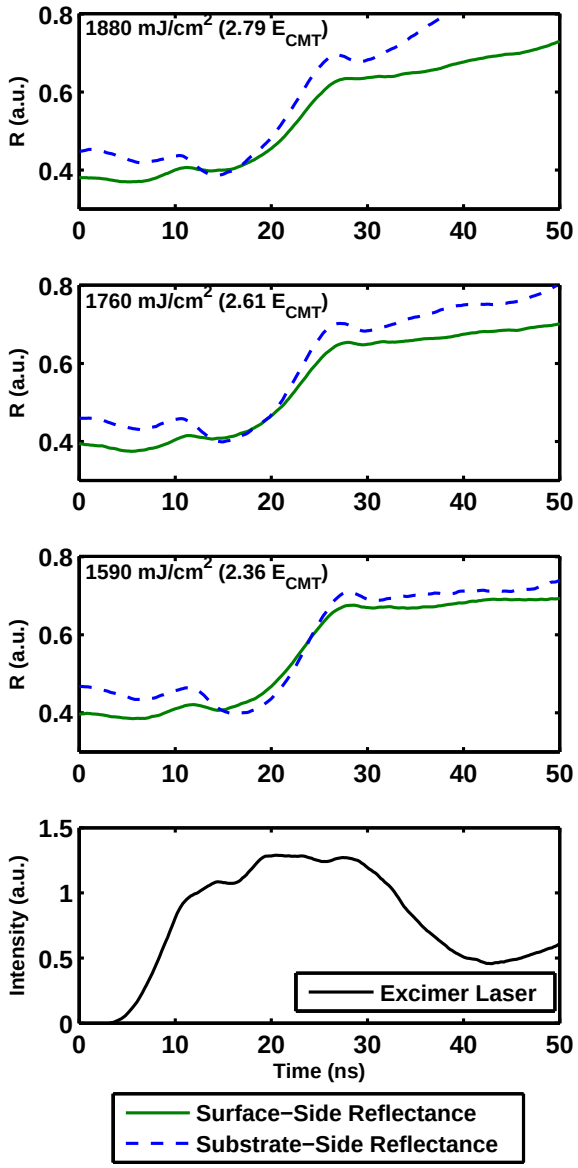

Figure 4.4: *In situ* surface-side and substrate-side TR signals measured during substrate-side excimer-laser irradiation of the BHF-treated sample at the highest energy densities capable that our laser is capable of. The time-dependent intensity profile of the incident excimer-laser pulse is presented in the bottommost subplot. Note that at above 30 ns, the large increase in reflectance after TR saturation was due to stray reflections of the intense excimer-laser beam.

4.2.2 Surface-Side Irradiation

Surface-side irradiation experiments of single-crystal silicon, particularly surface-oxide-free silicon, are well understood and serve as a useful experimental control in this investigation. For each melting regime (partial melting, complete melting, etc.), experiments performed on BHF-treated silicon are compared with those performed on surface-oxide-capped silicon in order to examine the effects of the Si-SiO_2 interface on melting.

In all of the surface-side irradiation experiments, irregardless of the existence of a surface oxide layer, melting initiated and propagated from the surface side. Figure 4.5 shows representative TR signals in the partial-melting regime for the BHF-treated sample (Subfigure (a) on the left) and the oxide-capped sample (Subfigure (b) on the right). As the liquid layer formed on the surface-side and grew in thickness, the surface-side TR eventually saturated. Meanwhile, the substrate-side TR exhibited sharp oscillations primarily due to the changing thicknesses of the solid and liquid layers, consistent with the model shown in Figure 3.3. Above the complete-melting regime, shown in Figure 4.6, once again, the surface-side TR saturated first but substrate-side TR saturation followed as the film transformed completely into highly reflective liquid silicon. A summary of the results of the surface-side irradiation experiments is shown in Table 4.3.

Surface Treatment	Side Where Melting Initiates	Incident Energy Density
Oxide-Capped	Surface	ALL
BHF	Surface	ALL

Table 4.3: Summary of data from the surface-side-irradiation experiments.

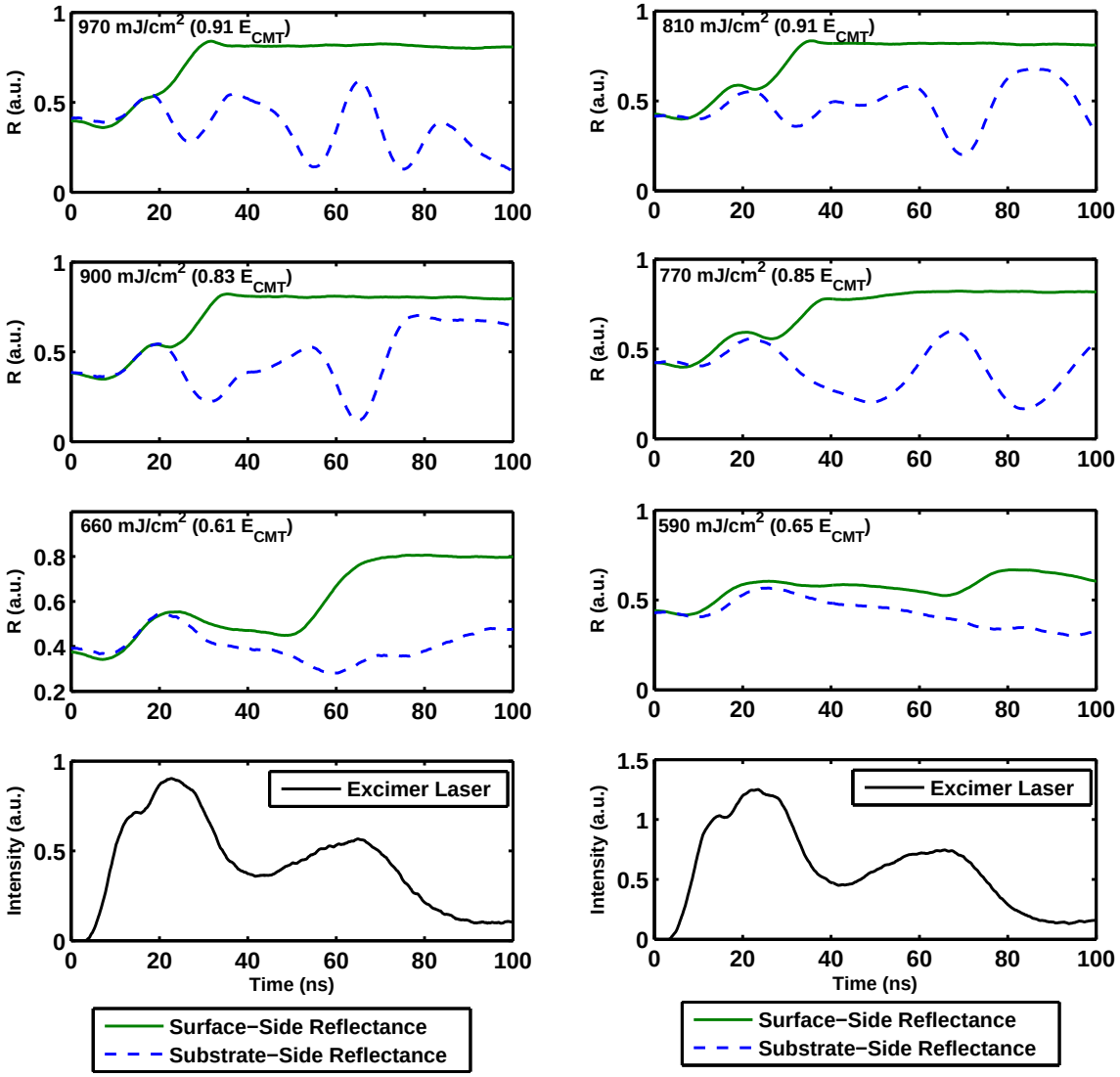

(a) BHF-treated surface

(b) Oxide-capped surface

Figure 4.5: *In situ* surface-side and substrate-side TR signals measured during surface-side excimer-laser irradiation of (a) the BHF-treated sample and (b) the oxide-capped sample in the partial-melting regime. The time-dependent intensity profile of the incident excimer-laser pulse is presented in the bottommost subplots.

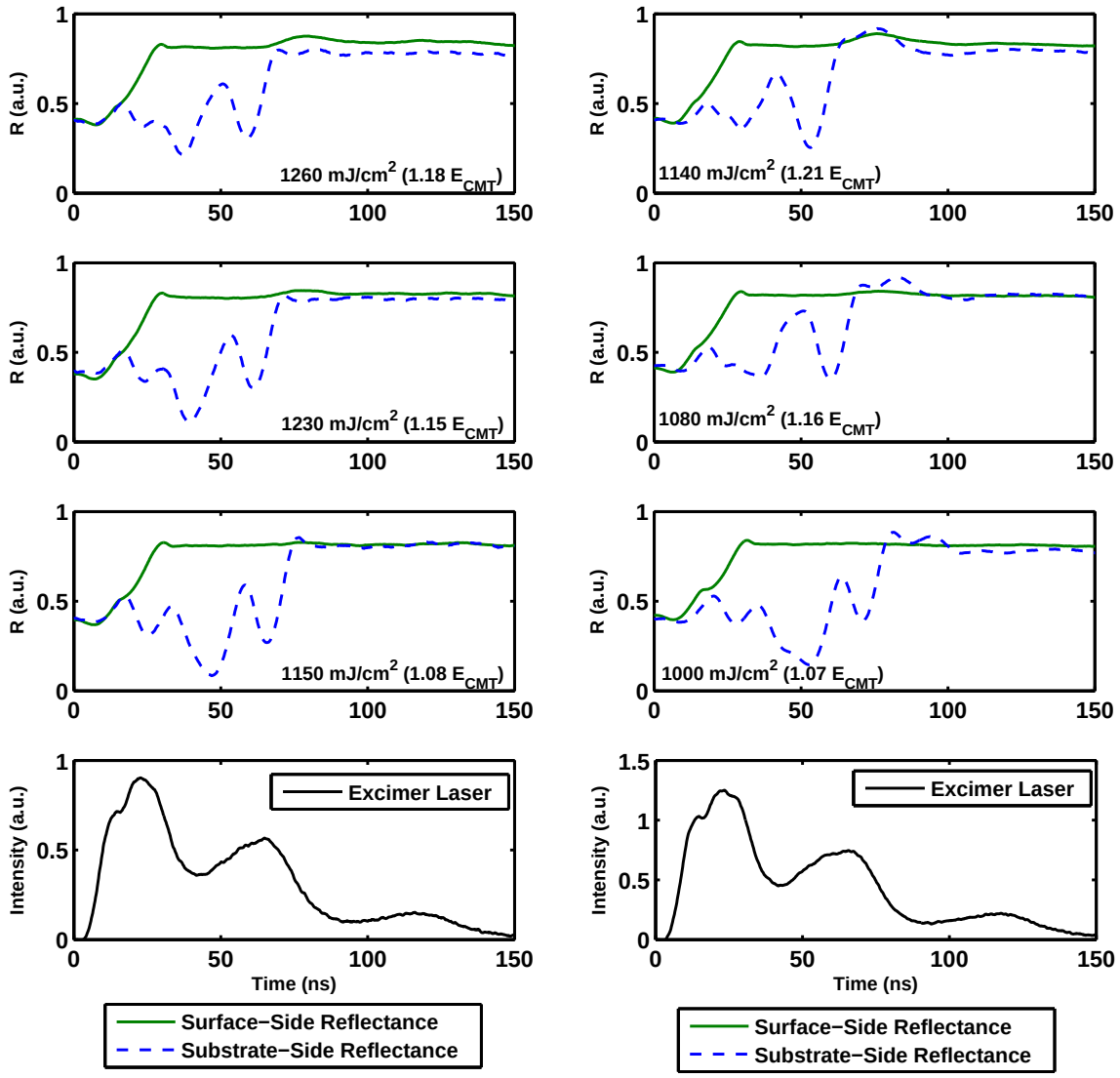

(a) BHF-treated surface

(b) Oxide-capped surface

Figure 4.6: *In situ* surface-side and substrate-side TR signals measured during surface-side excimer-laser irradiation of (a) the BHF-treated sample and (b) the oxide-capped sample in the complete-melting regime. The time-dependent intensity profile of the incident excimer-laser pulse is presented in the bottommost subplots.

4.3 Discussion

4.3.1 The Familiar Case of Surface-Side Irradiation

While the main result of this work lies in the substrate-side irradiation experiments, it is instructive to first examine the results of the surface-side irradiation experiments. Under surface-side irradiation, when considering the energy deposition and subsequent heat flow, one can deduce that the top surface is hottest and the bottom interface is coolest. This is due to the fact that the excimer-laser beam (which has a very small penetration depth in silicon) is directly incident on the top surface and heat dissipation from the film occurs nearly entirely through thermal conduction to the substrate at these short time scales. When further considering the fact melting usually initiates at the hottest region of the film, it is expected that we observe surface-side-initiated melting under these conditions, which is precisely what was observed in the present investigation. However, in substrate-side irradiation experiments, as discussed below, in addition to considering energy deposition and subsequent heat flow, due to the inverted thermal profile (when compared to that of surface-side irradiation experiments), one must additionally consider the thermodynamics and kinetics of melt-initiation at various material interfaces.

4.3.2 Superheating Along the Si-SiO_2 Interface

The substrate-side irradiation experiments demonstrate that superheating occurred along the Si-SiO_2 interface during pulsed-laser heating. The fact that melting initiated and propagated from the surface-side during substrate-side irradiation of the BHF-treated sample indicates that superheating must have occurred in the subsurface region of the film. Furthermore, melting must have occurred *at* the free surface (as opposed to *near* the free surface in the subsurface region of the film) when considering the fact that, at these heating rates, surface melting initiates at (or very near) the equilibrium melting point whereas a substantial degree of superheating is required for the internal homogeneous nucleation of liquid in the subsurface region of the film. The fact that we observed discontinuous surface melting (as opposed to pre-melting [20], which cannot be observed with our

experimental setup) and subsequent growth of the liquid layer in the TR signals immediately implies that the surface of the film had exceeded the equilibrium melting point. A consideration of the energy deposition and subsequent heat flow during substrate-side excimer-laser irradiation leads one to conclude that, during the heating period, the lowest temperature occurs at the surface whereas the hottest temperature occurs at or near the bottom interface. Thus, when one additionally considers the fact that surface melting must initiate at (or at least very near) the equilibrium transition temperature, the observation of surface melting under substrate-side irradiation must mean that a significant degree of superheating must had occurred in the subsurface region of the film, including along the Si-SiO_2 interface.

4.3.3 Internal Melting of the Film

In order to estimate of the degree of superheating required to initiate melting at or near the bottom Si-SiO_2 interface, the observations of substrate-side-initiated melting should be examined in detail. At energy densities well above E_{CMT}, substrate-side irradiation of the BHF-treated sample led to substrate-side-initiated melting. In Figure 4.3, it can be seen that despite the fact that the surface-side TR signals rose more promptly than the substrate-side TR signals, oscillations in the substrate-side TR signals disappeared. Additionally, it is notable that though the surface-side TR signals rose more promptly, the onset of saturation occurred near simultaneously for both sets of TR signals. Thus one may suspect that melting may have initiated at *both* the surface and at or near the bottom interface. In order to determine whether this was indeed the case, we assumed surface-initiated melting only (since the surface-side TR signals rose more promptly) and examined whether it is theoretically possible for the liquid layer to propagate from the surface down to the substrate in an amount of time denoted by Δt (defined in Figure 4.7). Using the linearized interface response function [56], the time-average velocity of the moving solid-liquid interface may be given as

$$\langle v_{int} \rangle = 0.26 \left(\langle T_{int} \rangle - T_m \right), \tag{4.1}$$

where $\langle T_{int} \rangle$ is the time-average temperature of the solid-liquid interface and T_m is the equilibrium melting temperature. The time-average velocity during the time in which the solid-liquid interface travels from the top surface to the bottom interface may be estimated as

$$\langle v_{int} \rangle = \frac{d - \delta}{\Delta t}, \tag{4.2}$$

where d is the film thickness, δ is the characteristic thickness of the liquid layer in order to observe saturation in the corresponding TR signal (approximately 20 nm), and Δt is the difference in time between the onset of saturation of the surface-side and substrate-side TR signals, as illustrated in Figure 4.7. Combining equations 4.1 and 4.2, and solving for the time-average interface temperature, we obtain

$$\langle T_{int} \rangle = \frac{d - \delta}{0.26\Delta t} + T_m. \tag{4.3}$$

Thus from Equation 4.3, it is immediately obvious that as $\Delta t \to 0$ (i.e., near-simultaneous onset of saturation for both the surface-side and substrate-side TR signals), $\langle T_{int} \rangle$ approaches unreasonably high values, meaning that the assumption of surface-initiated melting only at these high energy densities must be invalid. Using this analysis, we determined that the TR signals in Figures 4.3 and 4.4 must indicate that melting initiated both at the surface and at or near the bottom interface. The fact that substrate-side-initiated melting did not participate until at significantly higher energy densities indicates that the degree of superheating required to induce melting at or near the bottom Si-SiO_2 interface under these heating conditions must be substantial.

Closer examination of the substrate-side irradiation experiments on oxide-capped sample reveals more details pertaining to the degree of superheating at both the top and bottom oxide interfaces. In contrast to the BHF-treated sample (at moderate energy densities), melting in the oxide-capped sample initiated at or near the bottom interface under substrate-side irradiation. The primary difference between the two samples was that the BHF-treated sample lacked a surface oxide layer whereas the oxide-capped sample had a thin 50-nm oxide at the surface. The 50-nm oxide is expected to be thermally thin and only modestly affect the thermal environment. The drastically different melting dynamics induced by modifying the surface conditions (oxide-capped as opposed

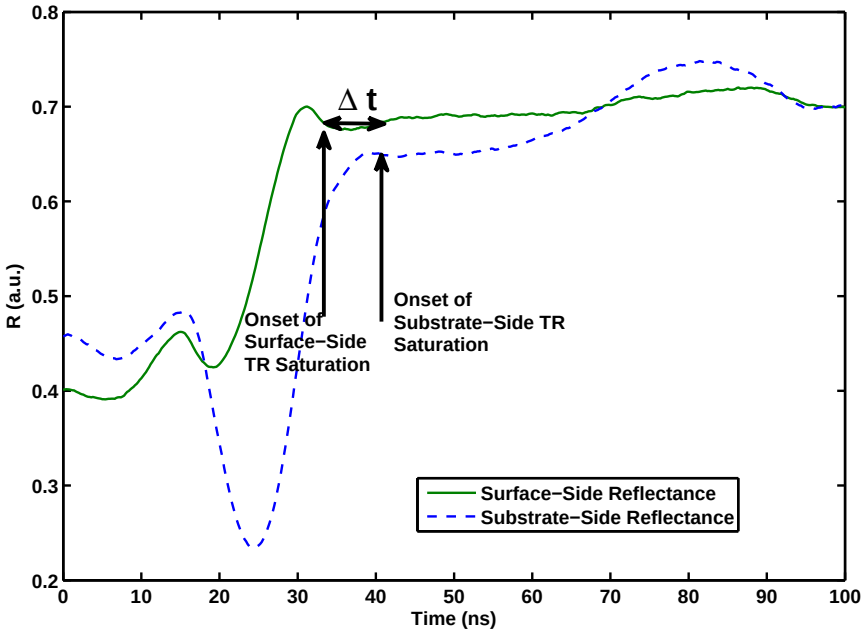

Figure 4.7: Representative set of TR signals in the complete-melting regime. The onsets of surface-side TR saturation and substrate-side TR saturation, respectively, are labeled. The difference in the onset of the surface-side TR saturation and the substrate-side TR saturation is denoted as Δt.

to free surface) indicate that both the top and bottom Si-SiO_2 interfaces must be very resistant to initiating melting. Furthermore, the melting threshold (defined as the minimum incident energy density required to induce a detectable amount of melting in the sample) under substrate-side irradiation is much higher for the oxide-capped sample (700 mJ/cm^2) than that of the BHF-treated (400 mJ/cm^2), which can be explained only by the fact that significantly higher temperatures are required to induce melting at the bottom oxide interface under these conditions. This large difference in the melting threshold between the two samples also indicates a substantial degree of superheating of the solid silicon at and near the top-oxide interface. Moreover, the fact that surface-side-initiated melting was not observed in the oxide-capped samples is consistent with our conclusion that, under the current heating conditions, melting at the top-oxide interface also requires significant degree of superheating.

4.4 Summary

In summary, we have demonstrated that the low-excess-free-energy (100)-oriented Si-SiO_2 interface can be highly resistant to catalyzing melting under excimer-laser irradiation. The results point to substantial superheating at and near the (100)-oriented Si-SiO_2 interfaces before the onset of melting. Inducing a substantial degree of superheating along a buried interface in a bulk solid is extremely challenging experimentally, and the present results offer an unusual opportunity to examine theoretical predictions of melting in superheated solids, which will be examined in the subsequent chapters.

Chapter 5

Thermal Analysis of the Observed Superheating

In this chapter, we present thermal analysis of the substrate-side irradiation experiments of the BHF-treated samples based on the *in situ* TR data presented in Chapter 4. The TR signals indicate a substantial degree of solid superheating in the subsurface region of the silicon film during excimer-laser irradiation. This observation of superheating in the subsurface region of the silicon film, and, in particular, along the Si-SiO_2 interface, may have significant scientific implications pertaining to various proposed models of melting in superheated solids. In order to examine these theoretical models, it is necessary to first obtain quantitative estimates of the degree of superheating in the film. It is possible to estimate the degree of superheating in experiments conducted on BHF-treated films since it is known that the free surface must trigger melting at (or at least very near) the equilibrium melting point. Using finite-difference-based calculations, we estimate that the solid silicon was heated up to 1.2 T_m before melting initiated at or near the bottom interface. We compare our result to theoretical predictions of the solid-phase superheating limit in silicon.

5.1 Description of the Computational Model

In order to accurately capture the time- and temperature-dependent parameters involved during the excimer-laser irradiation process, computational thermal analysis was performed for the corresponding experiments. A software package previously developed in our group, `3DNS`, was used to perform the thermal analysis. `3DNS` is a highly versatile numerical simulation program capable of providing accurate quantitative estimates of the transient thermal profile, melting, and solidification transitions during the excimer-laser irradiation process. The heat flow model used here has been shown to correspond closely to experimental data [14, 64].

Given the sufficiently planar interfaces in the single-crystal silicon observed during melting (which resulted in prominent oscillations in the TR signals that are indicative of a planar interface and a nearly one-dimensional melting-and-solidification scenario), melting can be approximated using a simple 1-D model. A major advantage of using a 1-D model over a 3-D model is the significantly higher computation speed which enabled the simulations to be completed in a reasonable amount of time on inexpensive hardware.

The 1-D thermal model utilizes a 1-D heat conduction equation that includes enthalpy generation/absorption and laser absorption, as described in Section 3.4.2. In the 1-D case, the simulation mesh consists of the silicon film and the fused-quartz substrate, which are divided into 1-D nodes of variable thicknesses. The program calculates and records the energy deposition, phase changes and interface movement, and the resulting heat flow for each time step. The time steps are adaptively adjusted during the simulation to ensure numerical stability while optimizing for computational efficiency. Details of the simulation algorithms and numerical methods can be found in Leonard's PhD Dissertation [14].

The simulation parameters were iteratively adjusted until the simulation yielded stable results. It was found that a node size of 4 nm, which divided the 200-nm silicon film into 50 nodes, yielded optimal results. The fused-silica substrate was divided into nodes of varying thicknesses, where the node sizes gradually increased away from the Si-SiO_2 interface in order to optimize compu-

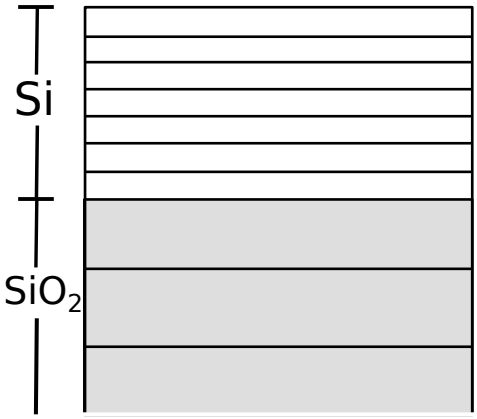

Figure 5.1: Schematic of the the simulation scheme. The materials are divided into "nodes" and the equations in the heat flow model are computed using a finite-difference method. Note that in this figure, for the sake of simplicity, the silicon layer is divided into only 7 nodes. In the simulations, the silicon layer was divided into 50 nodes of 4 nm each.

tation time. A simplified schematic diagram of the simulation geometry is shown in Figure 5.1. To accurately capture the non-isothermal and transient nature of the laser irradiation process, experimental values for heat capacity [14, 60, 61], thermal conductivity [14, 62, 63], normal-incidence reflectance [53], and normal-incidence absorption coefficients [53] of silicon and SiO_2 were used. A linearized interface response function obtained from experiments by Stolk et al. [56] was used. Additionally, the experimentally obtained time-dependent intensity profile of the incident excimer-laser beam from the corresponding experiment was used for each simulation.

5.2 Thermal Analysis

Based on the TR signals measured during substrate-side excimer-laser irradiation, one can qualitatively infer that the silicon film must had undergone a substantial degree of superheating. In order to quantitatively estimate the degree of superheating and analyze the kinetics of melting, it is necessary to perform thermal analysis of the experiments. Our thermal analysis begins by estimating the lower-bound superheating that the silicon film must undergo at the onset of melting

at the top surface during substrate-side excimer-laser irradiation. The lower-bound superheating is estimated to be the temperature of the solid silicon near the bottom interface at the time at which the top surface reaches the equilibrium melting point. As such, the lower-bound estimate only considers heat flow in the solid without considering melting and makes no assumptions regarding melting kinetics, establishing a firm lower-bound estimate of the superheating that transpired in the experiments. Once the lower-bound temperature estimates were established, we proceeded to estimate the maximum temperature reached in the solid silicon along the bottom Si-SiO_2 interface at moderate energy densities (below the energy density required to trigger melting from the substrate side) during the melting process. Lastly, we computed the temperatures to actually initiate melting at or near the bottom interface.

All of the analysis below were performed by examining experimental data obtained during substrate-side irradiation of the BHF-treated sample, where the free surface is exposed and not oxidized. This is due to the fact that the free surface is known to melt at (or very near) the equilibrium melting point, enabling us to define the equilibrium melting point as the surface melting temperature in the simulation. As such, the thermal analysis in the present chapter and subsequent theoretical analyses in Chapters 6 and A will focus on this particular set of experiments.

5.2.1 Estimated Superheating at the Onset of Surface Melting

First, we examined the temperature difference between the bottom interface and the top surface of the silicon film at the time at which the top surface node reaches T_m in the simulations for the range of incident energy densities used in the experiments. By utilizing the fact that melting at the surface must initiate at (or at least very near) the equilibrium melting point ($T_m = 1687\ K$), and, additionally, that, at these lower incident energy densities, melting initiated from the surface, it is possible to determine the temperature of the silicon along the bottom Si-SiO_2 interface at the onset of surface melting using `3DNS`. This condition is illustrated in Figure 5.2 Since the the beam is still incident on the silicon film after the onset of surface melting, the analysis in this section is a lower-bound estimate of the actual maximum superheating that transpired in the solid silicon

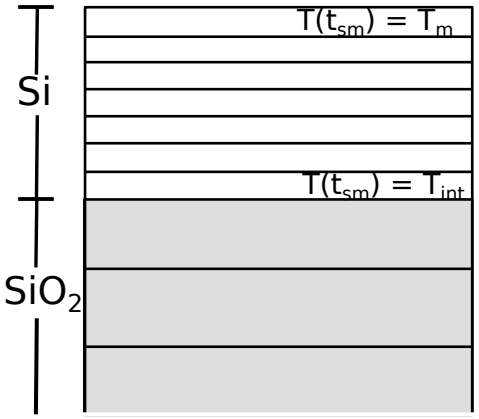

Figure 5.2: Schematic of the condition during the calculation at which the temperature of the top surface reaches the melting point, T_m, at time t_{sm}. At time t_{sm}, the bottom interface reaches a temperature of T_{int}. The interface must have reached at least this temperature during the experiment.

along the bottom interface.

5.2.1.1 Procedure

Here, we analyzed the substrate-side irradiation experiments on the BHF-treated samples at energy densities throughout the entire range of energy densities corresponding to those from experiment. We note that this analysis is valid for experiments at all incident energy densities that did not induce substrate-side-melting before the onset of surface melting. Representative TR signals obtained during substrate-side excimer-laser irradiation at these energy densities are shown in Figures 4.1 and 4.2.

In order to optimize the accuracy of the simulation results, it is necessary to first calibrate the simulation to the experiment. Thus instead of using raw energy-density units, in the simulations, we scaled the energy densities in terms of the melting threshold (E_{MT}). The melting threshold is defined as the minimum required energy density to induce melting, in this case, at the surface. The complete melting threshold (E_{CMT}), or the threshold energy density required to induce complete melting of the film, is then just a constant multiple of E_{MT}. Once the experimentally energy

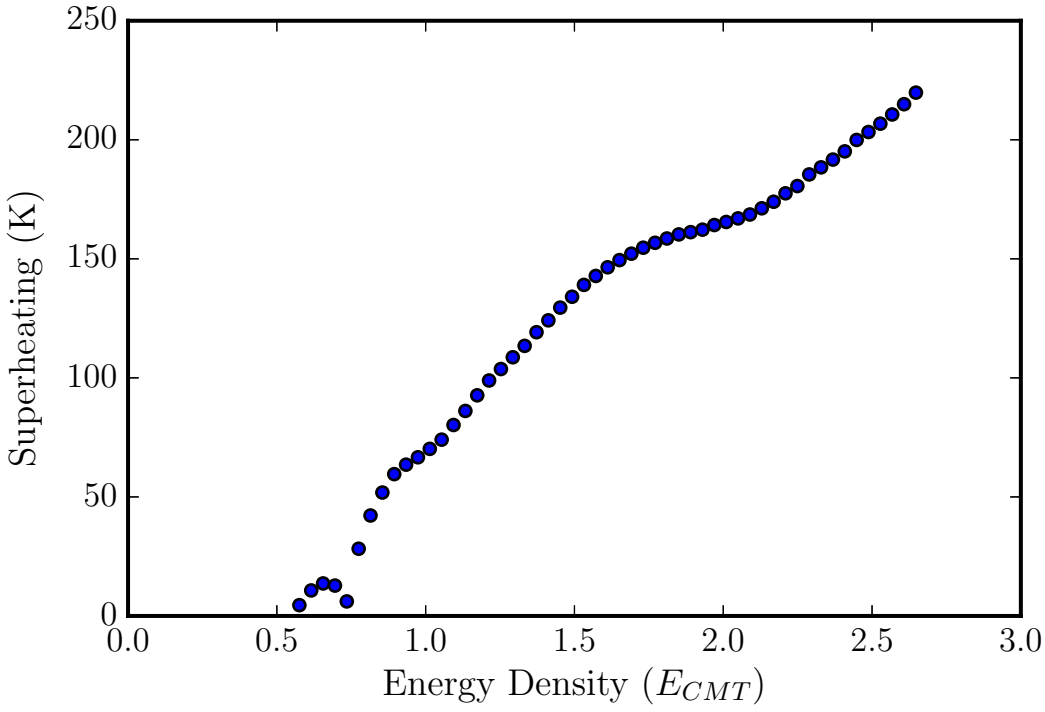

Figure 5.3: Estimated superheating of solid silicon as a function of incident energy density along the bottom Si-SiO_2 interface at the onset of surface melting. The near-substrate superheating increases with increasing energy density as expected, except at very low energy densities. This is due to the time-dependent intensity profile of the incident double-peak beam.

densities were converted into units of E_{MT}, we performed simulations at energy densities in the range corresponding to that of experiment. In the current set of simulations, melting was forced to not initiate anywhere in the film; thus, only beam absorption and heat flow in the untransformed solid were considered. For each simulation, the temperature of the silicon node immediately adjacent to the substrate node was recorded when the temperature at the top surfaces reached $T_m = 1687\ K$. This temperature is the estimated superheating at the time at which the top surfaces reaches the melting point, i.e., at the onset of surface melting.

5.2.1.2 Results

It was found that at the time at which the surface reaches the melting point, the region in the silicon film immediately adjacent to the substrate is the hottest region of the film. Moreover, the solid silicon along the bottom Si-SiO_2 interface could be heated up to 220 K above the melting point. From Figure 5.3, it can be seen that the estimated superheating at the onset of melting ranges from nearly zero at the lowest energy density up to 220 K at the highest energy density.

5.2.1.3 Discussion

The lower-bound superheating estimates presented above clearly indicates that superheating was experimentally observed. Note that since the lower-bound superheating estimates are temperatures taken at the bottom Si-SiO_2 interface at the onset of surface melting, the expected maximum superheating that occurred in each of these experiments is expected to be much greater since the beam is still incident on the sample after the onset of surface melting. Thus, in order to induce melting from the substrate-side (i.e., at or near the bottom Si-SiO_2 interface), temperatures well in excess of 220 K See Figure 5.3 may be necessary. A more detailed discussion of this result is presented in [65].

5.2.2 Estimated Maximum Observed Superheating in the Surface-Initiated Melting Regime

Now that we have quantitatively estimated the minimum degree of superheating of the solid silicon along the bottom Si-SiO_2 interface at the onset of surface melting, we proceed to estimate the maximum superheating that transpired in the sample during substrate-side irradiation at moderate incident energy densities at which melting initiated from the top surface only.

5.2.2.1 Procedure

Here, we continue our analysis by examining the set of TR signals obtained during substrate-side irradiation of the BHF-treated samples.

The thermal analysis procedure consists of two steps:

1. First, we performed a set of simulations to determine the energy threshold for substrate-side-initiated melting – above which, melting initiated from the substrate-side.

2. Next, we performed a series of simulations at energy densities below the substrate-side-initiated-melting regime in order to estimate the maximum superheating in the solid in this melting regime.

In order to determine how to proceed in developing procedures to estimate the maximum superheating that transpired in the sample, it is first necessary to determine the threshold energy density above which melting may additionally initiate from the substrate-side. It is possible to determine this threshold energy by performing simulations that assume surface-initiated melting only (i.e., by disabling substrate-initiated melting in the simulation) and then comparing the simulated results with the corresponding experimental results at various energy densities. Using the experimental results presented in Chapter 4, we analyzed the difference between the onset of saturation of the substrate-side TR signal and the corresponding surface-side TR signal.

This difference between the onset of saturation of the substrate-side TR signal and the corresponding surface-side TR signal is illustrated in Figure 4.7 and is denoted as Δt. In the present analysis, we compare the simulated Δt with the experimental Δt. It is expected that at energy densities below the substrate-side-initiated-melting threshold, the simulated Δt should be reasonably close to that of experiment. And, at energy densities above the substrate-side-initiated-melting threshold, the simulated Δt should be much greater than those that obtained from experiment since the simulations in this section assume surface-initiated melting only. This is due to the fact that, above the substrate-side-initiated melting threshold, melting initiates concurrently from both

the surface and the substrate-side, leading to a near-simultaneous rise in both the surface-side and substrate-side reflectance signals, resulting in a small Δt.

In this section, we present our maximum superheating estimates at energy densities below the substrate-side-melting threshold. We performed simulations in order to estimate the maximum temperature of the solid silicon along the bottom Si-SiO_2 interface as a function of incident energy density. The simulations here assumed surface-initiated melting only (i.e., substrate-initiated melting was disabled). The maximum temperature that the near-substrate silicon node whilst it remained solid was then extracted from the simulation output for each incident energy density.

5.2.2.2 Results

The surface-side-melting-only simulations in Figure 5.4 reveal that, at energy densities up to 1.5 E_{CMT}, the simulated Δt corresponds very well to the experimental Δt. However, at energy densities above 1.5 E_{CMT}, the simulated Δt starts to significantly deviate from the simulated Δt. Thus, at energy densities below 1.5 E_{CMT}, melting is initiated only from the surface; whereas at energy densities above 1.5 E_{CMT}, the melting scenario enters into a regime where melting is initiated concurrently from both the surface and substrate sides. This estimate that substrate-side initiated melting occurs at energy densities above $\sim$1.5 E_{CMT} is consistent with our estimate in Chapter 4.

The analysis showed that superheating of up to 330 K was observed at energy densities below the substrate-side-melting threshold. Comparing Figure 5.3 and Figure 5.5, it can immediately be seen that the estimated superheating from the current analysis yielded values that are greater than those from the lower-bound analysis. As with the lower-bound analysis, it can be seen that, in the present analysis, the maximum superheating is positively correlated with the incident energy density.

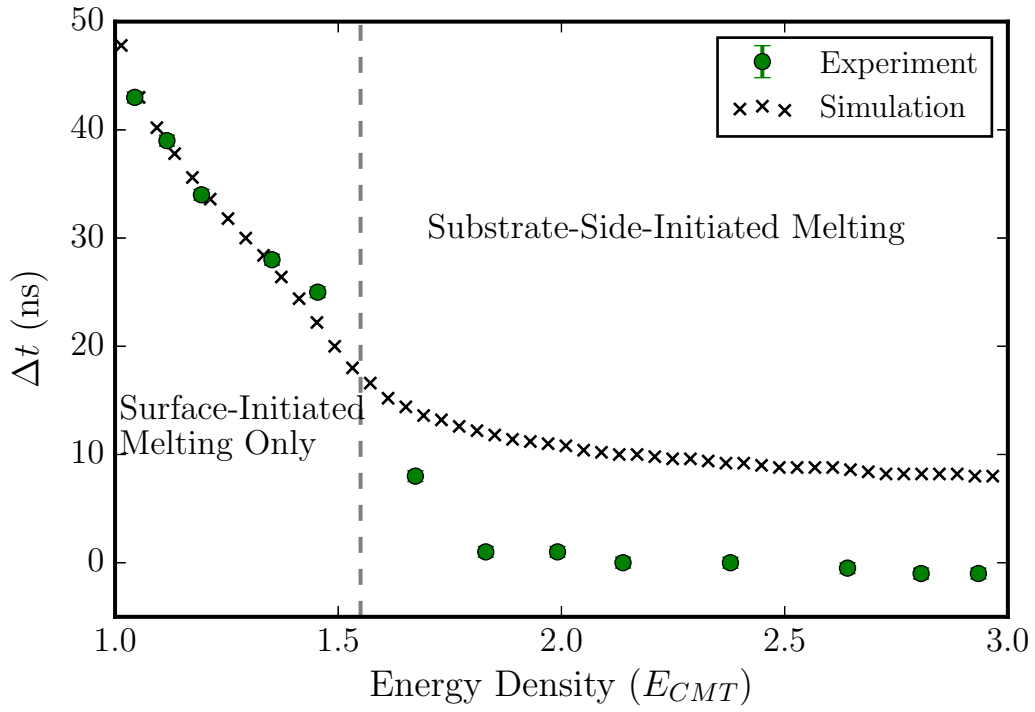

Figure 5.4: Difference between the onset of substrate-side TR saturation and that of surface-side TR saturation (defined as Δt) as a function of energy density. The simulated Δt deviates from the experimental Δt at energy densities above $\sim$1.5 E_{CMT}. The substrate-side-initiated melting threshold thus is estimated to be $\sim$1.5 E_{CMT}.

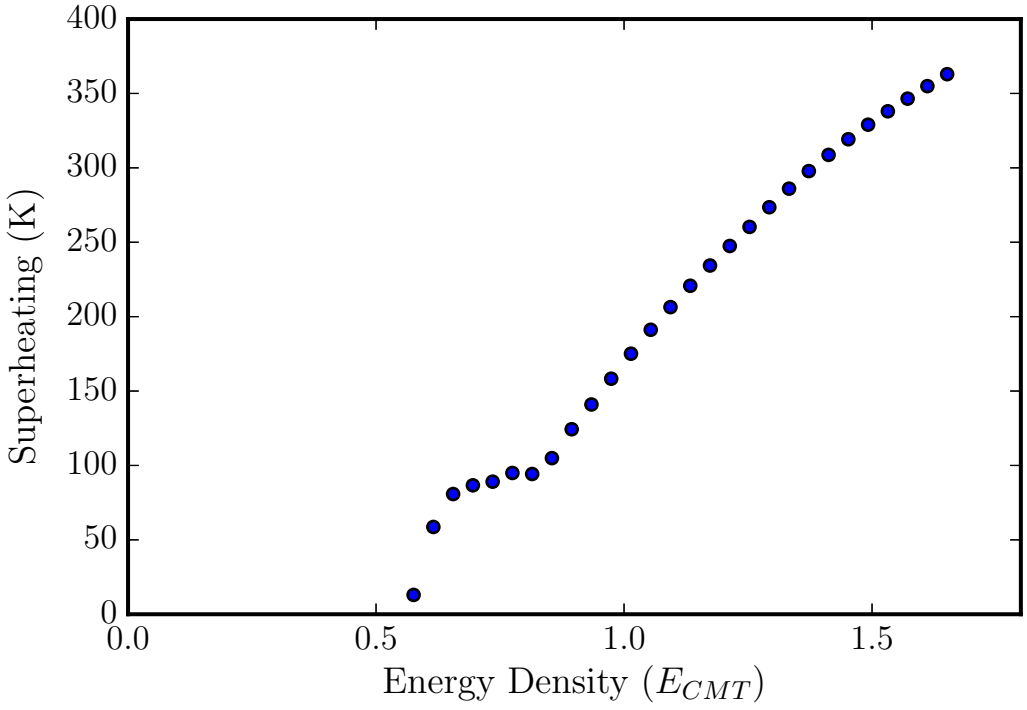

Figure 5.5: Estimated maximum superheating of the solid silicon along the bottom Si-SiO_2 interface during the pulsed-laser-induced melting process at energy densities below ~1.5 E_{CMT}.

5.2.2.3 Discussion

The simulated results agree very well with the experimental TR data presented in Chapter 4. Figure 5.4 clearly demonstrates this agreement. At energy densities up to the substrate-side-melting threshold ($\sim$1.5 E_{CMT}), the simulated Δt corresponds extremely well with the experimental Δt, where we concluded from the TR signals that melting initiated and propagated only from the top surface.

However, at energy densities above the substrate-side-melting threshold, the simulated data deviate significantly from the experimental data; the simulated Δt become much smaller than the experimental Δt. This is consistent with our conclusion in Chapter 4 that, based on qualitative analysis of the TR signals, at energy densities above the substrate-side-melting threshold, melting initiated at or near the bottom interface in addition to the surface. When melting initiates concurrently from both the surface side and the substrate side, when considering the fact that liquid silicon is much more reflective than solid silicon, both the surface-side TR and the substrate-side TR nearly simultaneously increase, resulting in a very small Δt. Since, in the simulations, only surface-initiated melting was enabled (substrate-initiated melting was forbidden), the simulated Δt are much larger than the experimental Δt above the energy density where substrate-side-initiated melting was also observed. The simulations here also predicted a substrate-side-melting threshold that corresponds with the analysis of the experimental TR signals from Chapter 4. This excellent agreement between simulation and experiment indicates that we have selected appropriate parameters describing the corresponding melting kinetics.

As expected, the estimated maximum superheating at energy densities below the substrate-side-melting threshold is greater than the previous lower-bound estimates. The fact that the maximum superheating is positively correlated with the incident energy density is due to the fact that the temperature gradient in the film increases as energy density is increased. This is also consistent with our lower-bound estimates. Here, the estimated maximum superheating, while still not triggering melting from the substrate-side, is 330 K. Thus, it is expected that superheating in excess of 330 K

is required in order to trigger melting of the solid silicon at or near the bottom Si-SiO_2 interface. Using these lower-bound values as a sanity check, we proceed to compute the actual temperatures required to trigger melting of solid silicon, under the heating conditions encountered in the present experiments, along the bottom Si-SiO_2 interface.

5.2.3 Estimated Temperatures to Induce Melting at the Bottom Si-SiO_2 Interface

So far, we have presented thermal analysis at incident energy densities below the substrate-side-melting threshold. The lower-bound estimate yielded a maximum value of 220 K and the maximum superheating estimate yielded a maximum value 330 K. Since at these energy densities below the substrate-side-melting threshold, melting only initiated at the top surface, these values are expected to be less than what is required to actually initiate melting at or near the bottom interface. In order to estimate the temperatures required to trigger melting of solid silicon at or near the bottom interface, it is necessary to perform thermal analysis on experiments at and above the substrate-side-melting threshold. In this section, we present our procedure for computationally extracting these temperatures and the subsequent results of this analysis.

5.2.3.1 Procedure

Building upon our previous analysis, we proceed to estimate the temperature of the solid silicon along the bottom Si-SiO_2 interface required to trigger melting. In this procedure, we performed a series of simulations that allow for melting to initiate at both the top surface and the bottom interface. As in the previously presented simulations, melting was triggered at the top surface at T_m. Melting, at the bottom interface, however, was triggered at different temperatures for each simulation. In other words, this "bottom-side melting temperature" is the parameter that was fitted to experimental data. In order to determine the range of values to use for the bottom-side melting temperature, we referred back to our previous lower-bound estimates for the minimum value and the "homogeneous nucleation temperature" (i.e., the temperature at which homogeneous

nucleation of liquid silicon in solid silicon becomes significant) estimated for the current heating rates for the maximum value [66]. The bottom-side melting temperature was varied from 1900 K to 2290 K with a step size of 5 K. The time at the onset of substrate-side-initiated melting was then recorded for each experiment. The energy density was varied from 1.8 E_{CMT} to 2.95 E_{CMT} with a step size of 0.05 E_{CMT}. In order to account for errors in estimating Δt, Δt as a function of energy was then extrapolated from the experimental data using linear regression and compared to the corresponding simulation. The estimated temperature, including its uncertainty, required to trigger melting at or near the bottom interface for each incident energy density is taken to be the range of temperatures that correspond to $\Delta t \pm 0.5$ ns from the regression line. Additionally, in order to examine whether melting was triggered at the interface or adjacent to it, we computed the hottest location in the silicon film for each time step.

5.2.3.2 Results

The estimated superheating to initiate melting at or near the bottom Si-SiO_2 interface is 370±35 K, corresponding to absolute temperatures of 1.20 to 1.24 T_m. The heating rate and near-substrate temperature of the silicon as a function of time for an incident energy density of 2.0 E_{CMT} is shown in Figure 5.9. The heating rate when the near-substrate temperature increased above the equilibrium melting point is estimated to be between $1 \times 10^{10}\, K/s$ and $5 \times 10^{10}\, K/s$. Figure 5.8 shows the estimated superheating at and near the bottom Si-SiO_2 interface as a function of incident energy density. Additionally, it was found that the hottest temperature in the film was in the simulation node right above the bottom Si-SiO_2 interface, i.e., the bottom 4 nm of the silicon film.

The analysis was performed by examining Δt as a function of the bottom-side melting temperature for each energy density. The simulated Δt was calculated from the thicknesses of the solid and liquid layers as a function of time. Representative plots of the temperature and phase information as a function of time obtained from the simulation is shown in Figure 5.6. A representative plot of Δt as a function of the bottom-side melting temperature at an incident energy density of 2.00 E_{CMT} is shown in Figure 5.7. Experimentally, Δt for the experiment performed at this energy

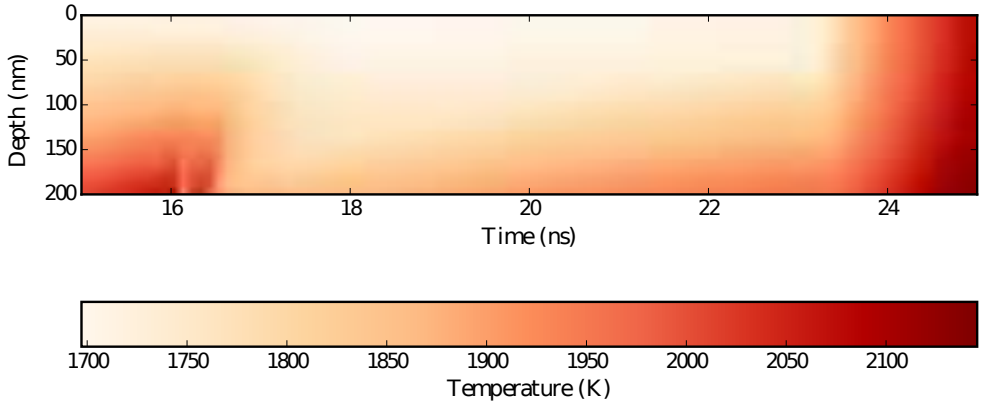

(a) Temperature as a function of position and time.

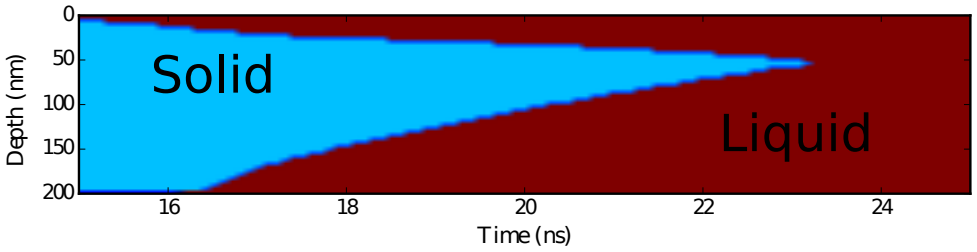

(b) Phase (solid or liquid) as a function of position and time.

Figure 5.6: Representative plots showing the simulated temperature and phase as a function of position and time for an incident energy density of 2.1 E_{CMT} assuming a bottom-side melting temperature of 2050 K. Here, 0 nm corresponds to the top surface and 200 nm corresponds to the Si-SiO_2 interface. These calculations were performed over a range of incident energy densities and bottom-side melting temperatures to calculate Δt, in order to fit the experimental data and generate the plot in Figure 5.8.

density was 0.7 ± 0.5 ns. Thus, by matching the simulated Δt with its corresponding experimental value, we were able to provide an estimate for the temperature of the solid silicon along the bottom Si-SiO_2 interface required to trigger melting. The points that lie in the region between the two gray lines (that correspond to the range of estimated Δt for that particular laser fluence) marks the range of predicted temperatures. The same procedure was repeated for each experiment. The

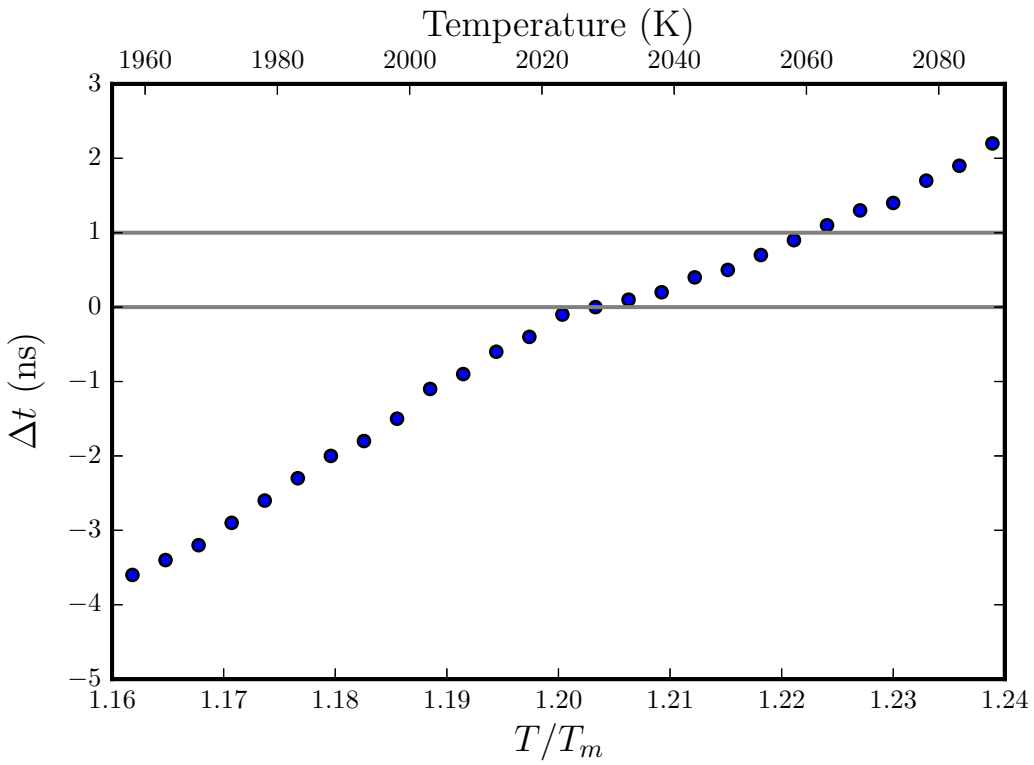

Figure 5.7: A representative plot of simulated Δt as a function of the homologous temperature required to trigger melting at the bottom interface ($T_{m,bottom}/T_m$). This set of simulations was performed at an incident energy density of 2.00 E_{CMT}. The points that lie region between the two gray lines (which correspond to the range of Δt from the experimental data) correspond to the range of estimated temperatures. For this energy density, $T_{m,bottom}/T_m \approx 1.21 \pm 0.1$.

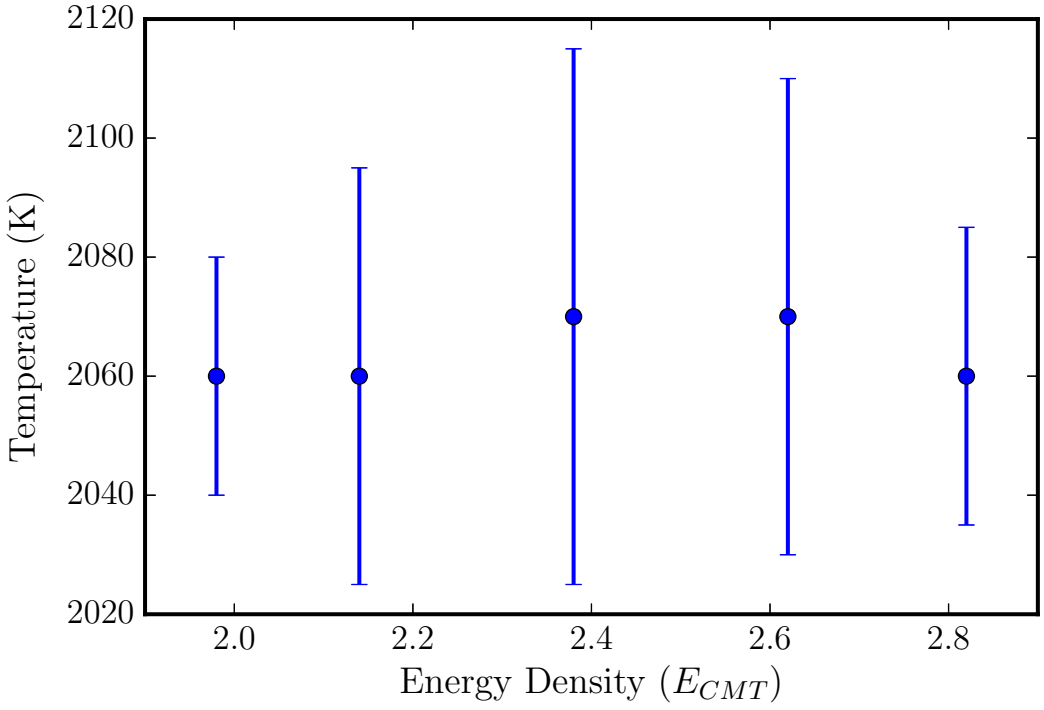

Figure 5.8: Estimated temperature required to trigger melting along the bottom interface as a function of incident energy density.

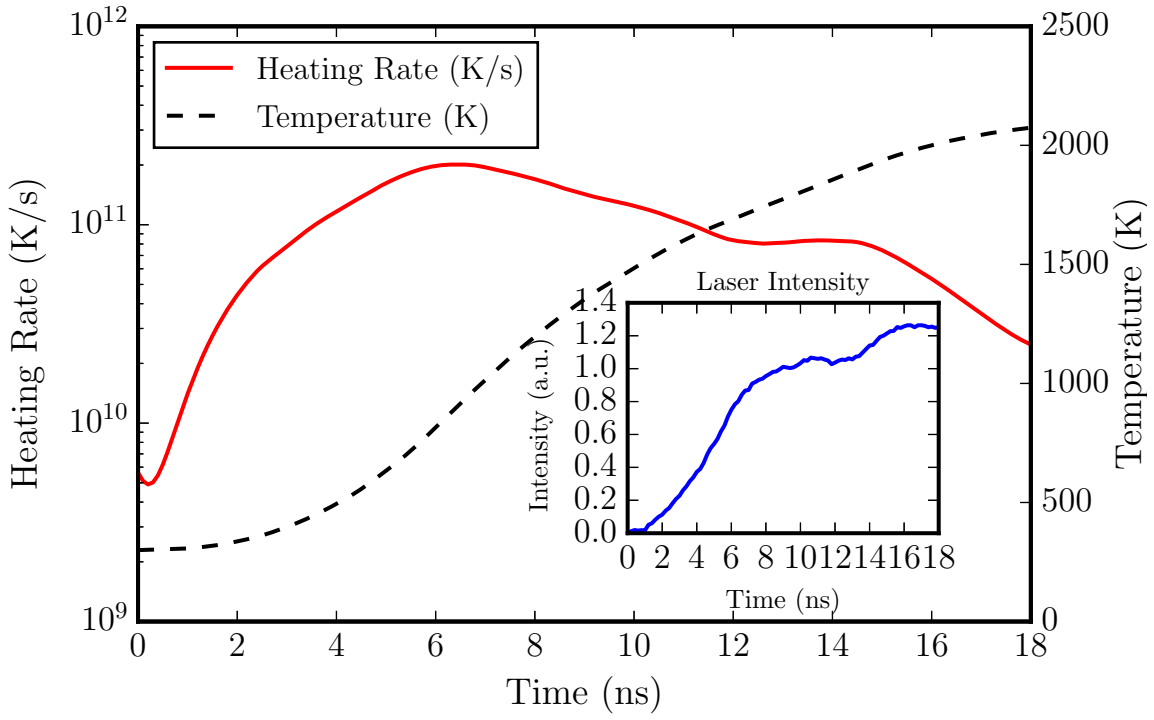

Figure 5.9: Computed heating rate and near-substrate temperature of the silicon as a function of time for an incident energy density of $2.0\,E_{CMT}$. The time at the onset of melting is $20\,ns$. The inset figure shows the time-dependent intensity profile of the incident excimer-laser beam.

data is summarized in Figure 5.8.

5.2.3.3 Discussion

In this section, we have presented our estimate of the degree of superheating in order to trigger melting at or near the bottom Si-SiO_2 interface under the present experimental conditions. Our estimated superheating of $370 \pm 35\ K$ is consistent with the previous estimates: The estimated value in order to actually trigger melting at or near the bottom interface is greater than our lower-bound estimates. The fact that the near-substrate region of the silicon film is the hottest during the pulsed-laser heating process justifies our assumption of substrate-catalyzed melting in the simulation. However, this does not necessarily imply that melting was heterogeneously catalyzed by the substrate. Thus the current data in itself does not rule out the possibility of the homogeneous initiation of liquid within the bulk silicon near the bottom interface, provided that it is energetically and kinetically favored. Further analysis regarding the mechanism of melting is presented in the subsequent chapter. Here, we discuss the significance of the degree of superheating observed in the present experiments and what it could mean regarding possible mechanisms of melting in our experiments.

5.3 Discussion: Possible Melting Mechanisms

Our thermal analysis reveals that during pulsed-laser-induced heating and melting, single-crystal silicon films can be substantially superheated – up to 370 K or 1.22 T_m – before inducing internal melting at or near the bottom Si-SiO_2 interface. This is indeed a substantial degree of superheating, comparable with experimental reports of superheating and melting near the theoretical superheating limit [43]. In order to further examine the mechanism of melting in the present study, including whether melting initiated immediately at or approximate to the bottom interface, it is worthwhile to compare the present result to theoretical predictions of the maximum superheating limit.

5.3.1 Liquid Nucleation as a Mechanism of Melting in Superheated Solids

As discussed in Chapter 2, at typical heating rates encountered in experiments (including the present experiments), nucleation theory predicts the lowest maximum superheating limit out of all the theories. As such, it is fruitful to examine the results of superheating experiments in the framework of classical nucleation theory, which is often used to model phase transitions in simple elemental systems. By examining the experimental results in light of classical nucleation theory, one may derive fundamental insights regarding the mechanism of melting – e.g., whether it is homogeneous or heterogeneous. Using classical nucleation theory, Luo et al. [43] analyzed the results of myriad superheating experiments on various materials. Their data analysis provided empirical formulas that demonstrated excellent agreement to many experimental data points over many experiments. Based on their analysis, the upper superheating limit of silicon at a heating rate of 10^{10} K/s, which is the estimated heating rate in the present experiments, is approximately 1.2 T_m. However, in a molecular dynamics simulation study by Zhang et al. [66], at a heating rate of 10^{11} K/s, liquid nuclei did not form in the crystalline silicon until a temperature of 2290 K (1.36 T_m) or at 611 K of superheating. Yet, in another molecular dynamics study by Nieves et al. [67], liquid nuclei did not form until a superheating of 538 K (1.32 T_m) for crystalline silicon. In contrast, in a simulation study done by Phillpot et. al, mechanical melting (i.e., elastic instability of the crystal) occurs at a higher temperature of 2400 K, 700 K above the melting point [68]. All of the above molecular dynamics studies used a large number of atoms and periodic boundary conditions. Nucleation analysis of the present dataset may suggest a probable mechanism of melting in the current experiments. Further analysis and discussion are presented in the subsequent chapter.

5.4 Summary

In this chapter, we have provided quantitative estimates of the degree of superheating required to initiate melting at or near the bottom Si-SiO_2 interface in the present experiments. Although it was qualitatively deduced in Chapter 4 that superheating must had taken place at and near

the bottom interface during pulsed-laser heating, computational methods are necessary due to the transient and temperature-dependent nature of many of the parameters. Using a software package called `3DNS`, previously developed in our research group to simulate pulsed-laser-induced melting processes, combined with experimental data, we developed procedures to provide consistent estimates of the degree of superheating required to initiate melting of silicon at or near the bottom Si-SiO_2 interface. The estimated temperature in order to trigger melting at or near the bottom Si-SiO_2 interface is approximately 1.2 T_m, which, to first order, is within range of the kinetic superheating limit predicted by certain classical nucleation models [43], assuming homogeneous nucleation of the liquid. Using our experimental results, we will critically examine these predictions as well as the possible mechanisms of melting in the subsequent chapter.

Chapter 6

Nucleation Rate Estimates

Considering the results presented in the previous chapters in light of theoretical models of melting in superheated solids, liquid nucleation is the expected mechanism of melting in the superheated silicon films. As such, using the TR signals and thermal analysis from Chapters 4 and 5, respectively, we use Johnson-Mehl-Avrami-Kolmogorov (JMAK) analysis to estimate the rate of liquid nucleation in the film. The result is then compared to classical nucleation theory in the subsequent chapter.

6.1 The Case for Liquid Nucleation

Various theoretical models have been developed in order to estimate the upper limit of superheating in a solid. An overview of the various models used to estimate the upper-bound superheating in a solid is presented in Section 2.3. Based on these theoretical models, Lu and Li [2] concluded that, under typical heating rates, homogeneous nucleation, which they described using classical nucleation theory, sets the upper limit of superheating in a solid. A consideration of computational studies [41, 43, 67] also suggests that the observed superheating in the present experiments correspond to a regime in which nucleation of the liquid phase is the expected mechanism of melting.

Nucleation is a thermodynamic and kinetic process that is extremely sensitive to the local temperature. In nucleation of liquid in a solid, the nucleation rate drastically increases as the local

temperature in the solid increases above the equilibrium point. At low heating rates, the nucleated liquid seeds are given sufficient time to grow and consume the remaining solid material, resulting in a lower kinetic superheating. On the other hand, at high heating rates, the nucleated liquid seeds do not have as much time to grow and consume the remaining solid, resulting in a higher kinetic superheating. Hence, when both nucleation and growth are considered, it is expected that, at high heating rates, the solid can be significantly superheated. Figure 6.1, reproduced from [2], shows a time-temperature-transformation (TTT) diagram that illustrates this kinetic dependence of the nucleation-rate-limited superheating for aluminum.

At extremely high heating rates, the kinetics are such that the solid may bypass homogeneous nucleation, enabling other melting mechanisms to transpire in the solid. Figure 6.1 shows that, at extremely high heating rates, the nucleation-rate-limited superheating exceeds the isentropic melting point [33]. It is further predicted that, for many solid materials, heating rates above ($> 10^{13}\,K/s$) may enable the solid to bypass homogeneous nucleation [12]. However, it has been noted that at such high heating rates, other factors such as the need for electron-lattice equilibration in laser heating [69] may control the onset of melting, leading to non-thermal melting of the superheated solid.

The experiments where melting was observed to initiated from the substrate-side correspond to a regime where nucleation of liquid is expected. The heating rates in the experiments where melting was induced along the bottom Si-SiO_2 interface was approximately $10^{10}\,K/s$, based on our thermal analysis in Chapter 5. This heating rate is well within the regime in which liquid nucleation is expected and below that in which non-thermal melting is expected. Moreover, the estimated observed melting temperature of $1.2\,T_m$ corresponds to the estimated upper limit of $1.2\,T_m$ predicted by Luo et al. [43] by fitting a large collection of experimental data to homogeneous classical nucleation theory. However, the estimated superheating in the present experiments is also much less than the homogeneous melting temperatures predicted by computational studies [66,67]. It is also much less than the predicted mechanical melting temperature for silicon [68], which is higher than that for homogeneous nucleation at these heating rates. In order to compare our

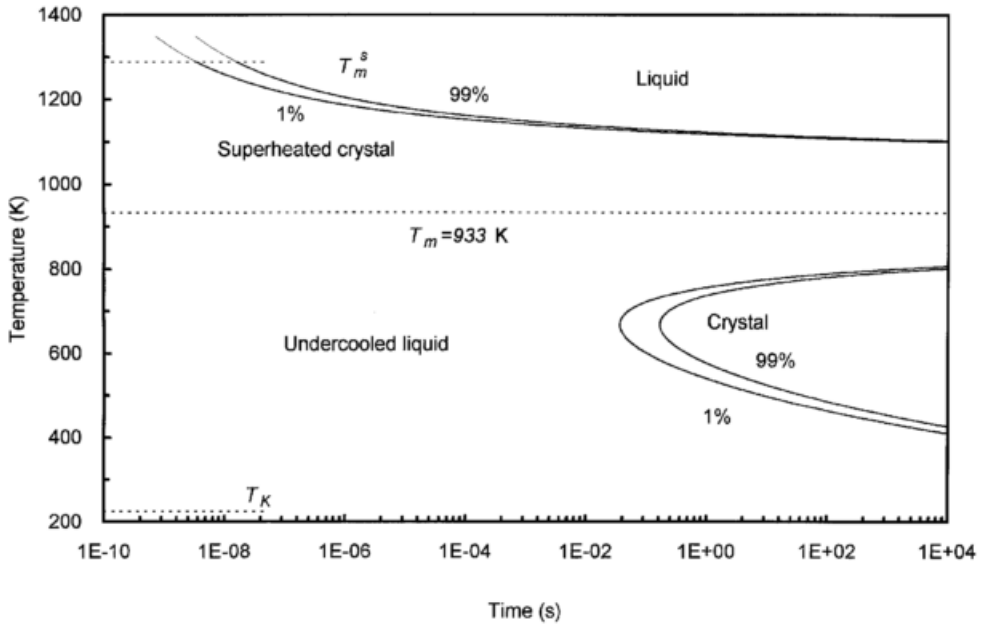

Figure 6.1: Time-temperature-transformation (TTT) curves for melting of a superheated aluminum crystal and for solidification of undercooled liquid aluminum. The volume fractions transformed are indicated by each curve. T_k denotes the lower Kauzmann temperature, and T_s^m the isentropic melting point. Reproduced from [2].

experimental results to computational and theoretical predictions, it is necessary to first estimate the nucleation rates encountered in the set of experiments where melting was observed to initiate at and/or near the bottom Si-SiO_2 interface.

6.2 Extraction of Nucleation Rates from Experimental Data

We estimated the nucleation rate based on analysis of the *in situ* TR signals (presented in Chapter 4). From the TR signals, it is possible to roughly estimate the fraction of the solid that had transformed into liquid as a function of time. (As will be argued later, a rough estimate of the fraction transformed as a function of time, $f(t)$, still leads to reasonably accurate results since the estimates of the nucleation rates here are order-of-magnitude estimates and are not extremely dependent on $f(t)$.) Based on geometric considerations, it is clear that the fraction transformed must be at least a function of the nucleation rate and growth rate of the new phase.

The Johnson-Mehl-Avrami-Kolmogorov (JMAK) [70–74] model describes the kinetics of concurrent nucleation and growth of a new phase in a material. It describes the fraction of the material that has been transformed into the new phase as a function of the nucleation rate, interface velocity, and time. Since the interface velocity can be extrapolated based on our thermal analysis and the fraction transformed as a function of time can be approximated based on the TR signals, estimates of the nucleation rate can be made. By examining the assumptions made in the JMAK theory, we discuss the expected errors in our estimates.

6.2.1 Johnson-Mehl-Avrami-Kolmogorov (JMAK) Analysis

The JMAK theory describes the kinetics of concurrent nucleation and growth by assuming statistical homogeneity of the nucleation rate and basic geometrical considerations. It is assumed that nucleation of the new phase may occur anywhere in the parent material (or along an interface in the case of heterogeneous nucleation) with equal and statistically independent probabilities. As nucleation and subsequent growth of the new phase occurs, the number of nucleation sites become

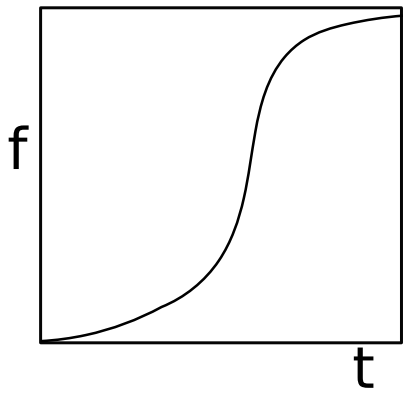

Figure 6.2: Schematic diagram of a typical transformation plot as a function of time. f is the fraction of the parent phase transformed into the new phase as a function of time t.

limited and the transformation process becomes primarily driven by the growth of the new phase. For simplicity, it is assumed that the growth rate of the new phase is isotropic. Additionally, the impingement of interfaces as the transformation proceeds is considered. Consideration of all of the above leads to theoretical predictions of the fraction transformed f as a function of time t, resulting in an s-shaped curve similar to the one shown schematically in Figure 6.2.

Assuming statistical independence of individual nucleation events, the fraction transformed can then be described using poisson statistics [70, 75] and can be described in terms of the nucleation rate and the growth rate. The fraction transformed is then

$$f = 1 - \exp\left(-\langle N \rangle_c\right), \tag{6.1}$$

where $\langle N \rangle_c$ is the expected number of nucleation events for a fraction f of the parent material to transform into the new phase. $\langle N \rangle_c$ is then a function of the nucleation rate and the growth rate of the new phase. It should be noted that the growth rate is exponentially dependent on the temperature at the solid-liquid interface and the nucleation rate is even more sensitive to the local temperature in the material. Since, in melting, large amounts of latent heat is absorbed in the phase transition, both the nucleation and growth rates are expected to be time-dependent. In the most general case, local temperature variations due to nucleation events and interface motion can become significant and the transformation kinetics is best described computationally [76, 77]. The

simple analytical expressions of the JMAK theory, on the other hand, enable quick estimates of the nucleation rates from experimental data.

For the two-dimensional case (such as heterogeneous nucleation along a planar interface) $\langle N \rangle_c$, assuming a time-dependent nucleation rate and an isotropic (but time-dependent) growth rate, and ignoring local temperature variations, $\langle N \rangle_c$ is written as [78]

$$\langle N \rangle_c = \pi \int_0^t J\left(t'\right) \left[R\left(t, t'\right)\right]^2 \, dt', \tag{6.2}$$

where J is the nucleation rate and R is the radius of a transformed region, which is given by

$$R\left(t, \tau\right) = \int_\tau^t v\left(t'\right) \, dt', \tag{6.3}$$

where v is the growth rate of the new phase, which can be described using the interface response function. Equation 6.2 requires knowledge of the nucleation rate as well as the growth rate as a function of time, which are unknown parameters in our experiments.

Further approximations can be made to avoid the complications in Equation 6.2 and still provide reasonable estimates of the nucleation rate. By taking $J\left(t\right)$ out of the integral, assuming a constant growth rate, and integrating, we obtain

$$\langle N \rangle_c = \pi J\left(\bar{t}\right) v^2 t^3, \tag{6.4}$$

and noting Equation 6.1 and solving for $J\left(\bar{t}\right)$, we obtain

$$J\left(\bar{t}\right) = \frac{-3 \ln\left(1 - f\right)}{\pi v^2 t^3}. \tag{6.5}$$

In Equation 6.5, $J\left(\bar{t}\right)$ represents an "average" nucleation rate on the open interval $(0, t)$. $J\left(\bar{t}\right)$ corresponds to the nucleation rate at some point in time in the interval $0 < \bar{t} < t$, according to the mean value theorem. Note that this is assuming that an accurate value is chosen for v. In our experiments, the growth rate v in the direction tangential to the bottom Si-SiO_2 interface is unknown. In order to provide a reasonable underestimate, v was chosen to be $v\left(T_k\right)$, where T_k is the kinetic melting temperature estimated in Chapter 5.

It should be noted that although the JMAK analysis here assumes 2-D nucleation and growth, the estimated nucleation rates here are useful even if nucleation was homogeneous. A consideration of the vertical temperature profile of the film immediately before the onset of nucleation leads one to conclude that nucleation must occur either at the interface (via heterogeneous nucleation) or near the interface (via homogeneous nucleation) since the near-substrate region of the film was hottest and the nucleation rate has an extreme temperature dependence. Moreover, nuclei are not expected to form close to one another due to the heat of fusion and resulting cooling that occurs upon nucleation. With these assumptions, nucleation, regardless of whether it was homogeneous or heterogeneous, can be described in terms of a 2-D nucleation rate.

6.2.2 Estimates of the Liquid Nucleation Rates in the Experiments

The nucleation rate estimations were made by analyzing the experimental substrate-side TR signals and using Equation 6.2. By comparing the experimental TR signals and the calculated TR signals (see: Section 3.4.1), it is possible to estimate (1) the onset of melting, and (2) the time at which the interface region is fully molten. The onset of melting is detected when there is a noticeable drop in the reflectance resulting from thin-film interference effects. The interface region is expected to be completely molten at the onset of saturation of the substrate-side TR signals, where the thickness of the liquid layer is estimated to be $20-30\,nm$. The onset of full liquid transformation at or near the bottom Si-SiO_2 interface is expected to occur before the onset of saturation of the substrate-side TR signals. However, neither the time at which full liquid transformation nor the thickness of the liquid layer that corresponds to full liquid transformation can be determined from the experimental data. As such, in order to provide the high estimates of the nucleation rates, we assume that the time at full transformation (i.e., $f \approx 0.99$) to be at the detectable onset of melting from the substrate-side TR signals. For the low estimates of the nucleation rates, we assume that the time at full transformation (i.e., $f \approx 0.99$) to be at the time at which saturation of the substrate-side TR signals.

Since v, the growth rate of liquid, in the direction tangential to the Si-SiO_2 interface cannot be

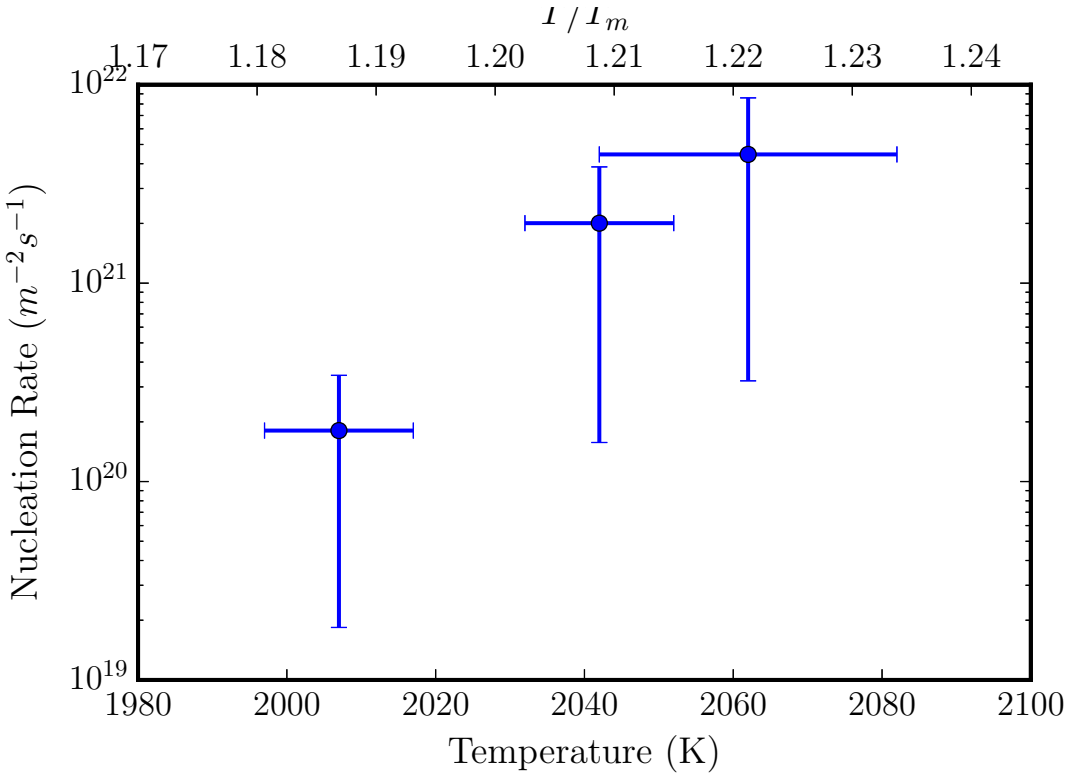

Figure 6.3: Estimated heterogeneous nucleation rates as a function of temperature for the experiments performed at incident energy densities above the substrate-side-melting threshold. These values are underestimates of the actual nucleation rate.

precisely and accurately determined from experiment, in order to provide a definitive underestimate, v was set to the maximum velocity $v\,(T_k)$, where T_k is the estimated kinetic melting temperature (see Chapter 5). This estimate is expected to underestimate the actual liquid nucleation rate. For the high estimate, we assume v to be v at 150 K below the kinetic superheating temperature since this is the temperature reached in the `3DNS` simulation, due to the enthalpy change, after melting is initiated at the bottom interface. The estimated nucleation rates are plotted in Figure 6.3 and tabulated in Table 6.1.

$T\ (K)$	$\pm\epsilon_T\ (K)$	$J\ \left(m^{-2}s^{-1}\right)$	$\pm\epsilon_J\left(m^{-2}s^{-1}\right)$
2010	10	1.8×10^{20}	1.6×10^{20}
2040	10	2.0×10^{21}	1.8×10^{21}
2060	20	4.5×10^{20}	4.1×10^{21}

Table 6.1: Table of the liquid nucleation rates estimated from experimental data. These values are underestimates of the actual nucleation rate.

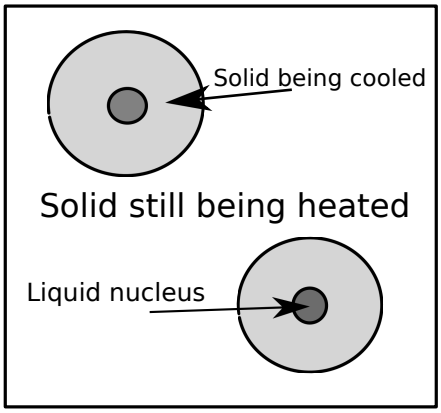

Figure 6.4: Schematic diagram (top view) of nucleated liquid clusters and their respective thermal diffusion radius in a superheated solid matrix. Due to the large heat of fusion and rapid interface movement, it can be approximated that the region within the radius of the thermal diffusion length gets cooled despite the fact that the excimer-laser beam is still incident on the film.

6.3 Discussion and Summary

The geometry of the situation should be considered in order to examine the heat flow situation in the film in more detail. A schematic of the situation is shown in Figure 6.4. Upon nucleation, not only does the nucleated liquid cool down due to decalescence but the area around it, approximately within the radius of the thermal diffusion length, also cools down due to heat conduction. Although the excimer-laser beam was still incident on the film during this entire process, cooling resulting from the enthalpy change upon melting is expected to be much greater than heating due to the

incident excimer-laser beam. Due to the extreme temperature-dependence of the nucleation rate, it can be assumed that, for any given temperature, the nucleation rate in the area of the solid film within the thermal diffusion length is negligible compared to the area of the solid film outside this region being cooled by decalescence.

After considering the scenario above, we argue that the nucleation rates estimated in Section 6.2.2, correspond to the nucleation rates at the very onset of nucleation. The nucleation scenario is expected to be similar to that of "burst nucleation" [79] where the majority of nucleation events occur in a very small timescale. In the situation here, this is due to the extreme temperature-dependence of the nucleation rate and the fact that the solid cools upon nucleation due to the enthalpy change.

In the subsequent chapter, we compare the estimated nucleation rates at the onset of nucleation with those predicted using classical nucleation theory in order to examine whether the theory predicts homogeneous or heterogeneous nucleation under this scenario. Additionally, we examine the significance of non-steady-state nucleation behavior using classical nucleation theory.

Chapter 7

Interpretation of the Experimental Results via Classical Nucleation Theory

In this chapter, we examine the melting situation in our experiments using classical nucleation theory. We utilize classical nucleation theory to examine whether it is predicted that our experimental results correspond to heterogeneous nucleation or homogeneous nucleation. We show that once non-isothermal conditions are accounted for, classical nucleation theory predicts that liquid nucleation, at least based on available parameters, in this case, is heterogeneous.

7.1 Classical Nucleation Theory for Liquid Nucleation in Superheated Solids

It is relevant at this point to discuss the details of classical nucleation theory as it pertains to liquid nucleation in superheated solids. Classical nucleation theory is the most simple and most commonly applied nucleation model and is based on thermodynamics and kinetics principles. Its simplicity and usefulness lie mainly in the fact that the model, which (at least in the simple continuum

description) consists of relatively simple analytic expressions, uses readily available parameters and can describe nucleation under experimental conditions.

Nucleation may be considered as "homogeneous" or "heterogeneous." In homogeneous nucleation, the stochastic formation of a new phase occurs in uniform regions of a system in the absence of catalyzing sites such as crystal defects or impurities, which can aid the nucleation process. On the other hand, in heterogeneous nucleation, the new phase is randomly formed at catalyzing heterogeneities in the material. Under most conditions, it is extremely challenging to induce homogeneous nucleation of the liquid phase in a solid due to material defects that enable copious heterogeneous nucleation at much lower relative superheatings. Hence the upper superheating limits predicted by classical homogeneous nucleation theory are not observed under most conditions [12], even in well-controlled experiments. However, homogeneous nucleation can still be more kinetically favorable under certain conditions (especially if θ is large) since heterogeneous nucleation requires a catalyzing interface whereas homogeneous nucleation occurs volumetrically in the bulk of the material. Moreover, due to the large superheating observed in the present experiments, the possibility of homogeneous nucleation needs to be carefully considered.

Homogeneous nucleation in the classical theory represents the simplest case of nucleation. In an ideal crystal without free surfaces or material interfaces, thermal melting is expected to only occur via homogeneous nucleation of the liquid phase. Heterogeneous nucleation, on the other hand, can occur if there is a defect in the material (such as the Si-SiO_2 interface in the present experiments) where melting may initiate. In both cases, as the solid is heated above the thermodynamic melting point, the liquid phase becomes increasingly more thermodynamically stable. However, there exists a kinetic barrier for melting to occur internally in a homogeneous solid. Due to this "nucleation barrier", a certain degree of superheating is required for the formation of liquid nuclei. In this section, we first describe classical nucleation theory as it applies to melting in superheated solids using its simple continuum formulation under steady-state conditions, with a few modifications [66] in order to more thoroughly describe the situation encountered in our experiments.

Nucleation in condensed systems is most often described using classical nucleation theory in its

simple continuum description. A brief description is provided in Section 2.3.1. Here, we provide a more detailed description of the classical nucleation model in its simple continuum description.

Let us consider the formation of a liquid "nucleus" in its parent solid phase. The change in the free energy resulting from the formation of a liquid nucleus in a solid is given by

$$\Delta G = (\Delta G_{ls} + \Delta E_{st})\, V + \sigma_{sl} A, \tag{7.1}$$

where ΔG_{ls} is the volumetric Gibbs free energy resulting from the solid-to-liquid phase transition, ΔE_{st} is the strain energy density resulting from creating a liquid nucleus in the solid, V is the volume of the nucleus, σ_{sl} is the per-area free energy of the solid-liquid interface, and A is the area of the newly formed solid-liquid interface.

In contrast to solid nucleation in a liquid, the strain energy resulting from the formation of a liquid nucleus in a solid can be significant. In solid nucleation in an undercooled liquid, the surrounding liquid atoms readily and easily conform to the density change, resulting in a negligible amount of strain energy. On the other hand, in nucleation of liquid in a superheated solid, the surrounding solid matrix is more rigid and experiences significant stress due to the density difference between the solid and liquid phases. Based on the analysis by Eshelby [80–82], the strain energy, assuming isotropy, can be written as

$$\Delta G_{st} = \frac{2\mu_s K_l}{3K_l + 4\mu_s} \left(\frac{V_l - V_s}{V_l} \right)^2, \tag{7.2}$$

where μ_s is the shear modulus of the solid phase, K_l is the bulk modulus of the liquid phase, V_l is the specific volume of the liquid phase, V_s is the specific volume of the solid phase. The strain energy acts as an additional thermodynamic barrier to nucleation, effectively increasing the melting point to

$$T_{mp} = T_0 \left(1 + \frac{\Delta E_{st}}{\Delta H_f} \right), \tag{7.3}$$

where T_0 is the equilibrium melting point, ΔE_{st} is the strain energy, and ΔH_f is the enthalpy of fusion. In other words, T_{mp} in Equation 7.3 is the temperature at and above which the liquid nucleation rate is a finite positive value. Since ΔE_{st} is proportional to $\left(\frac{V_l - V_s}{V_l} \right)^2$, T_{mp} is always above the equilibrium melting point, irrespective of whether $V_l > V_s$ or $V_l < V_s$.

Another factor that should be accounted for when describing liquid nucleation is the curvature of the solid-liquid interface [66, 83]. Due to the small size of the liquid nucleus, effects of the solid-liquid interfacial curvature may become significant. This effective interface free energy can be described by the Tolman Equation [83]:

$$\sigma = \sigma_0 \left(1 - 2\alpha\kappa\right), \tag{7.4}$$

where σ_0 is the normal solid-interface energy (σ_{sl}) of the flat interface, α is a material-specific constant called the Tolman coefficient, and κ is the mean curvature of the interface.

Since nucleation is defined as the rate of formation of supercritical clusters, it is helpful to define a term called the critical radius. The critical radius is the radius of a cluster that satisfies the relation

$$\left.\frac{d\Delta G}{dr}\right|_{r^*} = 0, \tag{7.5}$$

where ΔG is given by Equation 7.1. Assuming spherical nuclei, accounting for both the strain energy and the interface curvature of the nucleus, and letting $\Delta G_{ls} = \Delta T \Delta H_f / T_m$ the critical radius can be written as [66]

$$r^* = \frac{2\sigma_0 \pm \sqrt{4\sigma_0^2 - 8(\Delta G_{ls} + \Delta E_{st})\sigma_0\alpha}}{2(\Delta G_{ls} + \Delta E_{st})} \tag{7.6}$$

and the critical energy

$$\Delta G^* = \frac{16\pi\sigma_0^3 f}{\left(|\Delta G_{sl}| - \Delta E_{st}\right)^2} - E_c, \tag{7.7}$$

where $E_c = 4\pi/3(2\alpha)^3(\Delta G_{ls} + \Delta E_{st})$ is a correction term that requires the critical radius to be at least 2α, and $f = 1/3(1 - 4\alpha/r^*)(1 - \alpha/r^*)^2$. A schematic plot of the $\Delta G\,(r)$ is shown in Figure 7.1. Note that $\frac{d\Delta G}{dr} < 0$ for all $r > r^*$, implying that clusters exceeding the critical radius are thermodynamically favored to grow. On the other hand, clusters with radii less than r^* are thermodynamically favored to shrink. In order for nucleation to occur, an energy barrier of ΔG^* must be overcome. Given the above considerations, the nucleation rate can then be expressed as [84]

$$I = N\frac{kT}{h}\left(\frac{2\Omega}{9\pi}\right)^{1/3}\sqrt{\frac{\sigma_{ls}}{kT}}\exp\left(-\frac{\Delta G^*\,(T) + Q}{kT}\right), \tag{7.8}$$

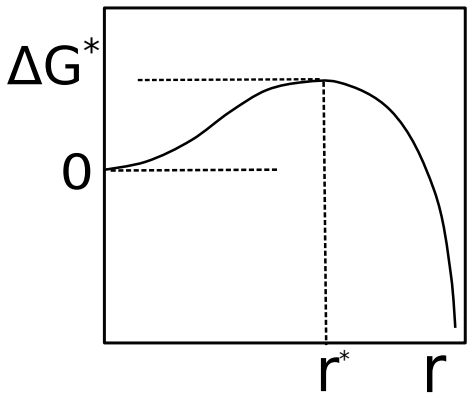

Figure 7.1: Schematic plot of $\Delta G(r)$. ΔG^* is the critical energy for formation of a cluster with a critical radius of r^*. Note that $d\Delta G/dr < 0$ for all $r > r^*$, implying that clusters exceeding the critical radius are thermodynamically favored to grow.

where N is the atomic density of the solid, Q is the activation energy required for diffusion of the solid atoms, ΔG^* is given by Equation 7.7, kT/h is the jump frequency of the solid atoms, and Ω is the atomic volume. The fourth and fifth terms in Equation 7.8 are commonly referred to the Zeldovich factor, which contains information of the shape of the potential barrier, and accounts for the shrinkage of clusters.

In the case of heterogeneous nucleation of a liquid spherical cap at a flat interface, Equation 7.8 may simply be rewritten as [84]

$$I = N^{2/3}\frac{kT}{h}\frac{f(\theta)}{\sqrt{s(\theta)}}\left(\frac{2\Omega}{9\pi}\right)^{1/3}\sqrt{\frac{\sigma_{ls}}{kT}}\exp\left(-\frac{s(\theta)\,\Delta G^*(T)+Q}{kT}\right), \tag{7.9}$$

where θ is the contact angle of the spherical cap,

$$s(\theta) = (2+\cos\theta)(1-\cos\theta)^2/4, \tag{7.10}$$

and

$$f(\theta) = (1-\cos\theta)/2. \tag{7.11}$$

Since $s(\theta) < 1$, the barrier for heterogeneous nucleation is reduced with respect to that of homogeneous nucleation. It can also be seen that, the smaller the contact angle θ, the smaller the

nucleation barrier becomes. This is consistent with with the fact that since r^* is the same for both homogeneous nucleation and heterogeneous nucleation, the critical cluster size for a spherical cap with a smaller contact angle must be smaller. Since a smaller cluster size has a lower work of formation, the energy barrier for the creation of such a cluster is also smaller. Thus, clusters that form a lower contact angle θ with the catalyzing interface can nucleate much more easily.

7.2 Classical Nucleation Theory Calculations

Here, we compare the nucleation rates estimated from experiments (Section 6.2.2) to those predicted by our classical nucleation theory calculations. It should be noted that the computed theoretical nucleation rates here are only applicable to the system at the onset of nucleation. As discussed in Chapter 6, once nucleation initiates, the heat of fusion resulting from melting significantly complicates the heat-flow scenario in the film, abruptly leading to an extreme decrease of the nucleation rate in the film. Thus the nucleation rates estimated from experimental data correspond roughly to the onset of liquid nucleation and can be compared with the computed theoretical nucleation rates.

Our aims here are the following:

1. Examine whether classical nucleation theory predicts that the current situation corresponds to homogeneous or heterogeneous nucleation.

2. Using the estimated nucleation rates from Chapter 6, compare the kinetic superheating predicted by classical nucleation to the predictions in [43, 66, 67].

7.2.1 Assumptions in the Calculations

In order to evaluate whether it is valid to describe liquid nucleation under the high heating rates here using the steady-state form of classical nucleation theory, we begin our analysis by examining the predictions of the simple steady-state approximation. The model is based on a modified

classical nucleation theory described in [35], where the strain energy [36] and the size of the nucleus [35,83] contribute to the energy barrier for nucleation. Details are described in Section 7.1 and the references within. Here, we computed the nucleation rates for both heterogeneous nucleation and homogeneous nucleation and examined whether heterogeneous or homogeneous nucleation is predicted from this formulation of classical nucleation theory.

Due to the extreme temperature dependence of the nucleation rate, when computing the homogeneous nucleation rate, it is necessary to consider the non-isothermal temperature profile in the material at the onset of melting. Based on the TR analysis, at these superheating values, surface-initiated melting occurred near simultaneously with substrate-side-initiated melting. Thus it can be approximated that at the onset of liquid nucleation, the surface temperature was approximately equal to the equilibrium melting point and that temperature of the silicon along the substrate was equivalent to the superheated temperatures required to trigger melting as estimated in Chapter 5. Moreover, in order to compare the various theoretical nucleation rates, the projected homogeneous nucleation rate (in units of frequency per area) should be used (as opposed to the volumetric homogeneous nucleation frequency) to match the units of the heterogeneous nucleation rates. Due to the large temperature gradient in the film and the nucleation rate's extreme dependence on temperature, homogeneous nucleation, if possible in this scenario, is predicted to predominantly occur near the bottom interface. Thus, homogeneous nucleation can be viewed as nearly two dimensional. By taking all of the above into consideration, the projected non-isothermal homogeneous nucleation rate can be written as

$$I_{hom,proj} = \int_0^d I_{hom}\left(T\right)\, dx, \tag{7.12}$$

and the temperature profile in the film, using a linear approximation, can be written as

$$T\left(x\right) = \frac{T_{bot} - T_m}{d} x + T_m, \tag{7.13}$$

where I_{hom} is given by Equation 7.9, d is the film thickness, T_m is the equilibrium melting point, T_{bot} is the temperature of the silicon along the bottom Si-SiO_2 interface, and $dx = \frac{d}{T_{bot}-T_m}\, dT$. Temperature-dependent thermodynamic data from [66] were used in the present calculation. The

Parameter	Value	Reference
ΔH	$4.17 \times 10^9\ J/m^3$	[60]
Q	$4\ eV$	[85, 86]
σ_{sl}	$0.35\ J/cm^2$	[66]
α	$0.145\ nm$	[66]
μ_s	$51.42 - 3.47 \times 10^{-3}T$ GPa	[66]
K_l	$4.53 + 7.54 \times 10^{-3}$ GPa	[66]

Table 7.1: Table of values used in the nucleation calculations.

values used in the calculations are tabulated in Table 7.1.

7.2.2 Results

The heterogeneous nucleation rate, calculated for contact angles of 60° and 85°, are shown in Figure 7.2. These two contact angles correspond to the range of contact angles that are predicted, assuming steady-state heterogeneous nucleation only, based on the nucleation rates estimated from experiments. The calculated projected nucleation rate for homogeneous nucleation, assuming a linear temperature gradient of $350\,K$ (based on our thermal analysis in Chapter 5), is shown in Figure 7.2. The predicted homogeneous nucleation rate, even with such a temperature gradient, is much less than that predicted by heterogeneous nucleation. Additionally, the predicted homogeneous nucleation rate, assuming isothermal conditions, is also plotted in Figure 7.2. Here, two of the experimental data points lie within range of predicted nucleation rates based on the homogeneous nucleation model that assumes isothermal conditions in the film. This clearly demonstrates the importance of the temperature profile in the film when considering homogeneous nucleation. When the temperature gradient is considered, the experimental points lie mostly outside the region in which homogeneous nucleation can be expected. Moreover, the calculated heterogeneous nucleation rates show a better fit to the experimental data points as a function of temperature than the

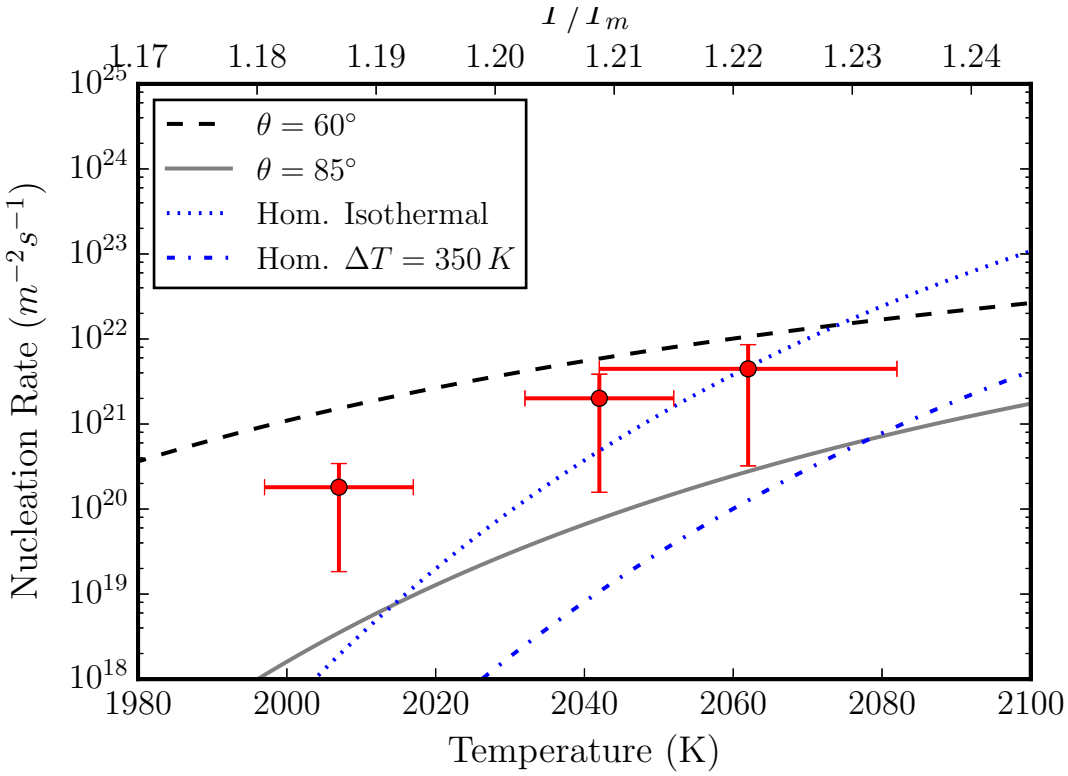

Figure 7.2: Experimental nucleation rates (estimated from TR signals as per Section 6.2) compared with nucleation rates predicted using classical nucleation theory assuming steady-state nucleation in three separate cases: heterogeneous nucleation with a contact angle of 60° and 85°, homogeneous nucleation assuming isothermal conditions and a vertical linear temperature gradient of 350 K in the film. The homogeneous nucleation rate is projected onto a per-area nucleation rate for comparison.

calculated homogeneous nucleation rates.

7.3 Discussion

In melt-mediated processing of silicon films, it is well known that the Si-SiO_2 interface is relatively resistant to initiating melting, at least when compared to grain boundaries and free surfaces. However, though many models of melting in melt-mediated processing of silicon films make the assumption of a melt-resistant Si-SiO_2 interface, until this thesis, there has been no experimental investigations on exactly how melt-resistant the Si-SiO_2 interface is under pulsed-laser melting. Experimental difficulties lie in the challenges of obtaining defect-free, single-crystal silicon with an atomically flat Si-SiO_2 interface, as grain boundaries and interfacial roughness may affect the melting process. In general, melting in superheated solids, particularly at buried interfaces, remains an active area of research since it remains quite challenging to perform such experiments. Unfortunately, due to the experimental difficulties involved in producing such extreme conditions, most investigations pertaining to melting at buried interfaces have been purely computational. Here, we used a material enabled by years of research and development in semiconductor manufacturing technology – the capability to produce practically defect-free, single-crystal silicon on quartz via wafer-bonding techniques – to perform the ideal experiment pertaining to melting in a superheated elemental solid.

By inducing internal heating in single-crystal silicon via substrate-side laser-induced heating through the transparent substrate, we have demonstrated that the bottom Si-SiO_2 interface can undergo a substantial degree of superheating before the onset of melting. By solving the time-dependent heat equation computationally using time- and temperature-dependent parameters, we have shown that melting did not initiate at or near the bottom interface until at least 1.18 T_m and higher at higher incident energy densities (which correspond to higher heating rates). As discussed in Section 6.1, based on the analysis by Lu and Li [2], the heating rates in our present experiments (10^{10} K/s) correspond to a regime where liquid nucleation is expected. A quick comparison to the

homogeneous melting limit for this heating rate proposed by Luo et al. [43] suggests that our observations may indicate homogeneous nucleation. However, several molecular dynamics studies [66,67] point to a much higher kinetic superheating in silicon at similar heating rates, assuming that melting initiates via homogeneous nucleation of liquid. Additionally, interpretation of our experimental data using classical nucleation theory suggests that our experimental result corresponds to one where heterogeneous nucleation along the Si-SiO_2 interface is to be expected – which contradicts the predictions by Luo et al. [43].

Based on the extremely low dislocation density (10^{-2} cm^2) and comparatively high degree of superheating, we conclude that degree of superheating resulted predominantly from the intrinsic heterogeneous nucleation mechanism involving the interface between single-crystal silicon and SiO_2. For a single-crystal silicon film in contact with SiO_2 containing extended defects, such as dislocations, we expect the superheating to decrease commensurately.

7.3.1 On the Thermal Stability of the Si-SiO_2 Interface

It is expected that the (100)-oriented Si-SiO_2 interface is the Si-SiO_2 interface that enables the greatest degree of superheating. This is because the (100)-oriented Si-SiO_2 is predicted to be the Si-SiO_2 interface with the lowest excess free energy [1, 48, 50, 87, 88]. This is due to the fact that the contact angle, θ can be described by the corresponding interface energies as

$$\cos\theta = \frac{\sigma_{s\text{-}SiO_2} - \sigma_{l\text{-}SiO_2}}{\sigma_{s\text{-}l\text{-}Si}}, \tag{7.14}$$

where $\sigma_{s\text{-}SiO_2}$ is the interface energy between crystal silicon and SiO_2, $\sigma_{l\text{-}SiO_2}$ is the interface energy between liquid silicon and SiO_2, and $\sigma_{s\text{-}l}$ is the interface energy between crystal silicon and liquid silicon. The corresponding force balance for Equation 7.14 is shown schematically in Figure 7.3. Since the contact angle, θ must be between 0° and 180°, where $\cos\theta$ has a negative slope, a decrease in $\sigma_{s\text{-}SiO_2}$ leads to an increase in θ. A larger contact angle results in a larger free energy barrier (ΔG^*) for nucleation. As such, the (100)-oriented Si-SiO_2 interface, the interface where σ is expected to be lowest [50] and θ is highest, is expected to be the Si-SiO_2 interface that

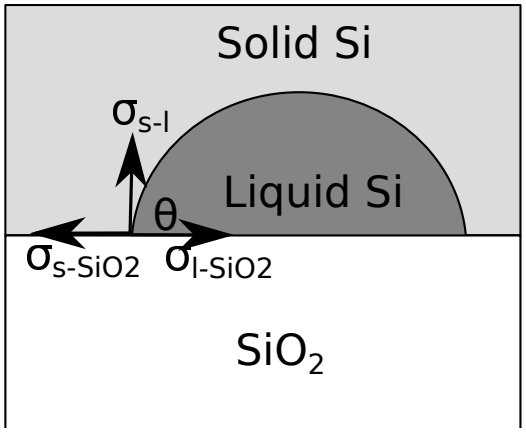

Figure 7.3: Schematic diagram of the corresponding interfacial energies and the force balance describing the contact angle given by Equation 7.14.

enables the maximum degree of superheating.

Although the present work addresses the (100)-oriented Si-SiO_2 interface, we point out that, based on theoretical considerations and other experimental reports, it should not be surprising if Si-SiO_2 interfaces of other crystal orientations can also be superheated. In CW-laser-induced melting experiments [1,48,88], it was shown melting initiated preferentially at grain boundaries rather than at oxide interfaces in oxide-capped polycrystalline silicon films on SiO_2. Previously, Atwater el al. [50] experimentally estimated the energy anisotropy between the highest ((111)-oriented) and lowest ((100)-oriented) Si-SiO_2 interface to be only about 0.069 J/m^2. In another work by Xu et al. [31], nanocrystals of germanium, another elemental semiconductor, of various crystallographic orientations embedded in a silica matrix were found to melt at temperatures significantly above the equilibrium melting point. Xu et al. also demonstrated that heterogeneous nucleation along various oxide interfaces, based on a classical nucleation model, accurately modeled the observed superheating. Thus, it should not be surprising if Si-SiO_2 interfaces of other orientations can be superheated.

7.4 Summary

Based on theoretical considerations, we suggest that the mechanism of melting in the superheated solid corresponds to that of liquid nucleation. From the thermal analysis in Chapter 5, the heating rate was approximately $10^{10}\,K/s$, a couple orders of magnitude below the heating rate typically expected before non-thermal melting mechanisms are expected to occur. It was found that both results predict that heterogeneous nucleation of liquid silicon along the Si-SiO_2 interface is the most probable nucleation mechanism of melting in the superheated silicon films on SiO_2. In addition to contributing fundamentally, this work clearly demonstrates that the melt-resistant nature of such low-excess-free-energy interfaces can profoundly affect how melting initiates and transpires in the solid during melt-mediated laser processing of silicon films.

Chapter 8

Conclusions

8.1 Summary

Melting in polycrystalline silicon films in contact with SiO_2 is a critical step in several important laser processes, such as excimer laser annealing (ELA), mixed-phase-solidification (MPS), and laser planarization of polycrystalline silicon films. Though many studies have focused on understanding melting of amorphous silicon and solidification of liquid silicon from the melt, not much has been done to further our understanding of how melting transpires in these polycrystalline films, often with complex microstructures. In order to characterize melting in polycrystalline films in contact with SiO_2, it is necessary to investigate how melting initiates from defects such as Si-SiO_2 interfaces and grain boundaries.

Here, we investigated melting along the (100)-oriented Si-SiO_2 interface by utilizing single-crystal silicon thin films on quartz substrates. In order to examine how the Si-SiO_2 interface initiates melting, internal melting was induced along the bottom Si-SiO_2 interface. It was found that melting was triggered along the Si-SiO_2 interface only at temperatures well above the equilibrium melting point, at around 350 K above the melting point.

We recognize that this is an unusual opportunity to perform a fundamental investigation of melting in a superheated solid. The sizable degree of kinetic superheating was enabled by the

fact the undoped semiconductor-grade silicon was essentially a perfect crystal with a planar, low-excess-free-energy Si-SiO_2 interface – a practically ideal material for an investigation of melting in a superheated solid. Based upon this and theoretical considerations, we concluded that melting can be explained via nucleation of liquid either homogeneously in the bulk solid or heterogeneously along the Si-SiO_2 interface.

We examined whether classical nucleation theory would predict that the nucleation mechanism was heterogeneous or homogeneous. By fitting our experimental data to classical nucleation theory using available material parameters, we showed that classical nucleation theory predicts that the situation corresponds to one where heterogeneous nucleation of the liquid phase is to be expected. The results from our analysis is consistent with computational results that suggest that homogeneous nucleation would require a higher degree of superheating.

8.2 Suggestions for Future Work

Melting at various defective sites is a topic that is both of interest fundamentally and technologically. Future work may include investigations of initiating melting at Si-SiO_2 interfaces of other orientations and at specific types of grain boundaries. Theoretically, it has been proposed that certain low-angle grain boundaries may be superheated above the equilibrium melting point [28, 29]. However, there has yet been any reported experimental confirmations of these theoretical models.

The results here also open the door for computational studies of liquid nucleation in superheated films during pulsed-laser irradiation. In order to better capture nucleation and growth of liquid in the superheated solid during excimer-laser irradiation, one must consider the three-dimensional nature of both the transient heat-flow and phase transformations that transpire in the film. An extension of the computational model (by introducing transient and athermal liquid nucleation) to three dimensions may refine the quantitative results presented in this dissertation. The simulations, when combined with more experimental studies, may enable one to more thoroughly and more quantitatively examine the mechanism of liquid nucleation.

The results of this research may also be used to conduct more applied work. Since Si-SiO_2 interfaces are unfavorable sites for initiating melting but grain boundaries can readily initiate melting, one might ask: Given sufficiently thin, oxide-capped silicon films, can MPS-like microstructures (large-grain (100)-surface-textured films) be produced under excimer-laser irradiation? The development of efficient excimer-laser-based processes to produce MPS-like microstructure would be a significant contribution since excimer-laser-based processes are compatible with high-temperature-intolerant substrates [4] whereas MPS is not [1]. Although it has been shown that (100)-surface-textured silicon films (where $> 96\%$ of the grains are oriented within 10° of the (100) surface normal) can be produced using excimer-laser irradiation [89], there are conflicting explanations for the surface texturing [10, 89]. Moreover, these laser crystallization processes involve hundreds of pulses per area, and are thus too resource-intensive for large-scale manufacturing. The development of a more efficient process to produce MPS-like material on economical glass substrates rather than on expensive quartz substrates could lead to applications in thin-film-transistor technology and photovoltaic technology. Additionally, since excimer-laser processes are already used in manufacturing, such a process would also be compatible with existing manufacturing capabilities. From a scientific perspective, such a process would also be quite interesting since it may reveal much about the thermodynamics and kinetics of the system.

Bibliography

[1] M. Chahal, *Mixed-Phase Solidification of Thin Silicon Films on Silicon Dioxide*, PhD thesis, Columbia University, 2010.

[2] K. Lu and Y. Li, Phys. Rev. Lett. **80**, 4474 (1998).

[3] F. S. d'Aragona, Journal of the Electrochemical Society **119**, 948 (1972).

[4] T. Sameshima, S. Usui, and M. Sekiya, IEEE Electron Device Lett. **7**, 276 (1986).

[5] R. S. Sposili and J. S. Im, Appl. Phys. Lett. **69**, 2864 (1996).

[6] T. Noguchi, Japn. J. Appl. Phys. **32**, L1584 (1993).

[7] N. Yamauchi and R. Reif, J. Appl. Phys. **75**, 3235 (1994).

[8] H. Kuriyama *et al.*, Jpn. J. Appl. Phys. **33**, 5657 (1994).

[9] H. J. Kim and J. S. Im, MRS Proc. **321**, 665 (1994).

[10] M. He, R. Ishihara, W. Metselaar, and K. Beenakker, J. Appl. Phys. **100**, 083103 (2006).

[11] Q. Mei and K. Lu, Prog. Mat. Sci. **52**, 1175 (2007).

[12] K. F. Kelton and A. L. Greer, *Nucleation in Condensed Matter*, 1st ed. (Pergamon Press, 2010).

[13] D. H. Auston, C. M. Surko, T. N. C. Venkatesan, R. E. Slusher, and J. A. Golovchenko, Appl. Phys. Lett. **33**, 437 (1978).

[14] J. P. Leonard, *Nucleation rate measurement in the $Si - SiO_2$ thin film system*, PhD thesis, Columbia University, 2000.

[15] D. R. Gaskell, *Introduction to the Thermodynamics of Materials*, 5th ed. (Taylor & Francis Group, LLC, 2008).

[16] G. Jaeger, Arch. Hist. Ex. Sci. **53**, 51 (1998).

[17] H. A. Wilson, Philos. Mag. **50**, 238 (1900).

[18] E. Rie, *über die Einfluss der Oberflächenspannung auf Schmelzen und Gefrieren*, PhD thesis, University of Vienna, 1920.

[19] F. Meissner, Z. Anorg. Allg. Chem. **110** (1920).

[20] J. W. M. Frenken and J. F. van der Veen, Phys. Rev. Lett. **54**, 135 (1985).

[21] J. F. van der Veen, Surf. Sci. **433-435**, 1 (1999).

[22] J. W. Herman and H. E. Elsayed-Ali, Phys. Rev. Lett. **69**, 1228 (1992).

[23] T. E. Hsieh and R. W. Balluffi, Acta Metall. **37**, 1637 (1998).

[24] J. Q. Broughton and G. H. Gilmer, Phys. Rev. Lett. **56**, 2692 (1986).

[25] S. R. Phillpot, J. F. Lutsko, D. Wolf, and S. Yip, Phys. Rev. B **40**, 2832 (1989).

[26] S. R. Phillpot and D. Wolf, J. Am. Ceram. Soc. **73**, 933 (1990).

[27] M. Tang, W. C. Carter, and R. M. Cannon, Phys. Rev. Lett. **97**, 075502 (2006).

[28] W. Fan and X.-G. Gong, Phys. Rev. B **72**, 064121 (2005).

[29] T. Frolov and Y. Mishin, Phys. Rev. Lett. **106**, 155702 (2011).

[30] Q. S. Mei, Z. H. Jin, and K. Lu, Philos. Mag. Lett. **85**, 203 (2005).

[31] Q. Xu *et al.*, Phys. Rev. Lett. **97**, 155701 (2005).

[32] W. Kauzmann, Chem. Rev. **43**, 219256 (1948).

[33] H. J. Fecht and W. L. Johnson, Nature **334**, 50 (1988).

[34] J. L. Tallon, Nature **342**, 658 (1989).

[35] X.-M. Bai and M. Li, Phys. Rev. B **72**, 052108 (2005).

[36] D. R. Uhlmann, J. Non-Cryst. Mat. **41**, 347 (1980).

[37] C. J. Rossouw and S. E. Donnelly, Phys. Rev. Lett. **55**, 2960 (1985).

[38] J. Dges, H. Gleiter, and J. H. Perepezko, MRS Proceedings **57**, 67 (1985).

[39] L. Gråbaek *et al.*, Phys. Rev. Lett. **64**, 934 (1990).

[40] Q. Mei, S. Wang, H. Cong, Z. Jin, and K. Lu, Acta Mater. **53**, 1059 (2005).

[41] L. Zhang, L. H. Zhang, M. L. Sui, J. Tan, and K. Lu, Acta Mater. **54**, 3553 (2006).

[42] D. A. Boness and J. M. Brown, Phys. Rev. Lett. **71**, 2931 (1993).

[43] S.-N. Luo *et al.*, Phys. Rev. B **68**, 134206 (2003).

[44] N. Fabricius, P. Hermes, D. von der Linde, A. Pospieszczyk, and B. Stritzker, Solid State Communications **58**, 239 (1986).

[45] E. A. Murphy, H. E. Elsayed-Ali, and J. W. Herman, Phys. Rev. B **48**, 4921 (1993).

[46] J. S. Im, H. J. Kim, and M. O. Thompson, Appl. Phys. Lett. **63**, 1969 (1993).

[47] T. Voutas, A. Marmorstein, and R. Solanki, Proc. SPIE Conf. **3014**, 112 (1997).

[48] M. Chahal *et al.*, **1426**, 257 (2012).

[49] J. B. Lasky, Appl. Phys. Lett. **48** (1986).

[50] H. Atwater, C. Thompson, and H. Smith, J. Mat. Res. **3**, 1232 (1998).

[51] A. Savitzky and M. J. E. Golay, Anal. Chem. **36**, 1627 (1964).

[52] H. A. MacCleod, *Thin-Film Optical Filters*, 4th ed. (CRC press, 2010).

[53] G. E. Jellison and F. A. Modine, J. Appl. Phys. **76**, 3758 (1994).

[54] G. E. Jellison and D. H. Lowndes, Appl. Phys. Lett. **51**, 352 (1987).

[55] J. H. Wray and J. T. Neu, J. Opt. Soc. Am. **59**, 774 (1967).

[56] P. A. Stolk, A. Polman, and W. C. Sinke, Phys. Rev. B **47**, 5 (1993).

[57] G. L. Pollack, Rev. Mod. Phys. **41**, 48 (1969).

[58] P. Kapitza, J. Phys.(USSR) **4**, 181 (1941).

[59] D. H. Hurley, M. Khafizov, and S. L. Shinde, J. Appl. Phys. **109**, (2011).

[60] P. D. Desai, J. Phys. Chem. Ref. Data **15**, 967 (1986).

[61] K. K. Kelley, High-temperature heat-content, heat-capacity, and entropy data for the elements and inorganic compounds, in *Contributions to the Data on Theoretical Metallurgy*, , XIII No. 584-585, US Govt. Print. Off., 1960.

[62] C. J. Glassbrenner and G. A. Slack, Phys. Rev. **134**, A1058 (1964).

[63] O. Sergeev, A. Shashkov, and A. Umanskii, J. Eng. Phys. **43**, 1375 (1982).

[64] X. Xu, C. P. Grigoropoulos, and R. E. Russo, Appl. Phys. Lett. **65**, 1745 (1994).

[65] J. J. Wang, A. B. Limanov, Y. Wang, and J. S. Im, MRS Proceedings **1770**, 2134184 (2015).

[66] Q. Zhang, Q. Li, and M. Li, J. Chem. Phys. **138**, (2013).

[67] A. M. Nieves and T. Sinno, J. Chem. Phys. **135**, (2011).

[68] S. R. Phillpot, S. Yip, and D. Wolf, Comput. Phys. **3**, 20 (1989).

[69] B. Rethfeld, K. Sokolowski-Tinten, D. von der Linde, and S. I. Anisimov, Phys. Rev. B **65**, 092103 (2002).

[70] A. N. Kolmogorov, Bull. Acad. Sci. USSR, Math. Ser **1**, 355 (1937).

[71] W. Johnson and R. F. Mehl, TAIME **135**, 416 (1939).

[72] M. Avrami, J. Chem. Phys. **7**, 1103 (1939).

[73] M. Avrami, J. Chem. Phys. **8**, 212 (1940).

[74] M. Avrami, J. Chem. Phys. **9**, 177 (1941).

[75] V. Skripov, Cur. Top. Mat. Sci. **2**, 327 (1977).

[76] J. P. Leonard and J. S. Im, MRS Proceedings **580**, 233 (1999).

[77] J. P. Leonard and J. S. Im, Appl. Phys. Lett. **78**, 3454 (2001).

[78] R. W. Balluffi, S. Allen, and W. C. Carter, *Kinetics of materials* (John Wiley & Sons, 2005).

[79] K. Barmak, Order-disorder transformations in metallic films, in *Metallic Films for Electronic, Optical, and Magnetic Applications*, edited by K. Barmak and K. Coffey, chap. 7, pp. 302–352, Woodhead Publishing, 2014.

[80] J. Eshelby, Solid State Physics **3**, 79 (1956).

[81] J. D. Eshelby, Proc. R. Soc. of London: Ser. A **241**, 376 (1957).

[82] F. R. N. Nabarro, Proc. R. Soc. of London, Ser. A **175**, 519 (1940).

[83] R. C. Tolman, J. Chem. Phys. **16**, 758 (1948).

[84] D. T. Wu, Nucleation theory, in *Solid State Physics*, edited by H. Ehrenreich and F. Spaepen, Academic Press, 1996.

[85] M. Tang, L. Colombo, J. Zhu, and T. D. De La Rubia, Phys. Rev. B **55**, 14279 (1997).

[86] H. Bracht, E. E. Haller, and R. Clark-Phelps, Phys. Rev. Lett. **81**, 393 (1998).

[87] J. S. Im *et al.*, J. Cryst. Growth **312**, 2775 (2010).

[88] Y. Wang *et al.*, MRS Proceedings **1770**, 2134674 (2015).

[89] D. P. Gosain *et al.*, Jpn. J. Appl. Phys. **42**, L135 (2003).

[90] J. B. Zeldovich, Acta Physiochimica U.R.S.S. **18**, 1 (1943).

[91] J. I. Frenkel, *Kinetic Theory of Liquids* (Oxford University Press, 1946).

[92] V. V. Gupta, *Analysis and computational modeling of nucleation and solidification in rapidly quenched liquids*, PhD thesis, Columbia University, 1997.

[93] J. S. Im, V. V. Gupta, and M. Crowder, Appl. Phys. Lett **72**, 662 (1998).

[94] J. S. Im, V. V. Gupta, and M. A. Crowder, Unpublished (1997).

[95] M. A. Crowder, *Microstructural development in sequential lateral solidification of thin Si films*, PhD thesis, Columbia University, 2001.

[96] D. T. Wu, J. Chem. Phys. **97** (1992).

[97] D. Ma, Y. Li, and D. Ma, Journal of Physics: Condensed Matter **12**, 9123 (2000).

[98] J. Berry, K. Elder, and M. Grant, Phys. Rev. B **77**, 224114 (2008).

[99] Y. Deng *et al.*, MRS Proceedings **1245**, 1245 (2010).

[100] Y. Deng, *The Mechanism of Solid Nucleation in Excimer-Laser-Quenched Liquid Silicon on Silicon Dioxide*, PhD thesis, Columbia University, 2011.

[101] S. Stiffler, M. O. Thompson, and P. Peercy, Phys. Rev. B **43**, 9851 (1991).

[102] S. Uma, A. McConnell, M. Asheghi, K. Kurabayashi, and K. Goodson, Int. J. Thermophys. **22**, 605 (2001).

[103] G. Harbeke, *Optical properties of polycrystalline silicon films* (Springer, 1985).

[104] P. Keblinski, D. Wolf, S. R. Phillpot, and H. Gleiter, J. Mat. Res. **13**, 2077 (1998).

[105] T. Sameshima and S. Usui, J. Appl. Phys. **74**, 6592 (1993).

[106] J. Narayan and C. White, Appl. Phys. Lett. **44**, 35 (1984).

[107] J. H. Yoon and J. S. Im, Metals and Materials **5**, 525 (1999).

[108] Q. Hu, *Dynamics of melt-mediated crystallization of amorphous silicon films*, PhD thesis, Columbia University, 2011.

[109] J. J. Wang, Y. Wang, A. B. Limanov, A. C. Chitu, and J. S. Im, Unpublished (2015).

Appendix A

On the Relevance Transient and Athermal Nucleation

Due to the high heating rates encountered in our experiments, athermal nucleation and transient nucleation effects may become substantial. In this appendix, we consider the significance of transient (non-steady-state) nucleation behavior. It was found that, using readily available parameters, classical nucleation theory predicts that while the nucleation behavior is predicted to be thermal-mechanism-dominated, a significant fraction of nucleation events is expected to correspond to the athermal mechanism of nucleation (as a consequence of a changing critical cluster size resulting from the high heating rate). Additionally, it is predicted that the nucleation rates should exhibit at least some deviation from purely steady-state nucleation behavior.

A.1 Background

In investigations involving liquid nucleation in a superheated solid, the steady-state form of classical nucleation is typically used to describe the nucleation process [2, 36, 41], even under high heating rates [2, 41] and in systems with slow kinetics [36]. Transient nucleation behavior and athermal nucleation mechanism have never before been considered for liquid nucleation in a superheated

solid. Here we examine whether athermal nucleation (i.e, nucleation resulting from a changing critical cluster size due to fast heating rates) is relevant in our experiments. Additionally, we also examine the degree to which transient (i.e. non-steady-state) nucleation behavior participates under the conditions that are encountered in our experiments using a simple analysis based on the isothermal nucleation induction time.

It is useful at this point to provide a brief background of classical nucleation theory. The total nucleation rate is defined as the rate of change in the supercritical cluster population,

$$J_{total} = \frac{d}{dt}\left(\int_{n^*}^{w} N_{n,t}\, dn\right), \tag{A.1}$$

where t is time, n^* is the critical cluster size, w corresponds to a cluster size that is sufficiently large such that $N_{n\geq w,t} = 0$, and $N_{n,t}$ is the cluster population of a cluster of size n at time t. The cluster distribution can be described using the Zeldovich-Frenkel equation [90, 91],

$$\frac{\partial N_{n,t}}{\partial t} = \frac{\partial}{\partial n}\left\{k^+_{n,t} N^e_n \frac{\partial}{\partial n}\left(\frac{N_{n,t}}{N^e_n}\right)\right\}, \tag{A.2}$$

where $k^+_{n,t}$ is the forward reaction rate of a cluster of size n at time t and N^e_n is the equilibrium cluster population for a cluster of size n. The total nucleation rate can be derived by combining Equations A.1 and A.2,

$$J_{total} = -k^+_{n^*} \left.\frac{\partial N_{n,t}}{\partial n}\right|_{n^*} - N_{n^*}\frac{dn^*}{dt}. \tag{A.3}$$

In Equation A.3, the first term of on the right side of the equation captures "thermal" nucleation rate and second term captures "athermal" nucleation rate. Thermal nucleation occurs when a cluster has fluctuated beyond its critical size. On the other hand, athermal nucleation occurs when the critical cluster size decreases a function of time, where existing clusters become supercritical (leading to a positive athermal nucleation rate); and athermal denucleation occurs when the critical cluster size increases as a function of time, where existing clusters become subcritical (leading to a negative athermal nucleation rate). It should be noted that whenever the system is non-isothermal with respect to time, some degree of athermal (de)nucleation is expected. Due to the high heating rates in our experiments (10^{10} K/s), athermal nucleation should at least be considered.

In order to examine the relative significance of athermal nucleation, we utilize a simple approach based on the nucleation-mechanism diagrams developed in [92,93]. A parameter called β is defined in order to quantify the ratio of thermal nucleation to athermal nucleation:

$$\beta = \frac{J_{thermal}}{J_{athermal}} = -\frac{k^+_{n^*}\xi}{(dn^*/dt)\,(dT/dt)}. \tag{A.4}$$

In the nucleation-mechanism diagram, we plot the upper and lower estimates of "isomechanism" contours (i.e., $\beta = 1$) with dT/dt (the heating rate) on the y-axis and T (temperature) on the x-axis and divide the plot into two regions: a region where the athermal contribution to the total nucleation rate is expected to dominate, and a region where the thermal contribution is expected to dominate.

In addition to considering the significance of athermal nucleation in our experiments, we also examine the extent to which non-steady-state nucleation behavior can be expected to participate under the conditions corresponding to our experiments. In order to examine the effects of transient nucleation behavior, following the procedure in [94, 95], we superimpose $1/\tau$ in the nucleation-mechanism plots. τ is the isothermal induction time at the corresponding temperature on the mechanism diagram, and is given by [96]:

$$\tau = -\frac{3\pi\eta kTn^*}{k^+_{n^*}\Delta G'} \tag{A.5}$$

with

$$\eta = \ln(Zn^*) + 0.3, \tag{A.6}$$

where k is Boltzmann's constant, T is temperature, n^* is the critical cluster size, $k^+_{n^*}$ is the forward reaction rate for a cluster of the critical size, and $\Delta G'$ is the energy of formation for a cluster of the critical size. The isothermal induction time corresponds to the total time required, for a given temperature, to establish near-steady-state populations of clusters near the critical size, starting initially from the condition in which no subcritical clusters are present. Although the situation encountered under the experimental conditions involved in this work is highly non-isothermal, the heating rates along the 1 K/τ curves are meaningful in that they represent the critical heating rates

where the solid spends an amount of time in excess of τ in a one degree interval – a sufficiently small temperature interval wherein the reaction kinetics do not change significantly. Thus the region of the diagram lying below this 1 K/τ curve corresponds to a parameter domain where nucleation can be expected to occur at near-steady-state conditions. On the other hand, heating rates lying at least one or two orders of magnitude above this 1 K/τ curve can be interpreted as heating rates where nucleation is expected to become significantly non-steady-state [95].

A.2 Nucleation-Mechanism-Mode Diagrams

The nucleation-mechanism-mode diagrams for the nucleation of liquid silicon in superheated solid silicon for contact angles of 60° and 85° (which corresponds to the range of contact angles estimated in the steady-state fit in Chapter 7) are shown in Figure A.1a and Figure A.1b, respectively. For a heating rate of 10^{10} K/s and temperatures of above 2000 K, as was estimated from our thermal analysis, the plots in Figure A.1 show that nucleation is expected to thermal-mechanism-dominated, where the athermal nucleation rate is a but a fraction of the thermal nucleation rate. This is perhaps not unexpected since $k_{n^*}^+$ increases with temperature, leading to higher thermal nucleation rates. However, it should be noted that while the situation is expected to lie within the thermal-nucleation-dominated regime, the fact that the situation encountered in the experiments lie relatively close to the lower isomechanism curve suggests that it is likely that a non-negligible fraction of nucleation events were due to the athermal mechanism.

On the other hand, the diagrams in Figure A.1 suggest that nucleation under these conditions is expected to occur in the transient regime. The result calculated using our experimental conditions lie between the 1 K/τ and 10 K/τ curves, suggesting that nucleation in the system deviated from near-steady-state conditions.

According to a numerical study by Im et al. [94], the nucleation rate becomes extremely transient if the situation lies at or above the 100 K/τ curve. The 100 K/τ line, for several materials, lies within the region where the numerically calculated athermal nucleation rate is equal to the thermal

nucleation rate. Moreover, the calculated nucleation rate at 100 K/τ was calculated to be 5% of its corresponding steady-state value.

Since the situation encountered in our experiments lies well below the 100 K/τ curve and less than an order of magnitude above the 1 K/τ curve, we do not expect substantial deviation from near-steady-state nucleation conditions. Moreover, the expression for the steady-state nucleation rate presented in Chapter 7 fits the experimental data reasonably well. In a highly transient situation, the nucleation rate is predicted to increase much more drastically as a function of temperature compared to that under near-steady-conditions, which would result in a poorer fit to the experimental data.

A.3 Discussion and Summary

We suggest that the most notable aspect of this analysis is the possibility that athermal nucleation and highly transient nucleation behavior can be induced in melting experiments. Such possibilities were never before considered in investigations of melting in superheated solids. In practice, one can use a different radiation source (e.g. by manipulating the wavelength and pulse duration) to induce higher heating rates and select a different material with slower melting kinetics to induce a situation where the athermal mechanism and transient behavior is predicted to become significant. Unlike in solidification, where the quench rate is limited by heat conduction away from the undercooled liquid, in melting experiments, the heating rate can be readily manipulated. Thus, experiments involving melting in superheated solids can be a better venue for examining these phenomena.

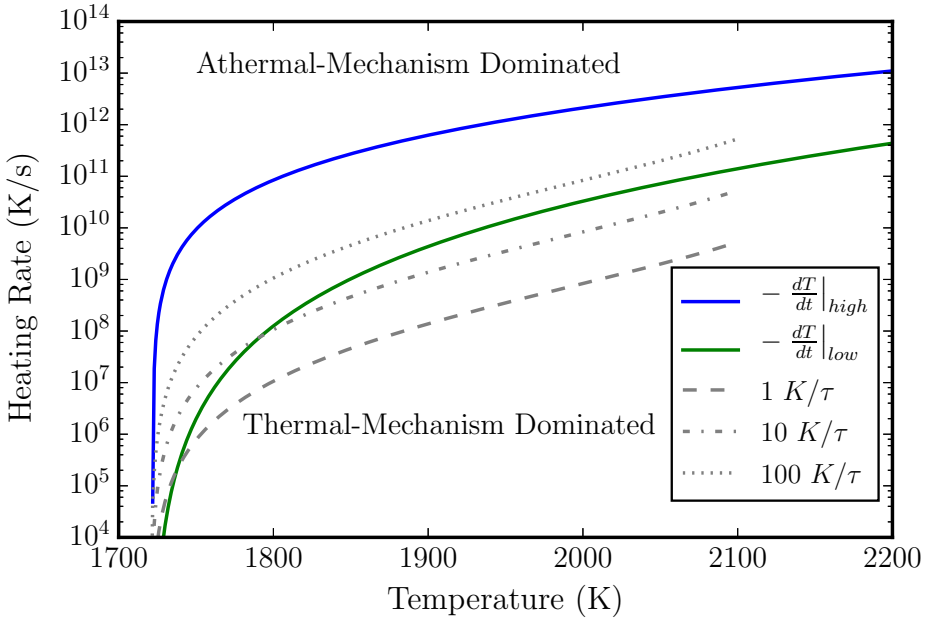

(a) Mechanism-mode diagram for a contact angle of 60°.

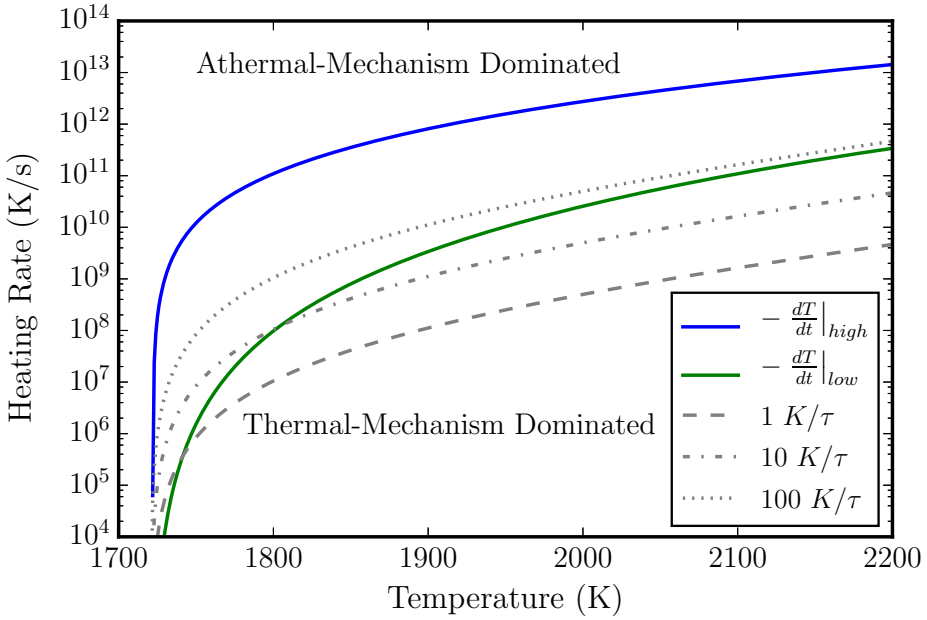

(b) Mechanism-mode diagram for a contact angle of 85°.

Figure A.1: Nucleation-mechanism-mode diagrams for contact angles of 60° and 85°. The blue solid line is the upper estimate of $\beta = 1$; the green solid line is the lower estimate of $\beta = 1$;the dotted gray line corresponds to 100 K/τ; the dotted-dashed gray line corresponds to 10 K/τ; and the dashed gray line corresponds to 1 K/τ.

Appendix B

Superheating and Melting Under Extended-Pulse Excimer-Laser Irradiation

Superheating and melting at the (100)-oriented Si-SiO_2 interface at lower heating rates was investigated via extended-pulse excimer-laser irradiation. The sample and experimental configurations are described in Chapter 4. Whereas the experiments conducted via short-pulse-duration excimer-laser irradiation in Chapter 4 resulted in interfacial superheating in excess of 300 K, the experiments in this chapter, conducted via extended-pulse-duration excimer-laser irradiation, resulted in interfacial superheating values of only approximately 50 K. Various possible explanations for this much-reduced superheating are examined and discussed.

B.1 Introduction and Background

In this dissertation, we presented experimental results that demonstrated superheating of the Si-SiO_2 interface during excimer-laser irradiation. Our thermal analysis estimated the superheating at and near the Si-SiO_2 interface to be 370 ± 35 K before the onset of internal melting, resulting in an

effective kinetic melting temperature of 1.2 T_m. Using classical nucleation theory, our calculations suggest that, in the experiments where internal melting was observed, melting initiated from the Si-SiO_2 interface via the heterogeneous nucleation mechanism. All of the experiments presented thus far involved an incident beam with the short-pulse-duration beam profile. According to JMAK theory [70–74], if the observed superheating resulted from a nucleation barrier to melting, the degree of kinetic superheating should correlate with the heating rate. In this chapter, we present our results for experiments performed under a lower heating rate, by using a extended-pulse incident beam profile.

B.2 Experimental

The experimental setup and sample configurations are presented in Chapter 3. All of the experiments and analysis from the previous chapters were repeated using a extended-pulse-duration beam, with a full-width-at-half maximum (FWHM) of approximately 240 ns. In order to extend the pulse, the initially 30-ns beam was passed through a pulse-duration extender, which consisted of a series of mirrors. A schematic of the excimer-laser system with the pulse-duration extender is shown in Figure B.1.

B.3 Results

In situ TR signals obtained during laser irradiation are presented in this section. We first present the results of the most significant experiment of this work – substrate-side irradiation (i.e., internal heating) experiments performed at various incident energy densities. Due to the fact that the time-dependent intensity profile of the incident excimer-laser beam fluctuated with each set of experiments, the corresponding temporal intensity profile of the excimer-laser pulse is presented with each set of experiments. Additionally, the results of the thermal analysis, using the same procedures developed in Chapter 5 are presented in this section. The results of the surface-side irradiation experiments are presented in the latter part of this section for comparison.

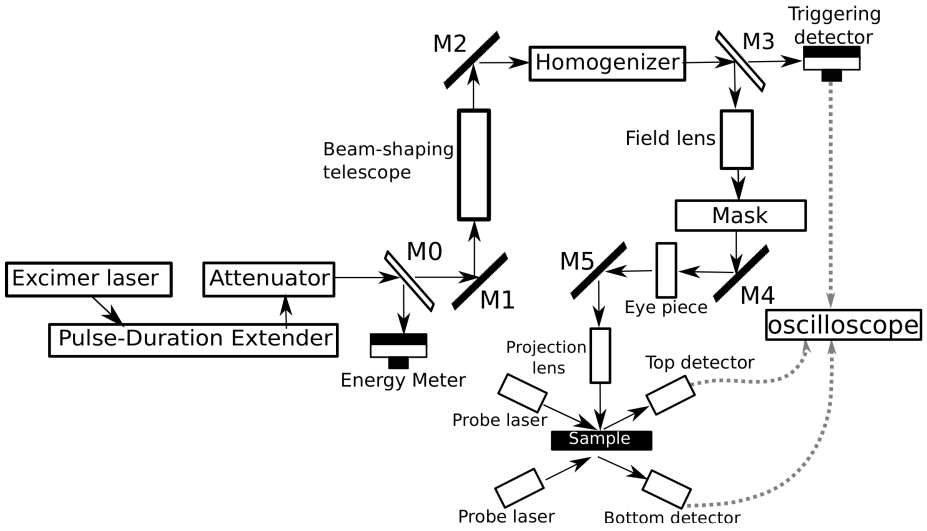

Figure B.1: Schematic of the excimer-laser system used in the extended-pulse-duration experiments.

B.3.1 Substrate-Side Irradiation

The substrate-side irradiation experiments conducted using the extended-pulse-duration beam yielded results that show several striking differences from the experiments conducted using the short-pulse beam:

1. In the experiments performed using the BHF-treated silicon film, substrate-side-initiated melting was observed at much lower laser fluences and at much lower temperatures compared to the short-pulse-duration experiments.

2. In the experiments performed using the oxide-capped silicon film, both substrate-side-initiated melting and surface-side-initiated melting were observed.

Although surface-initiated melting was observed when the sample was irradiated after BHF surface treatment (just as in the experiments conducted using a short-pulse-duration beam), melting was also observed from the substrate-side. This is evident upon inspection of the TR signals presented in Figure B.2a. At energy densities above the complete melting threshold, by comparing the onset of saturation between the surface-side and substrate-side reflectances, one can easily deduce that melting initiated from both the surface and at or near the substrate. If melting were

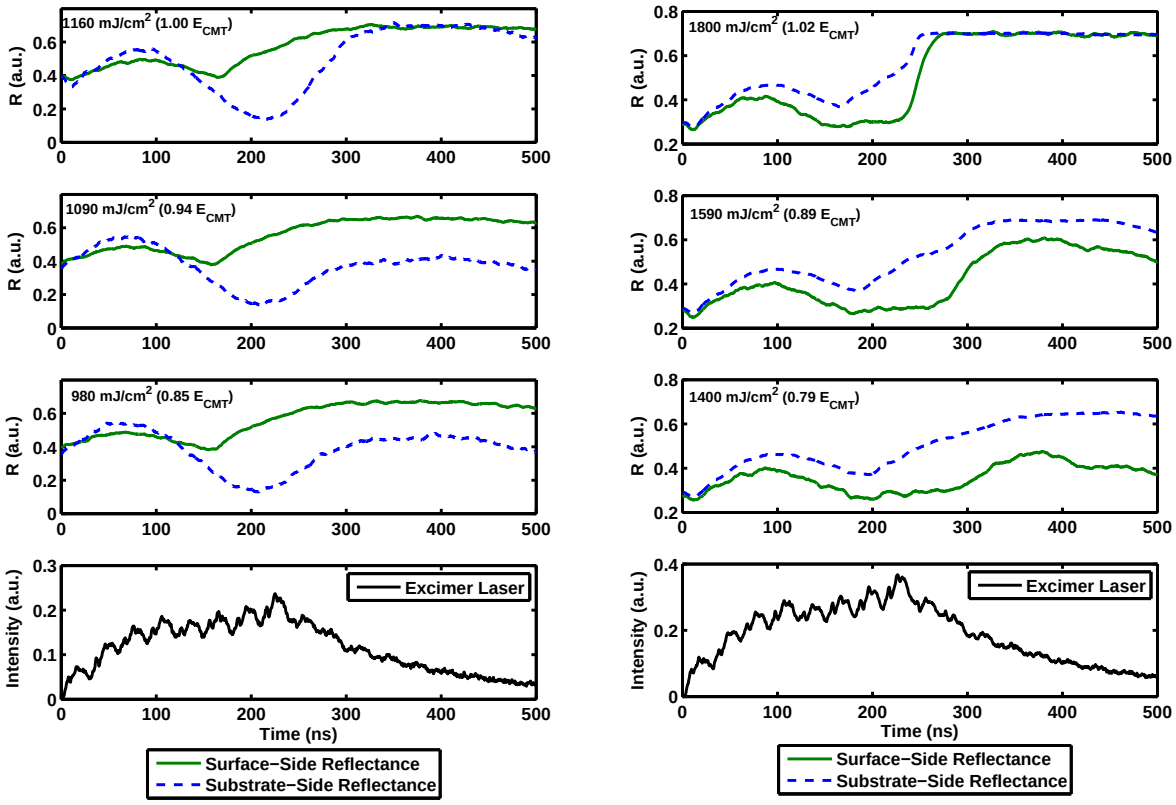

(a) BHF-treated surface

(b) Oxide-capped surface

Figure B.2: *In situ* surface-side and substrate-side TR signals measured during substrate-side excimer-laser irradiation of (a) the BHF-treated sample and (b) the oxide-capped sample at various energy densities (labeled in the figures). The time-dependent intensity profile of the incident excimer-laser pulse is presented in the bottommost subplots.

to initiate only from the surface, considering the transient temperature profile in the film (e.g., via `3DNS` calculations) and the interface response function, the time between the onsets of saturation between the surface-side and substrate-side TR signals would be much greater than what was observed. In other words, according to the interface response function for silicon, the solid-liquid interface cannot travel from the top surface to the bottom Si-SiO_2 interface in such a short period of time. Moreover, the lack of prominent oscillations in the substrate-side TR signals is consistent with the interpretation that melting initiated from both the surface-side and the substrate-side. The TR signals in Figure B.2a, when considering all of the above factors, must mean that melting initiated from both the surface-side and the substrate-side.

Similarly, melting initiated from both the surface-side and substrate-side in the oxide-capped films under substrate-side irradiation. The TR signals (shown in Figure B.2b) show that while melting first initiated from the substrate-side, melting also initiated from the surface-side.

Thermal analysis of both sets of experiments shows that melting was triggered at much lower temperatures at or near the Si-SiO_2 interfaces in the extended-pulse-duration experiments presented in this chapter in contrast to the short-pulse-duration experiments presented in Chapter 4. Whereas the superheating at and near the Si-SiO_2 interface in the short-pulse-duration experiments is estimated to be $370 \pm 35\ K$, the superheating in the extended-pulse-duration experiments is estimated to be $50 \pm 10\ K$.

B.3.2 Surface-Side Irradiation

For comparison and completeness, surface-side irradiation experiments were also performed. The results are consistent with short-pulse-duration experiments: Melting initiated from the surface-side, where it was hotter. Substrate-side-initiated melting was not observed.

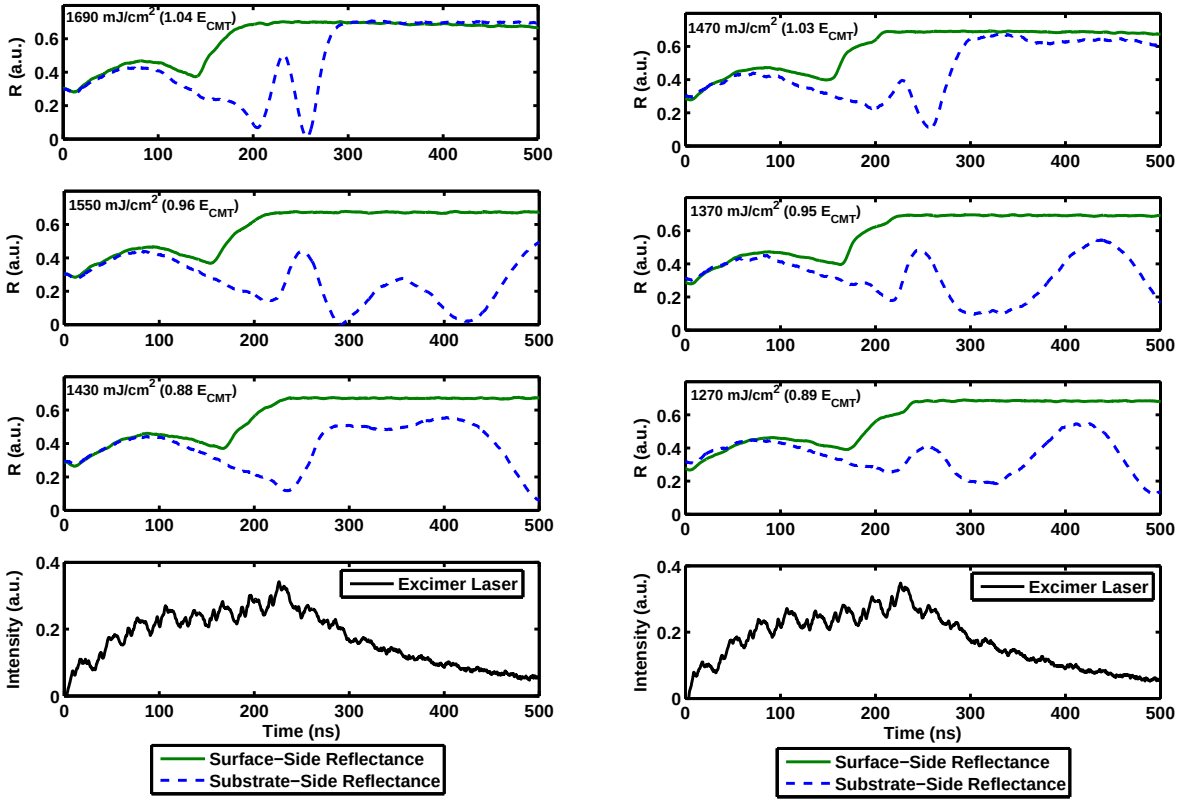

(a) BHF-treated surface

(b) Oxide-capped surface

Figure B.3: *In situ* surface-side and substrate-side TR signals measured during surface-side excimer-laser irradiation of (a) the BHF-treated sample and (b) the oxide-capped sample at various energy densities (labeled in the figures). The time-dependent intensity profile of the incident excimer-laser pulse is presented in the bottommost subplots.

B.4 Discussion

We suggest that the most striking result of this chapter is the much lower superheating observed under extended-pulse-duration irradiation. Here, we examine possible explanations for this much-reduced superheating observed for the extended-pulse-duration experiments.

Although the lower superheatings resulting from lower heating rates are predicted under the JMAK theory, our calculations show that the assumptions of heterogeneous nucleation of liquid silicon along an atomically flat Si-SiO_2 and lower heating rates alone cannot explain the much-reduced superheating. In order to examine the predicted superheating at these lower heating rates, time-temperature-transformation diagrams were constructed using the Avrami equation (Equation 6.5) along with classical nucleation theory (Equation 7.9), assuming heterogeneous nucleation (i.e., an Avrami exponent of 3) and contact angles of 60° and 85° along the Si-SiO_2 interface only, based on the classical-nucleation-theory-based calculations in Chapter 7. The experimentally observed superheating can be expected to lie between the 1% and 99% transformation curves. The TTT diagram, shown in Figure B.4, clearly demonstrates that the estimated observed superheating under extended-pulse-duration irradiation was much less than predicted based on these physical and theoretical assumptions.

A question one may ask is whether the much-reduced superheating can be attributed to a decrease in the strain energy resulting from softening of the SiO_2 due to being exposed to high temperatures at longer timescales. In order to examine this question, the TTT diagram shown in Figure B.5 was constructed using the nucleation rate equations that neglect the effects of the elastic strain energy. The calculations clearly show that even if strain energy is neglected, the observed superheating is still much less than what is theoretically predicted if only heterogeneous nucleation along an atomically smooth Si-SiO_2 interface is assumed.

In order for the results in this chapter to be consistent with our classical-nucleation-theory-based calculations for the short-pulse-duration experiments, melting could not have been triggered predominantly via heterogeneous nucleation of liquid silicon along the Si-SiO_2 interface. In the

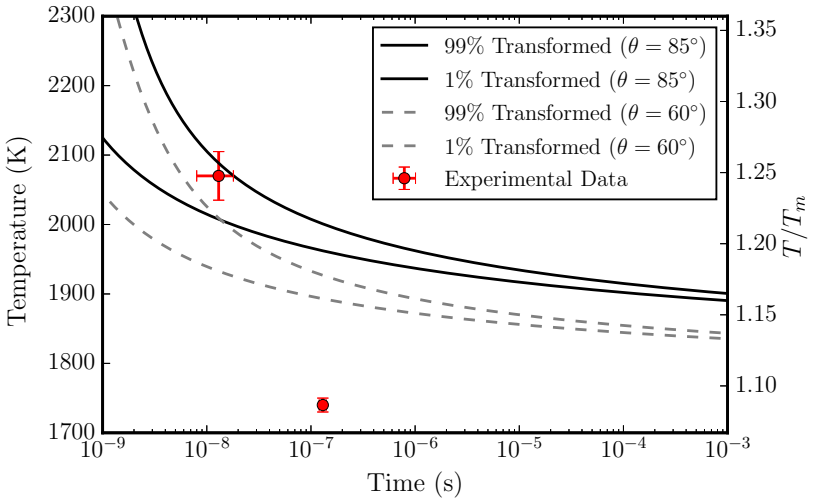

Figure B.4: Computed time-temperature-transformation (TTT) diagram for heterogeneous nucleation of liquid silicon in contact with SiO_2 with contact angles of 60° and 85° (based on the classical-nucleation-theory-based fit in Chapter 7).

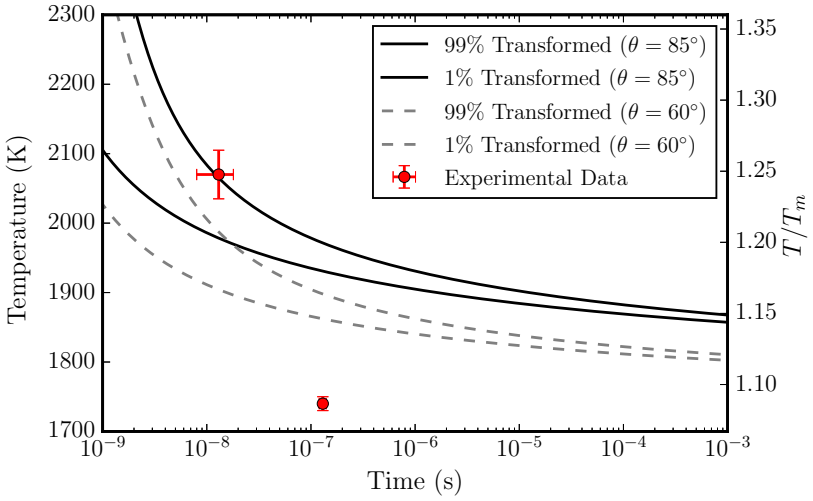

Figure B.5: Computed time-temperature-transformation (TTT) diagram for heterogeneous nucleation of liquid silicon in contact with SiO_2 with contact angles of 60° and 85° (based on the classical-nucleation-theory-based fit in Chapter 7). Here, we neglect strain energy.

short-pulse irradiation experiments, our classical-nucleation-theory-based analysis concluded that the kinetic superheating can be attributed predominantly to heterogeneous nucleation of liquid silicon along the Si-SiO_2 interface. The TTT diagrams in Figures B.4 and Figure B.5, the much-reduced superheating in the extended-pulse experiments suggest a very different situation. The longer timescales are expected to enable melting initiating at sparsely populated defects at lower temperatures due to a lower energy barrier (such as dislocations [97, 98]) to dominate, rather than liquid nucleation along the Si-SiO_2 interface, which, after considering the respective nucleation rates and the geometry of the sample, requires much higher temperatures. In order to test the above hypotheses, more experiments and calculations are needed.

B.5 Summary

In this chapter, we have investigated the effects of pulsed-laser irradiation under lower-heating-rate conditions (via extended-pulse-duration irradiation) on initiating melting at the Si-SiO_2 interface. It was found that the degree of superheating of the silicon along the Si-SiO_2 interface was significantly less than that of the short-pulse-duration experiments. We suggest that other melting mechanisms may be responsible for the much-reduced observed superheating.

Appendix C

Melting of Polycrystalline Silicon Films

Based on the results of our single-crystal experiments, we designed and implemented a simple set of experiments characterizing how polycrystalline silicon films melt. The results here suggest strongly that, in general, grain boundaries initiate melting much more readily than Si-SiO_2 interfaces. We discuss the technological ramifications of the present results and how they apply to laser processing of polycrystalline silicon films.

C.1 Background: Melting of Polycrystalline Silicon Films

Melting in polycrystalline silicon films is a critical part of several important laser crystallization processes. Some examples of these laser crystallization processes include excimer laser annealing (ELA) and mixed-phase-solidification (MPS). Since these processes inevitably involve partial melting of the polycrystalline film, the final microstructure is essentially dictated by the extent and details of melting in the film; solidification merely follows. Thus, in order to characterize these melt-mediated processes, it is necessary to understand the details of how melting transpires in these polycrystalline films.

Experimental investigations of melting in polycrystalline films, for a number of reasons, present formidable technical challenges. Presumably, the propensity for initiating melting at any interface is highly dependent on the involved interfacial energies. In ELA and MPS films, the microstructure is highly heterogeneous, containing a myriad of defects including low-angle grain boundaries, high-angle grain boundaries, grain boundary junctions, special grain boundaries, stacking faults, and more. Common to these microstructures are Si-SiO_2 interfaces, since these silicon films are deposited on glass or quartz substrates coated with an amorphous SiO_2 buffer layer. In the preceding chapters, we examined melting at the (100)-oriented Si-SiO_2 interface, demonstrating that it is very resistant to initiating melting in the solid silicon. Based on thermodynamic considerations and the results of other experimental investigations [1, 48, 50], we inferred that Si-SiO_2 interfaces of other crystallographic orientations can also be resistant to melting and can be superheated. In this chapter, based on our results on single-crystal silicon, we proceed to investigate melting in polycrystalline silicon.

C.2 Experimental Configuration

Based on the results in the previous chapters, we designed and implemented an experiment that examines the effects of a polycrystalline microstructure on melting. The experimental setup is identical to that of the single-crystal experiments and is described in Chapter 3. In order to directly compare our results on single-crystal silicon to the present experiment involving polycrystalline silicon, we start with the same starting material from the same wafer – 200-nm (100)-surface-oriented single-crystal silicon on a fused-quartz substrate. The initially single-crystal silicon was transformed into polycrystalline silicon via the complete-melting-crystallization (CMC) method [46] under substrate-side irradiation. CMC, when performed without substrate heating, produces highly defective and small grains (i.e., it contains a very high density of grain boundaries), since it involves the growth of heterogeneously and copiously nucleated grains [99, 100] in a highly undercooled melt [101]. Moreover, due to the small grain size (approximately tens of nanometers in diameter),

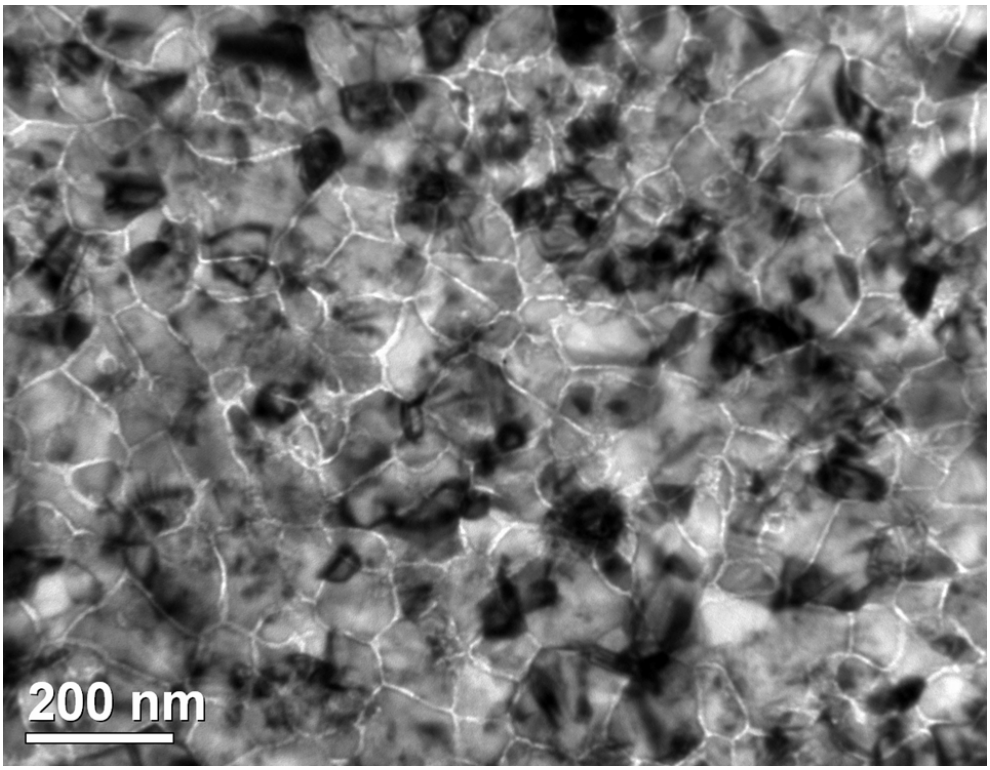

Figure C.1: Plan-view TEM image of a 200-nm CMC-processed silicon film on a quartz substrate. The film was defect-etched using the Secco etch formulation [3] in order to reveal the grain boundaries under TEM.

the density of grain boundary junctions is also substantial. A plan-view TEM image of this highly defective microstructure is shown in Figure C.1.

Substrate-side irradiation was performed again on the CMC-processed material. During each irradiation step, *in situ* surface-side and substrate-side TR signals were recorded, as described in detail in Chapter 3. BHF-etchant was used to remove any surface-oxide immediately before each irradiation step.

C.3 Results

The *in situ* TR signals obtained during substrate-side excimer-laser irradiation of the initially single-crystal silicon film is shown in Figure C.2. Upon inspection of the TR signals at $t > 300\,ns$, it is clear that solidification initiated from the substrate side. This is evident from the fact that, during solidification, the substrate-side TR signal decreased well before the surface-side TR signal, indicating that solidification must have initiated from the substrate side. Moreover, based on the work of Deng [100], in CMC, solidification initiates at the Si-SiO_2 interface via heterogeneous nucleation along the Si-SiO_2 interface. Melting of the single-crystal silicon on a quartz substrate, as can be seen from Figure C.3, initiated from the surface, even under substrate-side irradiation at this energy density, consistent with the results presented in Chapter 4.

The sample was irradiated again after CMC-processing. The *in situ* TR signals obtained during substrate-side excimer-laser irradiation of the now fine-grained polycrystalline silicon film at an incident energy density in the complete-melting regime is shown in Figure C.4. The *in situ* TR signals obtained during irradiation of the CMC-processed film in the partial melting regime is shown in Figure C.5. The TR signals obtained from the second pulse on the now polycrystalline film show significant differences than those obtained from the initial pulse on the single-crystal film. The most pronounced difference is that the onset of saturation of the substrate-side TR signal occurred well in advance of the onset of saturation of the surface-side TR signal for the experiment done at an incident energy density in the complete-melting regime. In the partial-melting regime, melting initiated only from the substrate-side. Considering the optics and phase transformation processes involved, this immediately indicates that melting initiated from the substrate-side. Furthermore, the difference between the onset of saturation of the substrate-side reflectance signal and that of the surface-side reflectance signal implies that the interface velocity must be lower in the second pulse on the CMC-processed film than in the original single-crystal film.

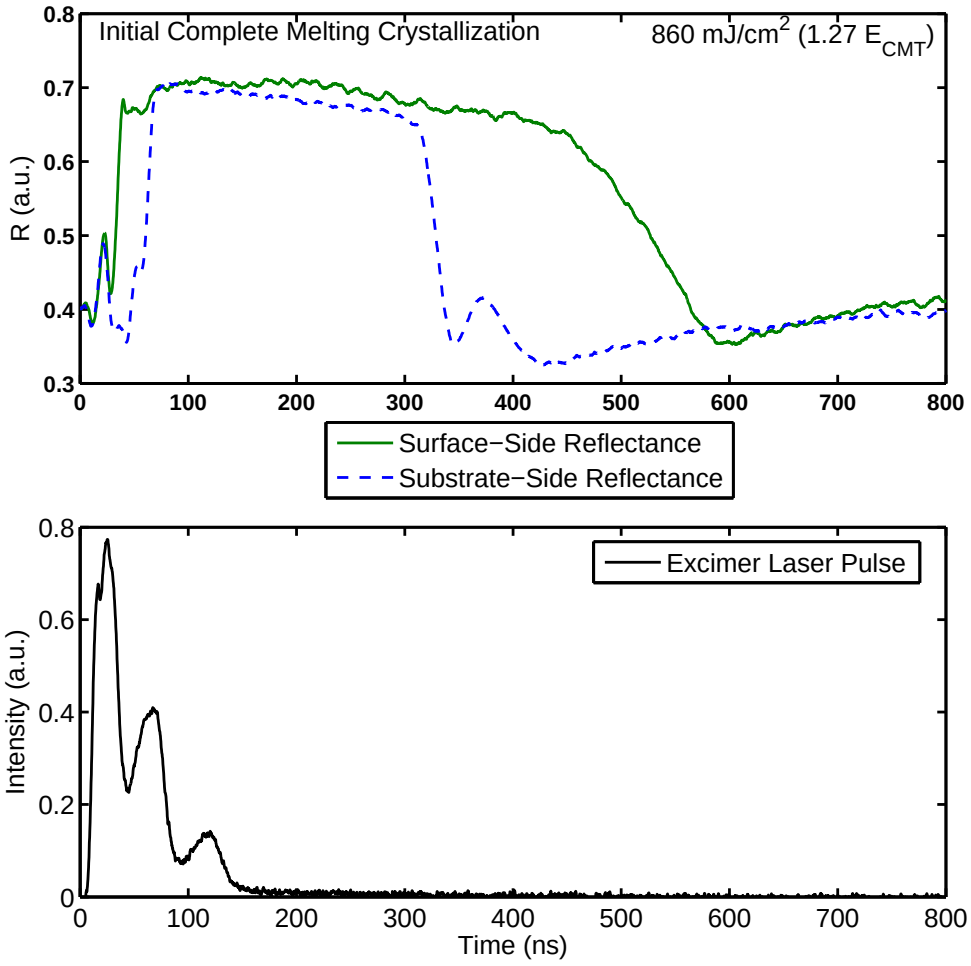

Figure C.2: Top: *In situ* TR signals obtained during the initial substrate-side irradiation step on the initially single-crystal silicon film. Here, we plot the entire time interval from the onset of melting to completion of solidification to illustrate that complete-melting-crystallization had occurred. Bottom: Time-dependent intensity profile of the incident excimer-laser beam.

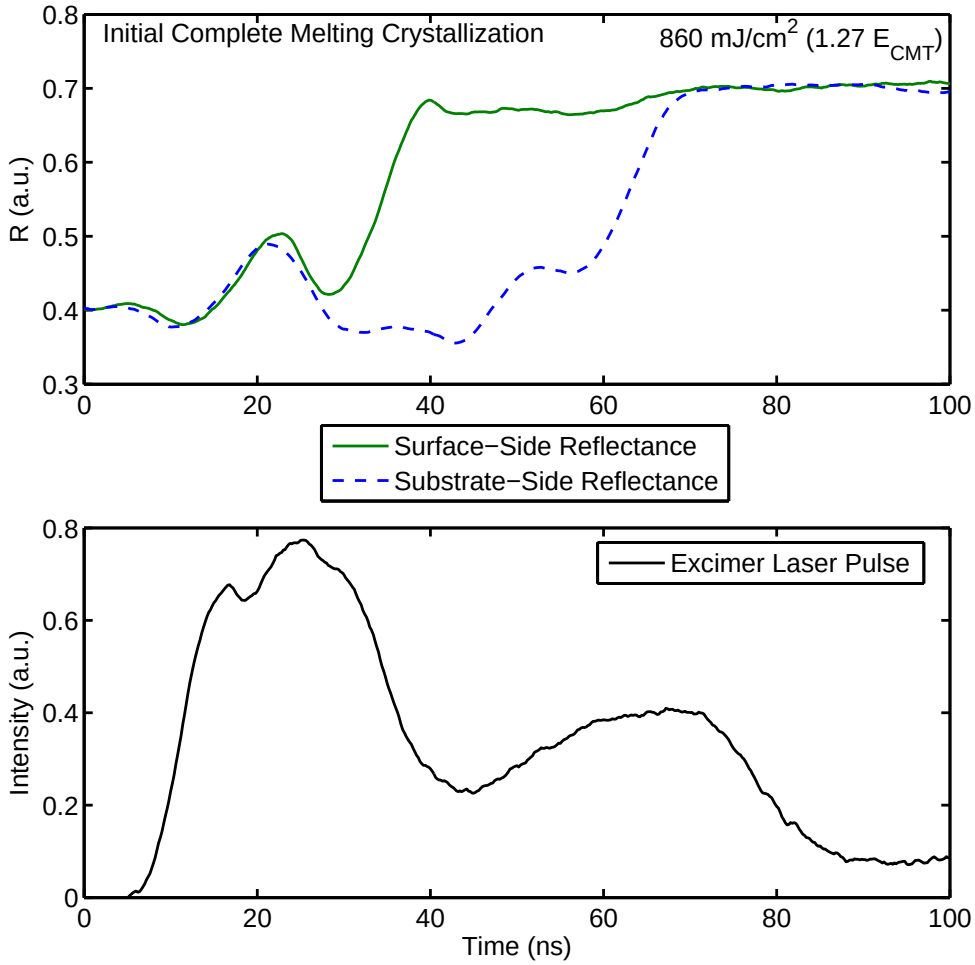

Figure C.3: Top: *In situ* TR signals obtained during the initial substrate-side irradiation step on the initially single-crystal silicon film. Bottom: Time-dependent intensity profile of the incident excimer-laser beam.

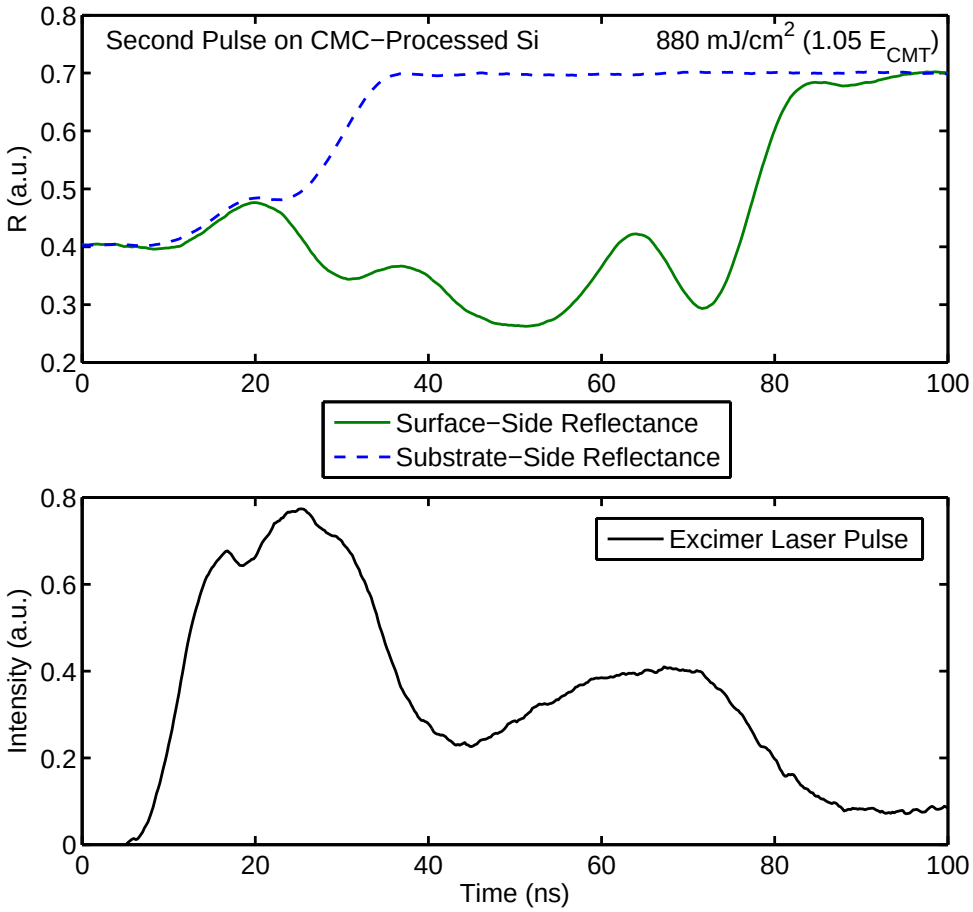

Figure C.4: Top: *In situ* TR signals obtained during the second substrate-side irradiation step on the now CMC-crystallized, fine-grained polycrystalline silicon film in the complete-melting regime. Bottom: Time-dependent intensity profile of the incident excimer-laser beam.

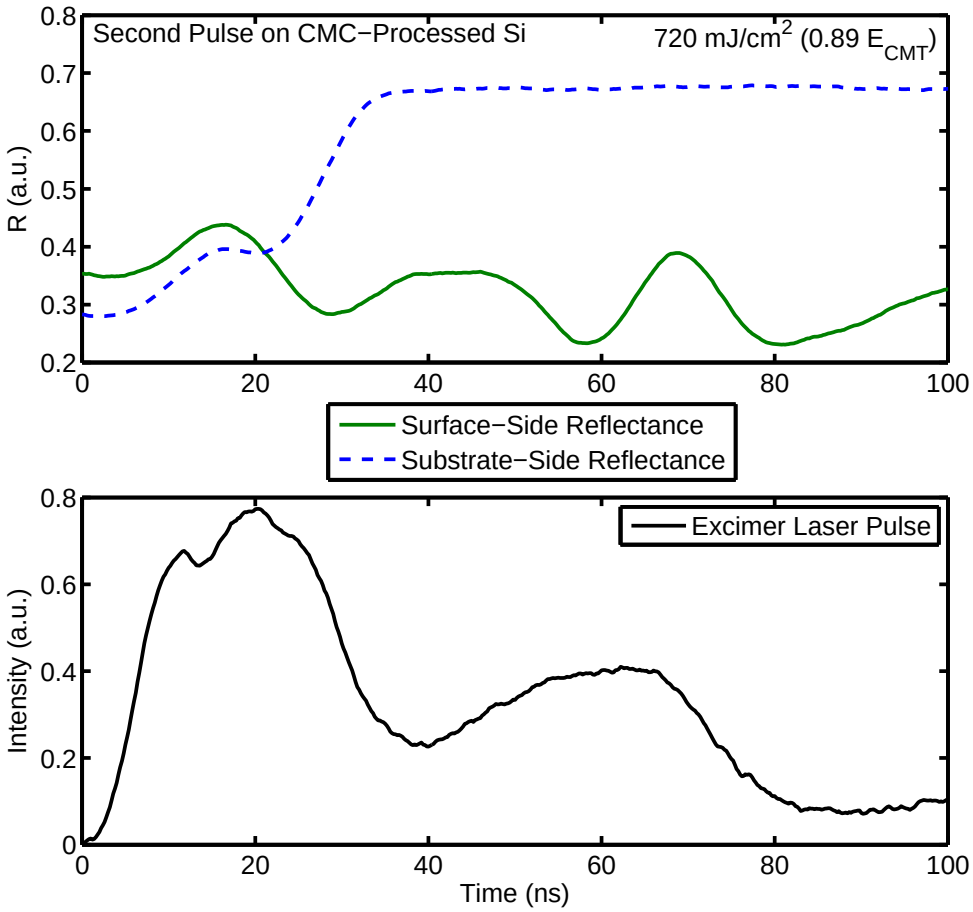

Figure C.5: Top: *In situ* TR signals obtained during the second substrate-side irradiation step on the now CMC-crystallized, fine-grained polycrystalline silicon film in the partial-melting regime. Bottom: Time-dependent intensity profile of the incident excimer-laser beam.

C.4 Discussion

C.4.1 Evidence of Grain-Boundary-Initiated Melting

Based on the results in this chapter, along with consideration of the results in the previous chapters, we argue from the results that, generally, grain boundaries (including grain boundary junctions, where three grain boundaries meet) are more prone to initiating melting than Si-SiO_2 interfaces. The main difference between the first irradiation step and the second irradiation step was the microstructure of the material being irradiated. During the first pulse on the initially single-crystal material, melting initiated from the surface, as expected based on our previous results. However, during the second pulse on the now fine-grained polycrystalline silicon (which is expected to contain a high density of random high-angle grain boundaries and grain boundary junctions), melting initiated from the substrate-side. Although polycrystalline silicon has slightly different thermal [102] and optical properties [103] than single-crystal silicon, these changes alone cannot account for the drastic difference in where melting initiated in the film. We argue that the details of the microstructure of the polycrystalline film must be considered along with the fact that Si-SiO_2 interfaces are not prone to initiating melting.

By considering the Si-SiO_2 interface free energies to the grain boundary energies, we argue that it is easier to initiate melting at Si-SiO_2 interfaces than at most grain boundaries. In the preceding chapters of this dissertation, we have shown that the (100)-oriented Si-SiO_2 interface is resistant to initiating melting. At the heating rates in the present experiments $\left(10^{10}\,K/s\right)$, the (100)-oriented Si-SiO_2 was observed to superheat in excess of $300\,K$ above the thermodynamic melting point. A consideration of theoretical considerations lead us to infer that other Si-SiO_2 interfaces can also undergo superheating under the same conditions. Atwater, et al. [50] estimated the energy anisotropy of the Si-SiO_2 interface between the (111)-oriented interface and the (100)-oriented interface to be $0.069\,J/m^2$ based on their experimental data. Chahal [1,48] and Wang [88] have experimentally demonstrated that the (100)-oriented Si-SiO_2 interface corresponds to the interface with the lowest free energy and the (111)-oriented interface corresponds to the highest

free energy. Based on these considerations, the value estimated by Atwater et al. [50] should correspond to the *maximum* anisotropy in the Si-SiO_2 interface free energy. A comparison of the anisotropy in the interface free energies show that these values are much less than the grain boundary energies [104] for random high-angle boundaries in silicon. The fact that we observed substrate-side-initiated melting during substrate-side irradiation of the polycrystalline films must mean that melting initiated primarily along grain boundaries and/or grain boundary junctions. Thus, based on all of the above considerations, random high-angle grain boundaries and grain boundary junctions are expected to initiate melting much more readily than Si-SiO_2 interfaces.

The results in this appendix are consistent with our hypothesis that random high-angle grain boundaries initiate melting much more readily than Si-SiO_2 interfaces. When considering that Si-SiO_2 interfaces can be significantly superheated above the equilibrium melting point at these heating rates, and that homogeneous melting occurs at much higher temperatures, melting must primarily initiate at grain boundaries, grain boundary junctions, and/or the top surface. Based on free energy considerations alone, it is further expected that the sites with the highest excess free energy – i.e., points where the grain boundary junctions and either the surface or Si-SiO_2 interface meet – would be most prone to initiating melting.

The experiments in this chapter, while unable to determine whether superheating had occurred along grain boundaries, also demonstrate that, if superheating had occurred, the degree of superheating that transpired in the film during excimer-laser irradiation of the CMC-processed film must be much less than that observed in the single-crystal experiments. The fact that only substrate-side-initiated melting was observed in the CMC-processed film at the same energy densities that was used to induce surface-initiated melting in the single-crystal film suggests that grain boundaries (including grain boundary junctions) generally cannot superheat as much as Si-SiO_2 interfaces, if at all. Even accounting for the slightly higher optical absorption and slightly lower thermal conductivity, the fact that substrate-side-initiated melting was observed at even *lower* incident-beam energy densities (see Figure C.5) further suggests that, generally, grain boundaries and grain boundary junctions in the material may initiate melting without a significant degree of superheat-

ing, if any. In order to determine whether superheating can transpire at grain boundaries and grain boundary junctions, more experiments are necessary.

It should be noted that while the grain boundaries that exist in the CMC-processed material in this set of experiments are predominantly random high-angle grain boundaries, low-angle boundaries and special boundaries such as twins also exist in the material [99, 100]. While random high-angle grain boundaries have been experimentally shown to melt at or at least very near the melting point [23], it is theoretically predicted that coherent boundaries can be superheated [28, 29]. For silicon in particular, molecular dynamics studies have shown that random high-angle grain boundaries may initiate melting at or very near the equilibrium melting point [24–26]. Even if the above experimental results and theoretical models are correct, then, when considering the the fact that the grain boundaries in the CMC-processed film are predominantly random high-angle boundaries, it is expected that very little, if any, superheating occurred in the film before the onset of grain-boundary- and grain-boundary-junction-initiated melting in the CMC-processed film. Our results here are consistent with prior experimental and theoretical investigations.

C.4.2 Implications for Existing Laser Crystallization Processes

Although melting in polycrystalline silicon films is important for industrially important laser crystallization processes, most of the work on pulsed-laser-induced melting of silicon films have thus far focused on melting in amorphous silicon [46, 105–108] and solidification in undercooled melts [14, 46, 100, 101, 105]. As discussed in Section 2.4, since laser crystallization processes such as excimer laser annealing (ELA) and mixed-phase solidification (MPS) involve partial melting of the polycrystalline film, and that solidification merely follows, melting is essentially the microstructure-determining step of the process. Based on previous research in our group, we maintain that grain enlargement in these partial-melting-based [46] laser crystallization processes results from local complete melting of the film at and near the grain boundaries [9]. The results in this chapter are clearly consistent with our stance on the profound significance of melting on the resulting microstructure of these laser crystallization processes. Therefore, research into how polycrystalline films melt can

lead to new fundamental understanding that can lead to better control of and improvements to these important laser crystallization processes.

The results presented here are consistent with the expectation that high-angle grain boundaries and grain boundary junctions are much more susceptible to initiating melting than Si-SiO_2 interfaces, which is consistent with the previously developed MPS model. Our results here agree with the previously developed model that describes melting during MPS processing [1, 48]. The assumption that melting initiates primarily along grain boundaries and grain boundary junctions and not at Si-SiO_2 interfaces is critical in the MPS model. The results in this thesis have experimentally demonstrated the validity of this assumption. Thus when developing models of melting in polycrystalline silicon (such as if one were to numerically model the ELA process), one must consider that while most grain boundaries and grain boundary junctions can readily initiate melting, Si-SiO_2 interfaces generally do not.

The results in this thesis have also demonstrated the significance of surface conditions and microstructure in melting. In laser planarization experiments performed on polycrystalline silicon films, it was found that BHF-etchant was required to produce a planarized surface [109]. Otherwise, if the surface had an oxide layer, melting would initiate along the grain boundaries and grain boundary junctions rather than at the top surface and planarization would not occur.

C.5 Summary

Pulsed-laser-melting of polycrystalline silicon is relevant to several important laser crystallization processes. Using the results of the previous chapters of this thesis, we have performed preliminary experiments in order to investigate melting in fine-grained polycrystalline silicon. Our results show that, under substrate-side irradiation, melting initiated and propagated from the substrate-side. Moreover, based on experimental and theoretical considerations, we infer that melting must have initiated along grain boundaries and grain boundary junctions. Our results are consistent with the previously developed model that described melting in MPS. Additionally, the observation that

grain boundaries can trigger melting much more readily than Si-SiO_2 interfaces is consistent with the results of laser planarization experiments. The results in this thesis demonstrate how defects such as grain boundaries, grain boundary junctions, surfaces, and Si-SiO_2 interfaces can affect melting during laser processing of silicon films.